WAVE NUMBER SELECTION AND DEFECT DYNAMICS IN PATTERNS WITH HEXAGONAL SYMMETRY

A Thesis
Presented to
The Academic Faculty

by

Denis B. Semwogerere

In Partial Fulfillment
of the Requirements for the Degree
Doctor of Philosophy

School of Physics
Georgia Institute of Technology
November 2003

WAVE NUMBER SELECTION AND DEFECT DYNAMICS IN PATTERNS WITH HEXAGONAL SYMMETRY

Approved by:

Dr. Michael F. Schatz, Committee Chair

Dr. Kurt Wiesenfeld

Dr. Roman O. Grigoriev

Dr. G. Paul Neitzel
(Mechanical Engineering)

Dr. Predrag Cvitanović

Date Approved: 11$^{\text{th}}$ November 2003

DEDICATION

Mzee Frederick Kiwanuka Semwogerere

ACKNOWLEDGEMENTS

As goes the cliché, "no man is an island". Many have contributed to the work that has led to this dissertation. It is thus my pleasure to have the opportunity to acknowledge their efforts.

First, I would like to thank my advisor Prof. Mike Schatz. His is a tough job. It is no simple task to formulate a clear problem that warrants research, and then to obtain funding for it, and successfully see it through. Thanks for the mentoring. The conferences, the paper writing, and the insistence that we give lab tours, are an integral part of being in this research group, and have contributed immensely to my personal development. But the long hours in the lab setting up and troubleshooting the experiment taught me perhaps the lesson I value the most: be resourceful.

I am grateful, of course, to the National Science Foundation and the Research Corporation, the sources of our funding, without which this work would not have been possible.

I would like also to thank other members of my committee. Prof. Roman Grigoriev and Prof. Predrag Cvitanović, who went through my thesis proposal in much finer detail than I could have asked for, given their schedules. Through their feedback emerged a much improved dissertation. Many thanks too to Profs. Paul Neitzel and Kurt Wiesenfeld for sacrificing their time and providing further suggestions.

There were numerous other people who made this research possible. Todd Meyrath guided me during my first few months in the lab, and was responsible for much of the early experimental setup. Luis Burgos drew up the original detailed designs of the second-generation-convection-cell and cooling assemblies. "Butch" Halverson, Norm Scott and Sam Mize are the talented folks over in the C.O.S. machine shop who built many of the critical components. Paul Neitzel gave us the use of his CO_2 laser which is a main component of our experimental setup. Prof. Hermann Riecke of Northwestern University was behind the idea to investigate secondary instability. He and Yuan-Nan Young, his postdoc at the time,

readily answered all questions and gave plenty of suggestions. In a move that demonstrates why we like him so much, Predrag Cvitanović invited Hermann Riecke to the department after I mentioned our long-distance discussions. Lab mates Jeff Rogers and Kapil Krishan, who had their own experiments to worry about, helped tremendously with suggestions and solutions to those nagging little things that hamper progress. And, I benefitted from many discussions with fellow graduate student Andreas Handel, our on-site example of German efficiency.

Thanks also to my other graduate student colleagues who made this experience at the Dept. of Physics a pleasant one: Murray Barrett, Barbara Breen, Frank Casanova, Api Shreenath, Marcelle Buford, and many others. Special thanks to Peace Rukundo and Nicola Barrett – non-Georgia-Tech special friends without whom these years would have been much less enjoyable. I am especially thankful for the support of my family, and the opportunities my dad, Dr. F. Kiwanuka Semwogerere, provided for all of us through years of selfless sacrifice. Dad, you have done your job well.

TABLE OF CONTENTS

DEDICATION . . . . . **iii**

ACKNOWLEDGEMENTS . . . . . **iv**

LIST OF FIGURES . . . . . **viii**

I INTRODUCTION **1**

II BACKGROUND **4**

2.1 Rayleigh-Bénard Convection 4

2.2 Bénard-Marangoni Convection 6

2.2.1 Stability Region 9

III EXPERIMENTAL SETUP **14**

3.1 Apparatus 14

3.1.1 Bénard-Marangoni Convection Cell 14

3.1.2 Flow Visualization 20

3.1.3 Flow Manipulation 23

3.2 Methodology 27

3.2.1 Stable Band 27

3.2.2 Secondary Instabilities 32

3.2.3 Penta-Hepta Defects 41

IV RESULTS AND CONCLUSIONS **52**

4.1 Stable Band 52

4.1.1 Remarks 53

4.2 Secondary Instability 54

4.2.1 Angular Dependence of Perturbations 56

4.2.2 Remarks 57

4.3 Penta-hepta Defects 58

4.3.1 Trajectory and Speed of PHD 58

4.3.2 Time Dependence of Speed 70

4.3.3 Discussion 76

V DISCUSSION **78**

APPENDIX A — PID CONTROL **81**

APPENDIX B — LINEAR REGRESSION ANALYSIS **83**

APPENDIX C — EVOLUTION OF HEXAGONAL PATTERNS FROM CONTROLLED INITIAL CONDITIONS IN A BÉNARD-MARANGONI CONVECTION EXPERIMENT **85**

APPENDIX D — PREPRINT: SUBMITTED TO PHYSICAL REVIEW LETTERS SEPTEMBER 2003 . . . . . **86**

REFERENCES **96**

LIST OF FIGURES

Figure 1 Illustration of fluid stream lines of straight convection rolls in RBC. (From Cross and Hohenberg [7].) 5

Figure 2 Stability diagram for rolls in RBC. The shaded region represents the parameter range in Rayleigh number R and wave number q space at fixed Prandtl number $Pr = 7$ for which straight rolls are stable. The region is bounded by secondary instabilities of the roll states: Z - zig-zag, CR - cross-roll, K - knot and SV - skewed-varicose. The dashed line labeled by N is the neutral stability curve above which convection occurs. (From Cross and Hohenberg [7].) 7

Figure 3 Liquid upflow in a pattern of BMC. (a) Shadowgraph image of a pattern of hexagons. Warm liquid flows upward in the dark cell centers and flows downward at the white cell edges. (b) Schematic of the liquid flows. . . 9

Figure 4 Neutral stability curves for two different types of instability in BM convection. M is the Marangoni number and q is the wave number of the instability. (a) As M is raised from zero the onset of convection is to patterns of $q \approx 2$ indicated by the global minimum of the neutral stability curve. (b) For sufficiently thin liquid depths d the global minimum is at $q = 0$ and a long wavelength deformation of the liquid is the primary instability. (From Schatz and Neitzel[28].) 10

Figure 5 Theoretical prediction of the stability band for hexagons in BMC [26] for $Pr \to \infty$ and $\Gamma \approx 2.7$ in ϵ-k space. $\epsilon = (M - M_c)/M_c$ and k is the wave number. Hexagons are stable in the shaded region bounded by phase instabilities. The dots are experimental data obtained from [30]. The line near the bottom is the neutral stability curve; the line at left corresponds to amplitude instabilities. (From Bestehorn [26]) 12

Figure 6 Schematic of the general setup of the experiment. The infrared laser and mirror assembly enable rapid local heating of the gas liquid interface. The light source along with a camera and other optics are used for shadowgraph visualization of the convective liquid flows. 15

Figure 7 General setup of the cell assembly. A heating pad below the aluminum mirror sets the bottom temperature while circulating cooled carbon disulfide maintains the top temperature. The bottom set of fine adjustment screws levels the liquid and the top set controls the thickness of the air gap. 16

Figure 8 Closeup of the bottom plate. The thermistor is placed in the center of the aluminum plate with some heat-sink compound to ensure accurate temperature readings. The Teflon tubing attached to the syringe allows controlled filling of the cell with silicone oil. 17

Figure 9 Schematic of the cooling system. CS_2 is pumped through a heat exchanger placed in temperature bath. The reservoir is set up to remove air bubbles from the system. 19

Figure 10 Schematic of shadowgraph setup. 21

Figure 11 (a) A typical 320×240 shadowgraph image captured from CCD camera. A background image taken with no pattern present has been subtracted to enhance the image. (b) The same image cropped to 240×240 and masked with a circular window that has a smooth transition to zero. 22

Figure 12 A shadowgraph image of straight convection rolls in RBC (a), and a side view illustration of the paths taken by light rays emerging from the convection cell. Caustics arise in regions near the focal point of the pattern where light rays intersect, and appear in a shadowgraph image as regions of increased intensity. 23

Figure 13 The process of imposing an ideal hexagonal pattern on the BMC cell. (a) Computer generated grid of points that correspond to the centers of individual hexagonal cells in the pattern. (b) The boundary points that are imposed to separate the interior dynamics from perturbations due to the cell apparatus wall. They are the same points as in (a) minus the interior 75%. (c) The infrared laser rapidly scans across the free surface layer from right to left. The dark vertical line indicates the current position of the laser. (d) A perfect pattern formed after several passes by the laser beam. The dashed line indicates the boundary of the lased points in (b). 24

Figure 14 The main features of the laser scanning system. By controlling the laser and a pair of mirrors the scanner can direct a laser beam to selected coordinates on the target. 26

Figure 15 A hexagonal pattern (a) and the power spectrum of its Fourier transform (b). 28

Figure 16 Decomposition of an imposed ideal hexagonal pattern into three plane waves oriented 120° with respect to one another. Each plane wave is perpendicular to two sides of the imposed boundary shown in (a) by the dashed lines. By moving opposite walls of the boundary the wave number of each plane wave can be varied by $\approx 5\%$ independently of the other two plane waves that make up the pattern. 29

Figure 17 (a) Ideal hexagonal pattern formed by superposing three plane waves oriented 120° with respect to each other. (b) Hexagonal array of points corresponding to the centroids of the peaks of the pattern. 30

Figure 18 Hexagonal array of points (a) before and (b) after uniformly stretching by a factor of 0.9 in a fixed direction to adjust the wave number of the component rolls relative to one another. 31

Figure 19 Hexagonal patterns that have become unstable as a result of being imposed with wave number outside the stable band. (a) Imposed q too high. b) Imposed q too low. 31

Figure 20 Time evolution of average wave number q of ideal hexagonal patterns illustrates stable vs unstable wave numbers for $\epsilon = 0.28$. Time is in units of τ_v. q represents the average of q_1, q_2, q_3; the variance of q is typically much smaller than the symbol size. Average wave numbers q that are time-independent correspond to stable ideal hexagonal planforms ($\bullet$). By contrast, time-dependent q correspond to patterns of initially ideal hexagons ($t = 0$) that lose stability ($\times$). The shaded area shows the extent of the stability region for ideal hexagons predicted by theory in [26] for the same ϵ. 33

Figure 21 Secondary instability of straight roll patterns observed in RBC. (a) Cross roll instability – rolls with q that is too large decrease in amplitude and are replaced with rolls of smaller q oriented at 90° with respect to the original ones. (b) Zig-zag instability – Rolls with q too small form "zig-zags" which reduce the spacing between the rolls, effectively raising q. As the zig-zags increase in amplitude neighboring rolls join and form new rolls. (From Busse *et al.* [8].) 34

Figure 22 Evolution of a hexagonal pattern with q too small. The data is for $\epsilon = 2.01$ which corresponds to a measured low q boundary of $\epsilon = 2.04$. The images are taken $\sim 5\tau_v$ apart. 35

Figure 23 A shadowgraph image (a) of hexagons with a longitudinal phase perturbation is shown with the pattern's three roll components (b-d) extracted by complex demodulation. For the purposes of illustration, the perturbation, imposed as an initial condition, is shown with an amplitude that is larger than typical modulations by a factor of 8. In (a), the white edges and dark centers of the hexagons indicate, respectively, regions of down-flow and up-flow. (b) The main modulation is to the $\mathbf{q_1}$ rolls – note their compression and dilation. Shading has been added to emphasize the long-wave nature of the modulation – the overall lighter areas have higher wave number than the darker regions. (c) $\mathbf{q_2}$ rolls are sheared slightly by the modulation.(d) The $\mathbf{q_3}$ rolls are modulated with the same amplitude and phase as the $\mathbf{q_2}$ rolls. 37

Figure 24 Spatial and temporal evolution of the longitudinal phase perturbation. (a) The profile of the local wave number of the $\mathbf{q}_1$ rolls (scaled by the mean value $q = 2.08$) is plotted at times $t = 0$ (symbol $-$), $t = 13$ ($--$) and $t = 27$ ($\cdot-$); thus the phase modulation adjusts the overall wave number by a maximum of less than 1.5%. The long-wave nature of the perturbation is apparent – the modulation wave number $k = 0.14$ is approximately $1/15^{\text{th}}$ of the mean q. (b) The amplitude ($k\alpha$) is plotted as a function of time on a semi-log scale; the slope of this curve yields the growth rate, which is negative for perturbations within the stable band. 38

Figure 25 A shadowgraph image (a) of hexagons with a transverse phase perturbation is shown with the pattern's three roll components (b-d) extracted by complex demodulation. For the purposes of illustration, the perturbation is shown with an amplitude that is larger than typical modulations by a factor of 9. (b) The $\mathbf{q}_1$ component is unaffected by the transverse modulation. (c) The roll component labeled by wave vector $\mathbf{q}_2$ that shows the shearing of the rolls in a direction transverse to the $\mathbf{q}_1$ rolls. (d) The $\mathbf{q}_3$ component is modulated with the same amplitude but opposite phase as the $\mathbf{q}_2$ component. 39

Figure 26 Climb motion of a single dislocation in a roll pattern in RBC. The wave number above the defect q_u is "preferred" over that below the defect q_l hence motion downward. (Adapted from Cross and Hohenberg [7].) . . . 42

Figure 27 Decomposition of an imposed hexagonal pattern with a PHD embedded near its center. (a) The five-sided cell of the PHD has dark shading and the seven-sided cell has light shading. The $\mathbf{q_1}$ (a) and $\mathbf{q_3}$ (c) rolls have dislocations while the $\mathbf{q_2}$ rolls(d) are dislocation-free. The dislocations have opposite winding phase numbers. In this case any counter-clockwise close path encircling the defect has a jump of -2π for $\mathbf{q_1}$ and $+2\pi$ for $\mathbf{q_3}$. 43

Figure 28 Illustration of grid of points obtained from a hexagonal pattern containing a single PHD is obtained. (a) Numerically obtained gray scale image with a PHD in the center. (b) Grid of points to be used for imposing the pattern onto the BM convection cell obtained by the finding the centroids of the peaks in (a). The dashed lines indicate rows of extra cells or points. The boxes are centered around the defect core. 47

Figure 29 Local wave number of the $\mathbf{q}_3$ roll pattern along a line through a single penta-hepta defect. (a) Shadowgraph image of PHD taken with $\epsilon = 3.8$. The dark colored patch is the five sided cell and the light patch is the seven sided cell. (b) The corresponding $\mathbf{q}_3$ roll pattern. (c) Cross-section of the local wave number of the mode along the dashed line indicated in (a) and (b). The wave number from the core to "A" is lower than the wave number from the core to "B" because it has one less row. In the ideal case the lower (high) wave number increases (decreases) asymptotically to a value which defines the wave number of the rolls. The wave number is well approximated by taking the average of the two over a range of several wavelengths away from the defect core. In this case the average wave number is $q_3 = 2.39$. 48

Figure 30 Illustration of the phases (b), (d), (f) of the slowly varying amplitudes of the components roll patterns (a), (c), (e) of a single PHD. 50

Figure 31 The band of stable wave numbers q for ideal hexagonal patterns ($q_1 = q_2 = q_3 = q$) is shown for a range of reduced temperatures ϵ. The experimentally determined stable wave numbers lie between the low- and high-q boundaries (•) and are compared with the theoretical predictions (solid lines) of Bestehorn [26]. 53

Figure 32 The Busse balloon – a three-dimensional region of stable straight convection rolls in R-P-α (Rayleigh number-Prandtl number-wave number) space. (From Busse [22].) 55

Figure 33 Plot of growth rate vs. wave number for the transverse perturbation. The dashed lines represent experimentally measured boundaries of the stable band measured previously for $\epsilon = 0.46$. The data are shown for $\theta = 0$ ($\times$,$\circ$), $\theta = \pi/18$ ($\square$), $\theta = \pi/12$ ($\Diamond$), $\theta = \pi/6$ ($\triangleright$), $\theta = \pi/3$ ($\triangle$), and $\theta = 2\pi/3$ ($\triangledown$). 56

Figure 34 Plot of growth rate vs. wave number for the longitudinal perturbation. The dashed lines represent experimentally measured boundaries of the stable band for $\epsilon = 0.46$. The growth rate of the longitudinal perturbation appears to sharply decrease and trend to zero at the high-wave-number boundary. The data are shown for $\theta = 0$ ($\times$,$\circ$), $\theta = \pi/18$ ($\square$), $\theta = \pi/12$ ($\Diamond$), $\theta = \pi/6$ ($\triangleright$), $\theta = \pi/3$ ($\triangle$), and $\theta = 2\pi/3$ ($\triangledown$). 57

Figure 35 Pairs of PHDs forming spontaneously from an initially ideal hexagonal pattern with q too small. The dark cells are five-sided and the light cells are seven-sided. The defects propagate outward and increase q in the process. 59

Figure 36 The trajectory of an isolated PHD for (a) equal and (b) unequal wave numbers at $\epsilon = 0.28$. Each circle represents the position of the PHD in intervals $\sim\tau_v$. The dashed arrows indicate direction of PHD motion. The trajectories are plotted on the defect-free mode $\mathbf{q}_2$. (a) For $Q_1 = Q_2 = Q_3 = 0.16$ the path is roughly parallel to $\mathbf{q}_2$. (b) Trajectory after Q_3 is decreased by 0.6. 60

Figure 37 Theoretical and numerical predictions of (a) speed and (b) angle of the PHD motion as a function of the wave number correction Q_3 of the component rolls with dislocation of negative phase-winding number. For the other component roll patterns corrections are $Q_1 = Q_2 = 0$. The angles are measured with respect to the wave vector of the dislocation-free roll pattern. The solid lines are theoretical predictions, and the open and closed circles are from numerical simulations. (Adapted from Tsimring [15].) . 62

Figure 38 Measured (a) speed and (b) angle of PHD motion as a function of the wave number correction Q_1 for $\epsilon = 0.46$. $Q_2 = Q_3 = 0$. The angles are measured with respect to the $\mathbf{q}_2$ wave vector. The gaps in the data plots correspond to values of Q_1 for which the PHD-path length was too short to estimate an accurate direction of motion. 63

Figure 39 Path of PHD when Q_1 is adjusted and $Q_2 = Q_3 = 0$. Motion is such that the PHD does not climb along the $\mathbf{q}_3$ rolls. The dashed arrow is the direction when $Q_1 > 0$ and the dotted arrow is the direction when $Q_1 < 0$. 64

Figure 40 Theoretical and numerical predictions of (a) speed and (b) angle of PHD motion as a function of the wave number correction Q_1 of the component rolls with dislocation of positive phase-winding number. The other component roll pattern with a dislocation has $Q_3 = 0.1$, while the dislocation-free roll pattern has $Q_2 = 0$. The angles are measured with respect to the wave vector of the dislocation-free roll pattern. The solid lines are theoretical predictions, and the open and closed circles are obtained by numerical simulations. (Adapted from Tsimring [15].) 65

Figure 41 Measured (a) speed and (b) angle of PHD as a function of the wave number correction Q_1 for $\epsilon = 0.46$ for $Q_2 = 0$ and $Q_3 = 0.14$. The angles are measured with respect to the $\mathbf{q}_2$ wave vector. The gaps in the data plots correspond to values of Q_1 for which the PHD-path length was too short to estimate an accurate direction of motion. 66

Figure 42 The shaded region marks the range of angles that the PHD moves along when Q_1 is adjusted, for fixed $Q_2 = 0$ and $Q_3 = 0.14$. 66

Figure 43 wave-number selection through formation of a PHD: $t = 0$. (a) A single PHD with (a) $q_1 = 2.37$, (c) $q_3 = 2.5$ and (d) $q_2 = 2.68$. q_2 is beyond the high-wave-number boundary ($q = 2.52$) of the stable band. 67

Figure 44 wave-number selection through formation of a PHD: Evolution of $\mathbf{q}_2$ roll pattern. (a) At $t = 0$ the roll pattern is defect-free. A pinching off of the rolls starts to occur at the core of the PHD at (b) $t \sim 16\tau_v$ which (c) grows steadily and (d) by $t \sim 24\tau_v$ a roll has split and formed to two dislocations of opposite phase-winding number. 68

Figure 45 Wave-number selection through formation of a PHD: $t \sim 50\tau_v$; a new pair of PHDs formed out of the old PHD and the two new dislocations, shown in (d), formed from a roll of the $\mathbf{q}_2$ pattern. The PHDs are moving in a direction (white arrows) that eliminates a roll from the $\mathbf{q}_2$ pattern. The original PHD was a combination of dislocations I and II, shown in (b) and (c) respectively. The top PHD is a combination of dislocations I and III, and the bottom PHD is a combination of dislocations II and IV. The dashed and dot-dashed lines in (a) are the extra rows of cells that correspond to rolls with dislocations. 69

Figure 46 PHD motion via cell collapse. (a) PHD at the center of the pattern. The dashed line marks an extra row of cells of the $\mathbf{q}_1$ component rolls. The dot-dashed line marks an extra row of cells associated with the $\mathbf{q}_3$ rolls. The extra rolls terminate at the PHD core. (b)-(d) The pentagonal cell in the process of collapsing. (e) The pentagon has collapsed into a vertex and an edge and in the process converted the heptagon into a hexagon, and changed a hexagon into a pentagon. (f) A partial T1 process creates an edge which converts a hexagon into a heptagon. Thus the penta-hepta pair has been recreated at new location. The process has reduced the length of the extra roll of $\mathbf{q}_1$, thereby moving the PHD core upward by one cell length. 71

Figure 47 Two elementary processes by which hexagonal patterns rearrange themselves. (a) T1 process – edge between cells 2 and 4 shrinks to zero and is replaced by another resulting in cells 1 and 3 becoming neighbors and 2 and 4 separating. (b) T2 process – a three-sided cell vanishes. (Adapted from Weaire [39].) 72

Figure 48 PHD motion via cell mitosis. (a) PHD at the center of the pattern. The dashed line marks an extra row of cells of the $\mathbf{q}_1$ component rolls. The dot-dashed line marks an extra row of cells associated with the $\mathbf{q}_3$ rolls. The extra rolls terminate at the PHD core. (b) The boundary separating the heptagonal and pentagonal cells deforms slightly. (c)-(e) The heptagonal cell splits into two pentagons through mitosis as the downward flowing liquid through its center becomes stronger. (f) After the split a partial T1 process creates an edge which converts one of the pentagons into a hexagon, while at the same time changing a hexagon into a heptagon. Thus the pentagon-heptagon pair has been recreated. The row corresponding to the dislocation in the $\mathbf{q}_1$ rolls has shifted to the left and lengthened slightly in the rearrangement process while the row with a dislocation in $\mathbf{q}_3$ has increased in length by one cell. Thus the core of the PHD has moved by one cell length. 73

Figure 49 Measured time series of PHD speeds for $q_1 = q_2 = q_3$ at $\epsilon = 0.28$, corresponding to (a) pentagonal cell collapse with $q = 2.23$ and (b) heptagon mitosis with $q = 1.95$. The solid line indicates the magnitude of velocity perpendicular to $\mathbf{q}_2$ while the dashed line shows the magnitude of velocity perpendicular to $\mathbf{q}_3$. Pentagonal cell collapse is characterized by jumps in PHD motion that occur alternately between directions perpendicular to $\mathbf{q}_2$ and perpendicular to $\mathbf{q}_3$; this alternating character is shown in (a). By contrast, PHD motion during heptagon mitosis is smoother, as shown in (b). 74

Figure 50 PHD motion via "neighbor switching". The dashed line marks an extra row of cells of the $\mathbf{q}_1$ component rolls. The dot-dashed line marks an extra row of cells associated with the $\mathbf{q}_3$ rolls.The edge indicated by the box (a) shrinks to a point (b) and is replaced by another edge along a different axis (c). In the process of rearrangement the PHD moves by π/q. 75

Figure 51 Ziegler-Nichols reaction curve. 82

Figure 52 A shadowgraph image (a) of hexagons with a longitudinal phase perturbation is shown with the pattern's three roll components (b-d) extracted by complex demodulation. For the purposes of illustration, the perturbation, imposed as an initial condition, is shown with an amplitude that is larger than typical modulations by a factor of 8. In (a), the white edges and dark centers of the hexagons indicate, respectively, regions of downflow and upflow. (b) The main modulation is to the $\mathbf{q_1}$ rolls – note their compression and dilation. Shading has been added to emphasize the long wave nature of the modulation – the overall lighter areas have higher wave number than the darker regions. (c) $\mathbf{q_2}$ rolls are sheared slightly by the modulation.(d) The $\mathbf{q_3}$ rolls are modulated with the same amplitude and phase as the $\mathbf{q_2}$ rolls. 88

Figure 53 A shadowgraph image (a) of hexagons with a transverse phase perturbation is shown with the pattern's three roll components (b-d) extracted by complex demodulation. For the purposes of illustration, the perturbation is shown with an amplitude that is larger than typical modulations by a factor of 9. (b) The $\mathbf{q_1}$ component is unaffected by the transverse modulation. (c) The roll component labeled by wave vector $\mathbf{q_2}$ that shows the shearing of the rolls in a direction transverse to the $\mathbf{q_1}$ rolls. (d) The $\mathbf{q_3}$ component is modulated with the same amplitude but opposite phase as the $\mathbf{q_2}$ component. 91

Figure 54 Spatial and temporal evolution of the longitudinal phase perturbation. (a) The profile of the local wave number of the $\mathbf{q_1}$ rolls (scaled by the mean value $q = 2.08$) is plotted at times $t = 0$ (symbol $-$), $t = 13$ ($--$) and $t = 27$ ($\cdot-$); thus the phase modulation adjusts the overall wave number by a maximum of less than 1.5%. The long wave nature of the perturbation is apparent – the modulation wave number $k = 0.14$ is approximately $1/15^{\text{th}}$ of the mean q. (b) The amplitude ($k\alpha$) is plotted as a function of time on a semi-log scale; the slope of this curve yields the growth rate, which is negative for perturbations within the stable band. 92

Figure 55 Plots of growth rate vs. wave number for the transverse perturbation (a) and the longitudinal perturbation (b). The dashed lines represent experimentally measured boundaries of the stable band measured previously for $\epsilon = 0.46$. (a) The growth rate for the transverse perturbation appears to go to zero at the low wave number boundary. (b) The growth rate of the longitudinal perturbation appears to sharply decrease and trend to zero at the high wave number boundary. The data are shown for $\theta = 0$ ($\times$,$\circ$), $\theta = \pi/18$ ($\square$), $\theta = \pi/12$ ($\Diamond$), $\theta = \pi/6$ ($\triangleright$), $\theta = \pi/3$ ($\triangle$), and $\theta = 2\pi/3$ ($\triangledown$). 93

CHAPTER I

INTRODUCTION

Many systems are observed to exhibit similar macroscopic spatial structure even when they differ in their microscopic detail; for example, cellular structures appear as nanometer sized pores in electrochemical anodization of aluminum [1], concentrations of chemicals in reaction diffusion systems [2], and standing wave patterns in vertically vibrated granular materials [3]. The structures can be as simple as patterns of straight rolls [4] and as complex as superlattices and quasipatterns [5, 6]. In all the cases described above, the structure has arisen as a result of the system being subject to nonequilibrium external conditions which can be quantified by a control parameter R. When R is adjusted it can lead to an instability that drives the system from a uniform featureless state to a state with a pattern; or to one that changes the nature of an existing pattern.

Patterns formed under nonequilibrium conditions arise out of instabilities that can be divided into several broad categories: instabilities that are periodic in space and stationary in time; instabilities that are uniform in space and oscillatory in time; and instabilities that are periodic in space and oscillatory in time. In this dissertation we restrict ourselves to patterns that fall under the first category. Above onset they are stationary with a wave number q, selected by the initial conditions from a continuous band of allowed wave numbers, that is bounded by secondary instabilities. The canonical example is that of periodic rolls observed in Rayleigh-Bénard convection (RBC). In RBC a thin confined fluid layer is subjected to a vertical temperature gradient ΔT by uniformly heating the plate that forms its bottom boundary while cooling the plate that bounds it from above. The control parameter is the Rayleigh number R, which is a nondimensional measure of ΔT. For low R buoyancy forces that arise from the heating are balanced by the viscous forces of the fluid, thus heat travels from the bottom plate to the top by conduction alone. At a critical value of R the destabilizing effect of buoyancy is strong enough to overcome the

stabilizing effect of the dissipation of viscosity and the horizontal thermal conductance in the fluid layer, and convection results. Mass conservation constrains warm rising fluid to be balanced by descending cooler fluid. The fluid motion forms a pattern of rolls, with some wave number q, as expected from the translational symmetry of the convection cell – it is assumed that the lateral extent of the convection cell is much larger than the fluid thickness. Pioneering theoretical and experimental work on RBC was performed by Busse *et al.* [8] and led to the famous "Busse balloon" – a fundamental result as it demonstrates the existence of a finite stability region (in this case for straight rolls) and identifies the secondary instabilities that limit it. Those instabilities are striking in appearance and have names such as "zig-zag" and "cross-roll" that describe their form. They have a universal character and have been associated with roll state instability in other physical systems such as nematic liquid crystals [9], granular materials [10], and nonlinear optics [11].

Theoretical and numerical studies have been carried out on more complex stationary periodic patterns such as those of triangles [12] and of hexagons [13, 14], but quantitative experimental investigations are lacking. The goal of this dissertation is to present results of the first quantitative experimental investigations of hexagons. The experiments are performed on a Bénard-Marangoni convection (BMC) cell – an experiment similar to RBC but with a convecting fluid that has a free upper surface. That boundary condition breaks the inversion symmetry observed in the vertical direction in RBC, and leads to the formation of stable hexagons at onset. The experiments concentrate on three areas of fundamental interest: First the region of stability of hexagons is determined for a range of control parameter by imposing ideal hexagonal patterns as initial conditions and observing their stability for different wave numbers – patterns imposed with wave number inside the stable band are stationary, while those imposed with wave number outside the stable band form penta-hepta defects (PHD) as a result of secondary instability. Next, the nature of the mechanisms that lead to secondary instability are studied. Theory suggests that perturbations that are long wavelength modulations of the phase of the hexagonal pattern are responsible for secondary instability [13, 14]. The phase perturbations are of two different types: A longitudinal modulation of wave vector $\mathbf{k}$ that has a curl-free phase vector $\mathbf{\Phi}$ *parallel* to $\mathbf{k}$ analogous to a

P-wave in elastic media; and a transverse modulation with a divergence-free phase vector $\mathbf{\Phi}$ *perpendicular* to $\mathbf{k}$ and analogous to an S-wave. Finally, the motion of PHDs is investigated. When formed through secondary instability PHDs move in such a way as to increase the wave number of the pattern if it falls below the lower limit of the stability band or decrease the wave number if it is above the upper limit. PHDs are predicted to move even when the wave number is within the stable band [15]. The trajectory and speed of a single PHD are found to depend strongly on the wave numbers of two of the three individual component roll patterns that make up the hexagonal pattern. A time dependence in the motion of the PHD is found – an aspect not predicted by theoretical studies, which assume constant velocity of the PHD as an ansatz.

Experimental studies of hexagonal and other complex patterns have been hampered by difficulties encountered in imposing controlled initial conditions. A thermo-optical technique was used in these investigations to overcome that problem by thermally imprinting different hexagonal patterns as initial conditions on a BMC cell. It was coupled with shadowgraphy to measure the dynamics of the subsequent pattern evolution enabling the detailed study outlined above.

The dissertation is arranged as follows: In Chapter II some basic theory and experimental work on RBC is described. This sets a framework with which to discuss hexagonal patterns in BMC. Chapter III provides a detailed description of the experimental apparatus along with the approaches used to study the different phenomena. Chapter IV presents our experimental results and their comparison with theoretical predictions as well as conclusions and possible avenues of future study. Chapter V is a discussion of the work done and how it relates to pattern formation in general.

CHAPTER II

BACKGROUND

When a layer of liquid with a free upper surface is heated from below with a sufficient temperature gradient, the motionless conducting state is replaced with a convecting pattern of hexagons. This phenomenon, referred to as Bénard-Marangoni convection (BMC), was first discovered by Bénard in experiments conducted in 1900 [16]. Lord Rayleigh published a paper in 1916 [4] in which he attributed the convection to the buoyancy resulting from thermal expansion of liquid near the heated bottom plate. Over 40 years later Pearson [17], neglecting buoyancy, showed that hexagonal patterns could be produced by considering surface-tension gradients arising from temperature variations at the gas-liquid interface. This is the so-called "Marangoni effect" first investigated by Thomson in 1855 [18] and later by Marangoni [19]. Studies by Nield in 1964 [20] combined both the effects of buoyancy and surface tension and suggested that the two mechanisms are tightly coupled. He showed that for a large liquid depth buoyancy is the dominant mechanism driving convection while for small depths surface tension dominates. Thus he concluded that the patterns observed by Bénard were probably surface tension dominated.

The appearance of stable hexagons at the onset of BMC makes it a desirable system with which to study nonequilibrium patterns with hexagonal symmetry, analogous to the pioneering investigations by Busse *et al.* [8] on straight convection rolls in Rayleigh-Bénard convection (RBC). This chapter introduces RBC and then discusses BMC in more detail.

2.1 Rayleigh-Bénard Convection

Much of the progress in understanding nonequilibrium pattern forming systems stems from extensive theoretical and experimental work done on RBC. The following is an overview of the main concepts and results of interest to this dissertation. Extensive reviews are presented in Refs. [21, 22]. RBC bears some similarities to BMC and serves as a useful

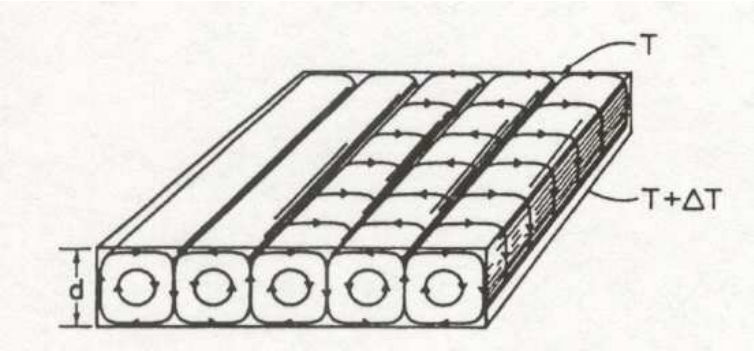

Figure 1: Illustration of fluid stream lines of straight convection rolls in RBC. (From Cross and Hohenberg [7].)

system with which to compare results of our investigations. Unlike in BMC, there is no free surface in RBC, thus the sole mechanism that drives convection is the temperature difference, ΔT, across the fluid. The buoyancy force per unit volume is given by $\rho\alpha g\Delta T$ where ρ, $\alpha = -\rho^{-1}\partial\rho/\partial T$ and g are, respectively, the average density, thermal expansion coefficient and acceleration due to gravity [21]. Opposing convection is the viscous friction of the fluid along with the relaxation of temperature gradients due to heat diffusion. The kinematic viscosity $\nu = \eta/\rho$, where η is the dynamic viscosity, gives a measure of the viscous damping, while the thermal diffusivity κ quantifies the thermal damping. Associated with the buoyancy is a characteristic time τ_B, obtained from the buoyancy force by considering

$$\text{buoyancy force per unit volume } = \rho \times \text{acceleration}.$$

Then τ_B is defined by

$$\rho\alpha g\Delta T = \rho\frac{d}{\tau_B^2},$$

where d is the fluid depth. The characteristic times τ_η and τ_θ for kinematic viscosity and thermal diffusivity respectively are defined from $\nu = d^2/\tau_\eta$ and $\kappa = d^2/\tau_\theta$. Thus the control parameter for RBC is the Rayleigh number defined as $R = \tau_\eta\tau_\theta/\tau_B^2 = \alpha g\Delta T d^3/\nu\kappa$, *i.e.*, the ratio of the stabilizing and destabilizing time scales. When R is small, the response time of the damping is faster than the time it takes for a warm bubble to rise so convection is suppressed; and for sufficiently large R the opposite is true and convection results. In large aspect ratio systems, *i.e.*, $L/2d \gg 1$ (where L is the lateral length of the convection cell of

depth d) convective onset occurs at $R \simeq 1708$. Translational symmetry in the plane leads to a convection pattern of periodic rolls with a wave vector $\mathbf{q}$, which breaks the symmetry of the uniform state (Fig. 1). For $R > 1708$ the wave number q of the rolls is selected from a narrow range of allowed wave numbers centered around $q_0 \simeq 3.117/d$ [7]. From a physical standpoint the limited range in q of stable rolls can be understood by considering the following: For $q < q_0$ the rolls are flat and have excess thermal dissipation at the top and bottom plates arising from increased horizontal motion; while for $q > q_0$ the rolls are tall and thin resulting in excess vertical shear. Thus for any fixed R across a fluid of Prandtl number $Pr = \nu/\kappa = \tau_\theta/\tau_\eta$, the ratio of the strengths of the two damping mechanisms, there is a narrow finite region of stability. This region is characterized by the "Busse balloon" obtained theoretically and through experiments by Busse et al. [8] in the late 1960s and early 1970s. Fig. 2 shows a slice of the Busse balloon at $Pr = 7$. When straight rolls have q at the edge of the region of stability they become unstable through one of a number of several distinct mechanisms that depend on R, Pr and on which side of the stable region q is.

2.2 Bénard-Marangoni Convection

The control parameter that measures the strength of surface tension driving in BMC is the Marangoni number $M = \sigma_T \Delta T d/\rho\nu\kappa$, where σ is the surface tension and $\sigma_T \equiv \frac{d\sigma}{dT}$; d, ρ, ν, κ are respectively, the liquid's thickness, density, kinematic viscosity, and thermal conductivity. With $\sigma_T < 0$, surface tension gradients draw fluid from warm areas at the liquid-gas interface to cool areas. Due to mass conservation this creates upflows at the locally warm spots and downflows at the cool areas (Fig. 3). As in the case of the Rayleigh number, R, the Marangoni number, M, is the ratio $\tau_\eta\tau_\theta/\tau_{th}^2$ of the stabilizing and destabilizing time scales, where $\tau_{th}^2 = \rho d^3/\sigma_T\Delta T$ is the destabilizing thermocapillary time scale. For large enough M ($\simeq 80$) thermocapillarity is sufficiently strong to overcome the damping due to viscosity and heat conduction resulting in convection. Unlike in the case of RBC there is no inversion symmetry in the vertical direction about the mid-plane of the liquid layer and consequently the equations of motion are not invariant under a reversal of the fluid

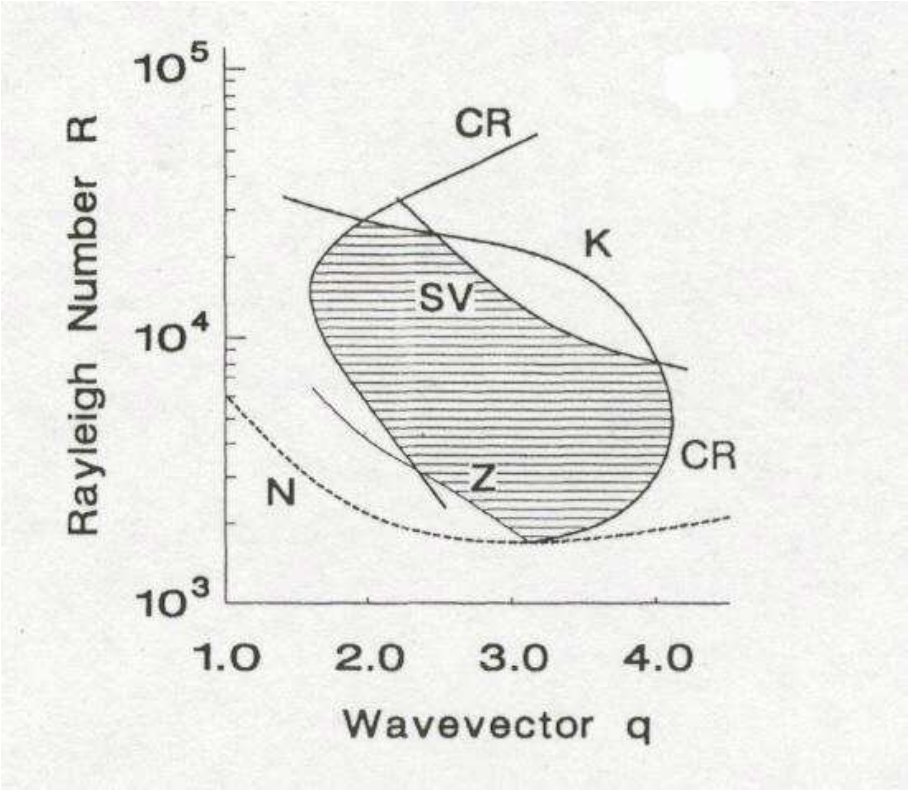

Figure 2: Stability diagram for rolls in RBC. The shaded region represents the parameter range in Rayleigh number R and wave number q space at fixed Prandtl number $Pr = 7$ for which straight rolls are stable. The region is bounded by secondary instabilities of the roll states: Z - zig-zag, CR - cross-roll, K - knot and SV - skewed-varicose. The dashed line labeled by N is the neutral stability curve above which convection occurs. (From Cross and Hohenberg [7].)

velocity variables. Thus three roll patterns arising from the translational symmetry in the lateral direction couple resonantly to form a pattern of hexagons [23]. A perfect hexagonal pattern can be considered as a superposition of three roll systems $A_j e^{i\mathbf{q}_j \cdot \mathbf{r}}$, for $j = 1, 2, 3$, and $\mathbf{r} = (x, y)$. The $\mathbf{q}_j$ are the wave vectors of the roll patterns and are oriented 120° with respect to one another. They satisfy the resonance condition $\mathbf{q}_1 + \mathbf{q}_2 + \mathbf{q}_3 = \mathbf{0}$. To the lowest order in the small parameter $\epsilon = (M - M_c)/M_c$, which is a nondimensional representation of the control parameter M, the following equations for the amplitudes of the rolls can be written from symmetry considerations [25] (assuming $q_1 = q_2 = q_3$):

$$\partial_t A_i = \epsilon A_i + \alpha {A_j}^* {A_k}^* - (|A_i|^2 + \gamma |A_j|^2 + \gamma |A_k|^2) A_i,$$

with $\{i, j, k\} = \{1, 2, 3\}, \{2, 3, 1\}, \{3, 1, 2\}$. The A_j are $O(\epsilon^{1/2})$ and γ is $O(1)$. The coefficient of the inversion symmetry breaking quadratic term α is $O(\epsilon^{1/2})$. The cubic terms prevent unbounded growth of the amplitudes due to the linear and quadratic terms. For non-ideal patterns additional terms that describe the spatial variation in the amplitudes must be included. To lowest order in ϵ this variation is described by the term $(\hat{\mathbf{n}}_j \cdot \nabla)^2 A_j$ where $\mathbf{n}_j$ is the unit vector parallel to wave vector $\mathbf{q}_j$. Thus

$$\partial_t A_i = \epsilon A_i + \alpha A_j^* A_k^* - (|A_i|^2 + \gamma |A_j|^2 + \gamma |A_k|^2) A_i + (\hat{\mathbf{n}}_i \cdot \nabla)^2 A_i, \tag{1}$$

The variables can be rescaled so that the coefficient of the quadratic terms is equal to one by introducing a new parameter $\mu = \epsilon/\alpha^2 = O(1)$ and amplitude $\widetilde{A} = A/\alpha$. The time variable becomes $T = \alpha^2 t$ and the spatial variables are rescaled as $X_j = \alpha x_j$ and $Y_j = \alpha y_j$. The equations then become

$$\partial_T \widetilde{A}_i = \mu \widetilde{A}_i + \widetilde{A}_j^* \widetilde{A}_k^* - (|\widetilde{A}_i|^2 + \gamma |\widetilde{A}_j|^2 + \gamma |\widetilde{A}_k|^2) \widetilde{A}_i + (\hat{\mathbf{n}}_i \cdot \nabla)^2 \widetilde{A}_i, \tag{2}$$

where in this case $(\hat{\mathbf{n}}_j \cdot \nabla)^2 = \partial_{X_j}$.

As mentioned at the beginning of the chapter the effects of buoyancy must also be taken into account when considering BMC. It has been suggested that buoyancy dominated convection yields qualitatively different regions of stable hexagons in the (M, q) plane than does surface tension dominated convection [26]. Thermocapillarity is considered dominant when $M/R = \rho\nu\kappa/\sigma_T \Delta T d^2 > 1$. The simplest way to control this ratio is by adjusting

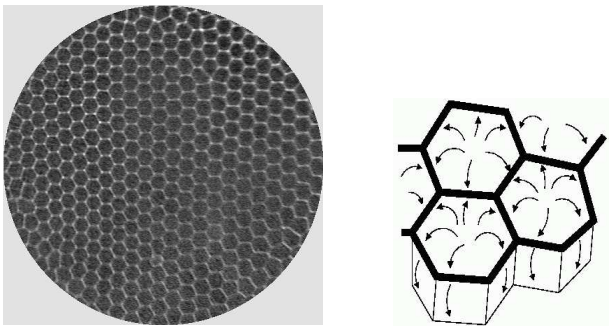

(a) (b)

Figure 3: Liquid upflow in a pattern of BMC. (a) Shadowgraph image of a pattern of hexagons. Warm liquid flows upward in the dark cell centers and flows downward at the white cell edges. (b) Schematic of the liquid flows.

the liquid depth d. Thus, as asserted by Nield, [20] buoyancy driving is dominant for thick liquid layers while thermocapillarity is the primary driving mechanism when d is small. For thinner depths still, the patterns become qualitatively different. In that case short wavelength temperature perturbations are quickly damped (since $\tau_\theta = d^2/\kappa$), but the gravitational time scale $\tau_{grav}^2 = d/g$ is large enough that long wavelength deformations due to thermocapillarity are not damped quickly enough and draw fluid away from the center of the convection cell creating a large dry spot [27]. The relevant parameter for determining which pattern appears is the Galileo number $G = gd^3/\nu\kappa = \tau_\eta\tau_\theta/\tau_{grav}^2$. For large enough G gravity responds quickly enough to flatten out deformational perturbations and hexagons are the expected planform. Fig. 4 shows the different neutral stability curves for convection when G is large and when G is small.

2.2.1 Stability Region

Externally driven stationary periodic hexagonal patterns are expected, as in the case of rolls in RBC, to have a finite region of stability. Estimates of its size and shape have been made by Echebarria and Pérez-Garciá [13], and Young and Riecke [14] using amplitude equations, which only consider the essential symmetries of the problem. Bestehorn [26] has computed the region for hexagons formed in BMC using the relevant governing equations. The main ideas behind that analysis are outlined below.

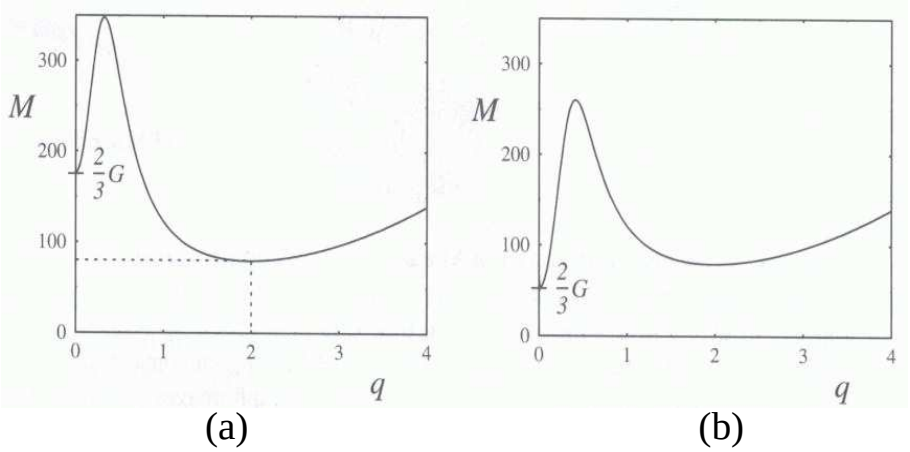

Figure 4: Neutral stability curves for two different types of instability in BM convection. M is the Marangoni number and q is the wave number of the instability. (a) As M is raised from zero the onset of convection is to patterns of $q \approx 2$ indicated by the global minimum of the neutral stability curve. (b) For sufficiently thin liquid depths d the global minimum is at $q = 0$ and a long wavelength deformation of the liquid is the primary instability. (From Schatz and Neitzel[28].)

The equations that describe BMC are the Navier-Stokes equations, the continuity equation and the equation for the temperature field which are respectively,

$$\rho[\partial_t \mathbf{v} + \mathbf{v} \cdot \nabla \mathbf{v}] = \rho g \hat{\mathbf{z}} - \nabla p + \eta \Delta \mathbf{v}, \tag{3}$$

$$\nabla \cdot \mathbf{v} = 0, \tag{4}$$

$$\partial_t T + \mathbf{v}.\nabla T = \kappa \Delta T, \tag{5}$$

where $T = T(\mathbf{r}, t)$ is the temperature field, $\mathbf{v} = \mathbf{v}(\mathbf{r}, t)$ is the velocity field, $p = p(\mathbf{r}, t)$ is the pressure field and η is the viscosity. Bestehorn uses the Boussinesq approximation, which assumes the variation of the density with temperature can be neglected except for the buoyancy term of the Navier-Stokes equations where it is assumed to be linear. Thus

$$\rho(T) = \rho_0\{1 - \alpha[T(\mathbf{r}, t) - T_0]\}, \tag{6}$$

where T_0 is the temperature of the bottom plate. The velocity field is divergence-free and can be decomposed as

$$\mathbf{v} = \nabla \times (\phi \hat{\mathbf{z}}) + \nabla \times \nabla \times (\psi \hat{\mathbf{z}}), \tag{7}$$

where $\phi = \phi(\mathbf{r}, t)$ and $\psi = \psi(\mathbf{r}, t)$ are scalar fields. Denoting the variation of the temperature

from the linear profile by $\Theta = \Theta(\mathbf{r}, t)$ and eliminating the pressure by taking the curl and twice the curl of the Navier-Stokes equations yields

$$\left\{\Delta - \frac{1}{Pr}\partial_t\right\}\Delta\Delta_2\psi = R\Delta_2\Theta - \frac{1}{Pr}[\nabla \times \nabla \times (\mathbf{v}\cdot\nabla\mathbf{v})]_z, \tag{8}$$

$$\left\{\Delta - \frac{1}{Pr}\partial_t\right\}\Delta_2\phi = -\frac{1}{Pr}[\nabla \times (\mathbf{v}\cdot\nabla\mathbf{v})]_z, \tag{9}$$

$$[\nabla - \partial_t]\Theta = \Delta_2\psi + \mathbf{v}\cdot\nabla\boldsymbol{\Theta}, \tag{10}$$

where $Pr = \eta/\rho_0\kappa$, $\Delta_2\phi = \partial_{xx} + \partial_{yy}$ and R is the Rayleigh number. Time and length have been scaled by $\tau_\theta = d^2/\kappa$ and the depth d respectively. Assuming vanishing velocity components at the fixed boundaries, Eq. (7) leads to

$$\phi(\mathbf{r}, t) = \psi(\mathbf{r}, t) = \partial_n\psi(\mathbf{r}, t) = 0 \tag{11}$$

for $\mathbf{r}$ on the bottom and at the vertical walls. The vertical walls also have

$$\partial_n\phi(\mathbf{r}, t) = 0, \quad \Delta_2\psi(\mathbf{r}, t) = 0. \tag{12}$$

Boundary conditions for the temperature field can be written as

$$\partial_z\Theta(\mathbf{r}, t) = \begin{cases} Bi_0\Theta(\mathbf{r}, t) & \text{for } z = 0 \\ -Bi_1\Theta(\mathbf{r}, t) & \text{for } z = 1 \end{cases}$$

where Bi is the Biot number, the ratio of the thermal conductivity of the boundary wall to that of the fluid. For a perfectly conducting boundary $Bi \to \infty$, and for a poor conductor $Bi \ll 1$. Assuming a perfectly conducting bottom boundary $Bi_0 \to \infty$, while for the poorly conducting air boundary the Biot number is taken as $Bi_1 \approx 0.1$. The velocity field and the temperature field at the free surface ($z = 1$) are linked by

$$\partial_z\phi(\mathbf{r}, t) = 0, \quad \psi(\mathbf{r}, t) = 0, \quad \partial^2{}_z\psi(\mathbf{r}, t) = -M\Theta(\mathbf{r}, t).$$

Assuming $Pr \to \infty$ Eq. (10) becomes

$$\Delta\Delta_2\phi(\mathbf{r}, t) = 0,$$

which together with boundary conditions, Eqs. (11) and (12), leads to

$$\phi(\mathbf{r}, t) = 0,$$

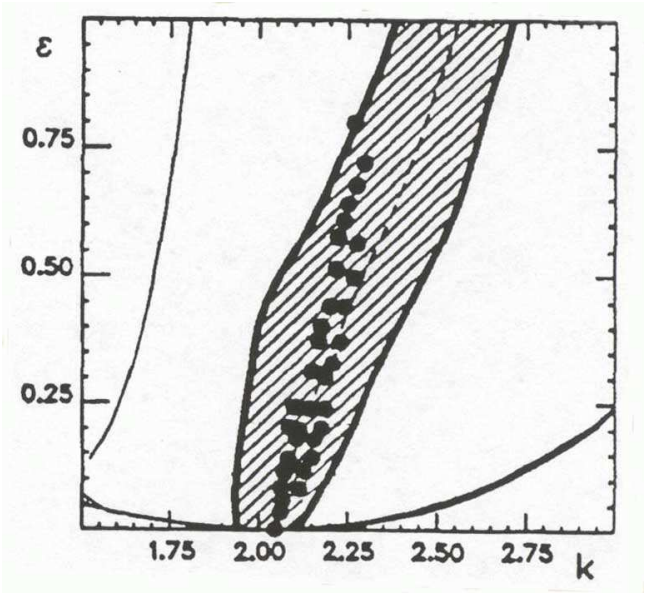

Figure 5: Theoretical prediction of the stability band for hexagons in BMC [26] for $Pr \to \infty$ and $\Gamma \approx 2.7$ in ϵ-k space. $\epsilon = (M - M_c)/M_c$ and k is the wave number. Hexagons are stable in the shaded region bounded by phase instabilities. The dots are experimental data obtained from [30]. The line near the bottom is the neutral stability curve; the line at left corresponds to amplitude instabilities. (From Bestehorn [26])

throughout the liquid. Thus only two dependent variables ψ and Θ remain.

The solutions $\psi(\mathbf{r}, t)$ and $\Theta(\mathbf{r}, t)$ of the basic Eqs.(9)-(10) are projected onto eigenfunctions of their linearized form to obtain a large set of coupled ordinary differential equations of the eigenfunction amplitudes. By the slaving principle the linearly damped modes are eliminated, leaving a smaller system of amplitude equations which can be studied in detail. One particular solution of the reduced equations is that of hexagons. The stability of hexagon solutions as a function of their wave number k was computed by Bestehorn who obtained the stability boundaries plotted in Fig. 5.

At the boundaries of the stability region the hexagon solutions are found to be unstable to phase perturbations. However, unlike the case of the Busse balloon, where the forms of the perturbations that lead to the instability of straight rolls have been determined, the mechanisms of instability for hexagons have not been identified in Bestehorn's study. Other researchers (Echebarria and Pérez-Garciá [13], and Young and Riecke [14]) have suggested

forms for secondary phase instabilities in hexagonal patterns by starting considering amplitude equations. The results of their analyses, which are outlined in Chapter IV, form the basis of the experimental investigation. Until now no comprehensive experimental measurements have been been carried out to measure either the boundaries of the stable band or to determine the secondary phase instabilities for hexagons.

Much of the progress in pattern formation has been through experimental studies of fluids. The clear advantages of fluid systems are that their governing equations are well known, which allows quantitative comparisons with complementary theoretical studies. Accurate and convenient techniques have been developed in recent years for measurement of fluid flows at multiple spatial points in time. However, fluids experiments are typically limited by difficulties in the control of their initial conditions. Thus quantitative study of phenomena such as secondary instability, that require the probing of a range of initial conditions, is often lacking. For the investigations of this dissertation a novel thermo-optical technique that exploits the main driving mechanism of BMC is used to impose a variety of initial conditions and is described in the next chapter. Coupled with shadowgraph measurements, it enables investigation of hexagons analogous to the straight roll studies in RBC of 30 years ago [8].

CHAPTER III

EXPERIMENTAL SETUP

3.1 Apparatus

The experimental setup (Fig. 6) is designed to enable thermo-optical imprinting of a pattern that sets an initial condition on a Bénard-Marangoni convection cell, along with noninvasive tracking of its subsequent evolution. The setup is divided into three main subsystems: the BM convection-cell assembly (Fig. 7); the fluid-flow-visualization subsystem (Fig. 10); and the flow-manipulation subsystem (Fig. 14), all of which are connected to a central computer. The convection-cell and flow-measurement subsystems are well developed and have been used extensively by other researchers [10, 29, 30]. The unique capability of this experimental setup lies in its ability, provided by the flow manipulation subsystem, to impose controlled initial conditions through rapid multi-point actuation of liquid flows. The discussion below starts with a description of the BM convection cell and then details the visualization subsystem, before finally describing the technique used to impose controlled patterns.

3.1.1 Bénard-Marangoni Convection Cell

The convection cell consists of a thin silicone-oil layer, used as a test liquid, that is heated uniformly from below by a metal mirror and cooled from above by a thin air layer sandwiched between the silicone oil and a liquid cooled window (Fig. 7). The convection cell is on a platform that is mounted on top of three fine adjustment screws, arranged in an equilateral triangle, to enable precise leveling of the silicone-oil layer. The cooled window is part of a separate platform that is mounted on similar screws to allow fine control of the thickness of the air layer.

The silicone oil is chosen because of its low susceptibility to surfactants which would otherwise significantly alter its surface-tension properties, and hence the dynamics of the

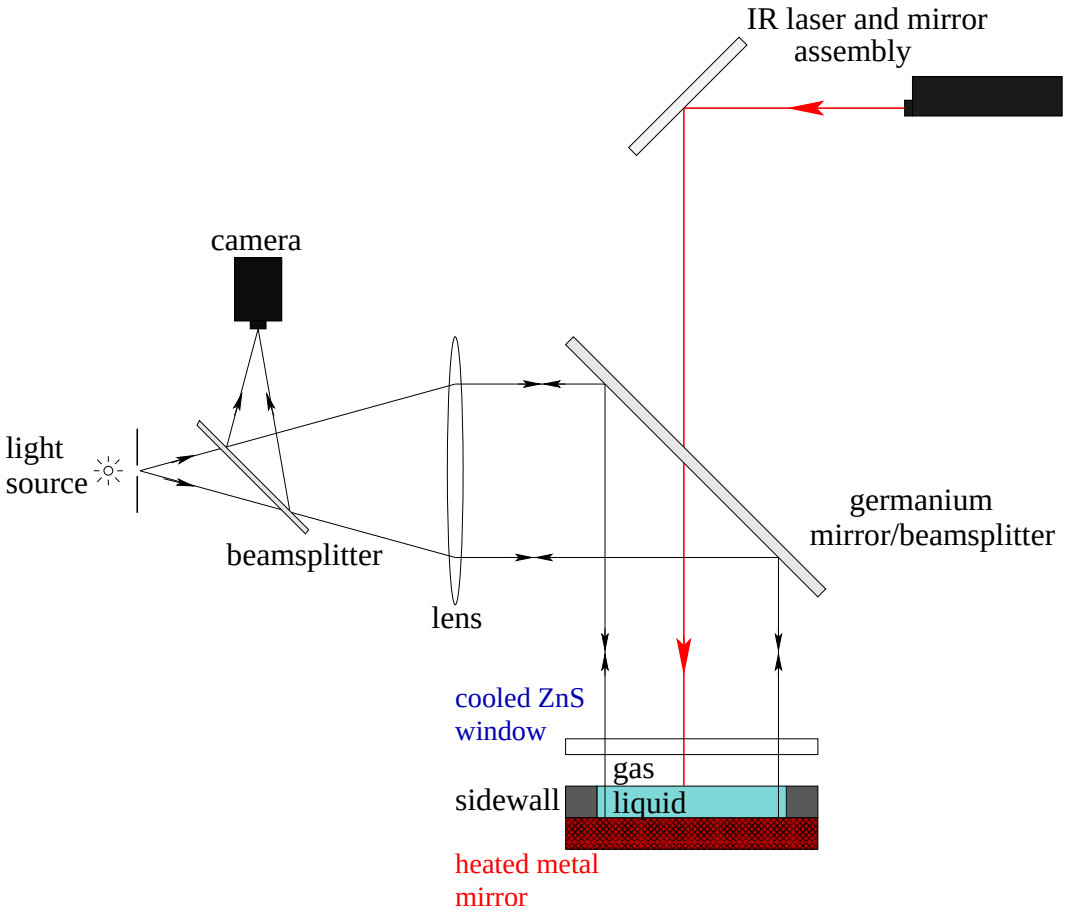

Figure 6: Schematic of the general setup of the experiment. The infrared laser and mirror assembly enable rapid local heating of the gas liquid interface. The light source along with a camera and other optics are used for shadowgraph visualization of the convective liquid flows.

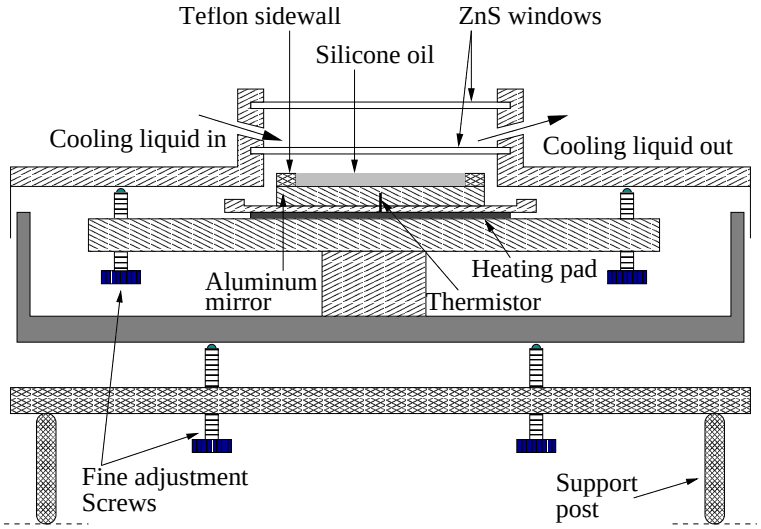

Figure 7: General setup of the cell assembly. A heating pad below the aluminum mirror sets the bottom temperature while circulating cooled carbon disulfide maintains the top temperature. The bottom set of fine adjustment screws levels the liquid and the top set controls the thickness of the air gap.

fluid flows. It has the additional advantage of being available in a range of Prandtl number $Pr = \nu/\kappa = \tau_\theta/\tau_\eta$, which defines the ratio of the thermal and viscous dissipative time scales. In the experiments $Pr = 87.25$, *i.e.*, the velocity dissipation due to viscosity is much faster than the dissipation of heat by conduction. The silicone-oil depth is $d = 0.98 \pm 0.01$ mm, which sets the time scale $\tau_v \equiv \tau_\theta = d^2/\kappa = 10.2$ s of the experiments. (Time scale τ_v is typically taken to be the larger of τ_θ and τ_η – in this case $\tau_\eta = 0.12$.) The layer is confined by a sidewall of inner diameter of 76.2 ± 0.01 mm yielding an aspect ratio of 38.9. The bottom plate of the cell is a 76 mm diameter and 12.5 mm thick polished aluminum mirror whose surface varies in height by $\sim$100 Å. A flat mirror is necessary for shadowgraphy and for leveling of the cell by interferometry. The mirror is placed concentrically inside an aluminum ring of the same thickness but with a slightly larger inner diameter. A hole is drilled into the side of the ring to accommodate a 20-gauge Teflon tube whose other end is attached to a syringe used to inject silicone oil into the cell (Fig. 8). On top of the ring is a 1 mm thick and 6.35 mm wide ring of Teflon that serves as the sidewall. Teflon is used instead of aluminum because its thermal conductivity ($\sim 20 \times 10^3$ erg s^{-1} cm^{-1} K^{-1}) is more closely matched to that of silicone oil (13.3×10^3erg s^{-1} cm^{-1} K^{-1}) than aluminum's

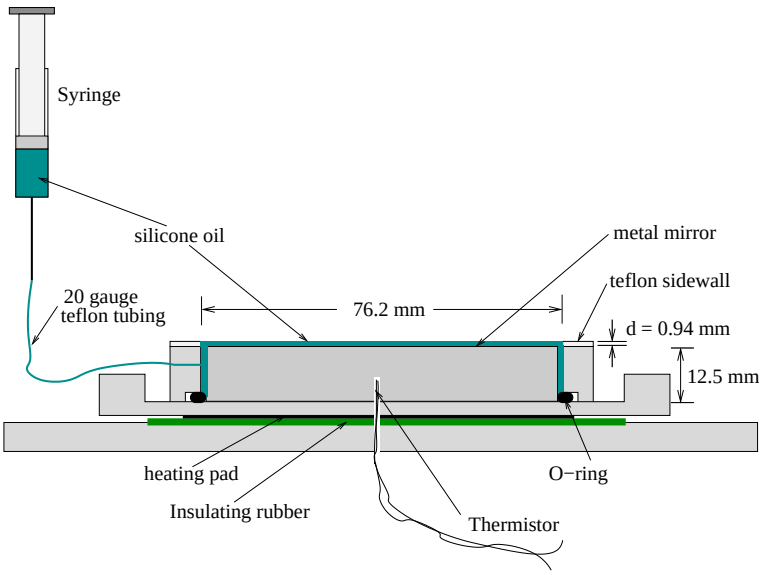

Figure 8: Closeup of the bottom plate. The thermistor is placed in the center of the aluminum plate with some heat-sink compound to ensure accurate temperature readings. The Teflon tubing attached to the syringe allows controlled filling of the cell with silicone oil.

is ($\sim$23,000$\times 10^3$erg s^{-1} cm^{-1} K^{-1}).

Leveling of the silicone oil is achieved through interferometry: A 632.8 nm helium-neon laser beam is expanded through a spatial filter and directed at the convection cell. The laser light that reflects off the flat mirrored bottom plate interferes with the light that reflects of the surface of the silicone oil and forms fringes whose separation increases as the angle between the silicone-oil surface and the mirror decreases. The silicone-oil depth d is then leveled using the three fine adjustment screws – the 4 mm diameter ball bearings at the top of the screws fit snugly into machined grooves at the base of the platform which has an additional screw at its center to secure it. The leveling can decrease the number of fringes to $\sim$5 across the diameter of the cell making the depth uniform to within $\sim 10^{-3}$mm. Interferometry is also used to ensure a uniform gap between the mirrored bottom plate and the bottom window and set the air gap at $d_g = 0.97 \pm 0.01$ mm. The silicone-oil depth is measured with a vernier attached to a needle. The needle is lowered until it touches the surface of the silicone oil – an event made abrupt by the capillary action of the silicone oil on the needle. The reading on the vernier is noted before lowering farther it until it touches

the metal mirror. Contact is established accurately by forming a circuit that includes the mirror, the needle and a digital multimeter and noting the vernier reading when the resistance drops sharply.

Heating from below is with a thin flat 18Ω (Minco) resistive heating pad, which at normal operating temperatures provides ∼7 W of power. The high thermal conductivity of aluminum coupled with heat-sink compound placed between the heater and the metal mirror ensure uniform heating of the silicone oil. A rubber insulator is placed below the heater to reduce heat loss. The heater is connected to a Kepco ATE-36-3M power supply that is, in turn, connected to the main computer through a National Instruments LabPC Card that can be instructed to output 0-10 V. The power supply is configured to output a voltage that varies as a multiple of an input voltage thus providing sufficient power to the Minco heating pad. The temperature T_b of the bottom plate is measured with a thermistor placed inside a hole drilled in the bottom of the mirror. Heat-sink compound placed in the hole with the thermistor ensures accurate temperature reading. The thermistor is connected to a Hewlett Packard 34401A multimeter that can be configured to be periodically read by the computer. Using the thermistor readings and the heater, the bottom plate can be maintained at a range of temperatures within 0.005°C using proportional-integral-derivative control (Appendix A).

The temperature $T_t = 22.39 \pm 0.03$°C of the cooled-ZnS window is maintained by circulating carbon disulfide (CS_2) in a closed loop system that includes a pump and a heat exchanger (Fig. 9). The windows are made of ZnS Cleartran® with anti-reflection coating at 10.6 μm, which together with the circulating CS_2, allow both visualization of the fluid flows and optical access to the silicone oil by the infrared laser beam used to impose initial conditions. To keep the toxic, small-molecule CS_2 from escaping the closed system, fittings and tubing from Swagelok, specially designed to provide a tight seal, are used. The system is leak-checked with helium, a smaller molecule than CS_2, before filling it. Because CS_2 is a strong solvent, the tubing is made from PFA (perfluoroalkoxy), all O-rings are made of Viton®, and the pump housing is made from glass filled Ryton® (polyphenylenesulphide). The CS_2 circulates through a reservoir to remove bubbles, and then through a copper coil

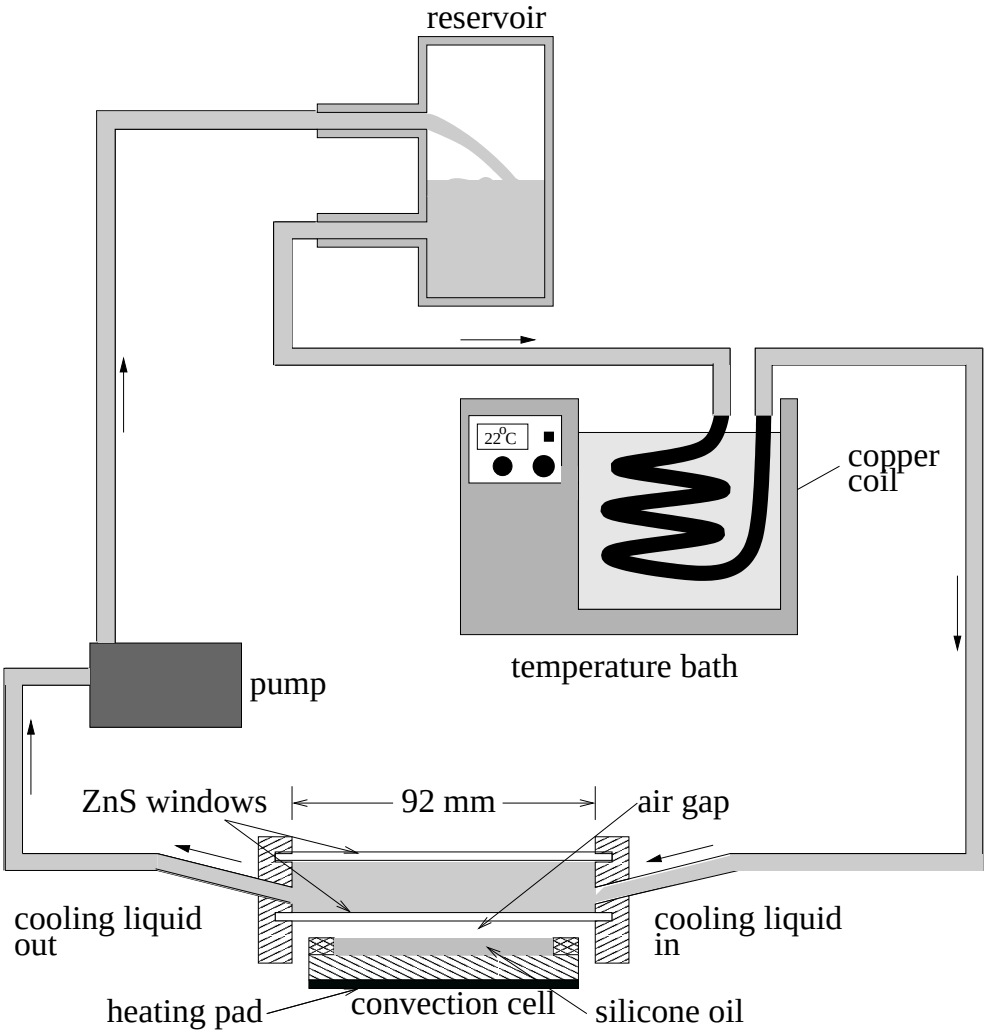

Figure 9: Schematic of the cooling system. CS_2 is pumped through a heat exchanger placed in temperature bath. The reservoir is set up to remove air bubbles from the system.

immersed in a Neslab RTE 210 temperature bath before returning to the cooled windows.

A convective pattern forms when the temperature difference ΔT across the liquid layer is 1.44°C. Because a thermistor cannot be placed in the silicone oil without disturbing it, ΔT is estimated from $\mathrm{T_b}$ and $\mathrm{T_t}$ by assuming that heat transport is solely by conduction in both the gas and liquid layers. Thus

$$\Delta \mathrm{T} = \frac{\mathrm{T_b} - \mathrm{T_t}}{1 + \frac{d_g k}{d k_g}},$$

where $k = 13.3{\times}10^3$erg s^{-1} cm^{-1} and $k_g = 2.76{\times}10^3$ erg s^{-1} cm^{-1} K^{-1} are the liquid and gas thermal conductivities respectively. Thus at onset $\mathrm{M}_c = 86$, which compares well with Pearson's theoretical estimate of $\mathrm{M_c} = 80$ [17], and a measurement of $\mathrm{M_c} = 84$ by Schatz *et al.* [31]. Close to onset, thermal driving of the sidewall [31] causes a pattern of concentric rings to form near the boundary. The rings are replaced by hexagons in a localized area after an increase in ΔT of $\sim 10^{-3}$K. More hexagons form in a front that propagates across the entire silicone-oil layer resulting in a pattern of unique wave number $q_0 = 2\pi d/\lambda \approx 2$.

3.1.2 Flow Visualization

Flow visualization is achieved non-invasively using shadowgraphy [10]. Light from a halogen lamp is passed through a pinhole located at the focal point of a large lens where it emerges normal to the mirrored bottom plate (Fig. 10). The light reflects off the mirror and is redirected on its return path to a CCD camera connected to a frame-grabber in the main computer. Along their trip the light rays pass through the silicone oil. The temperature-induced density variations in the silicone oil cause refractive-index gradients which result in a lensing effect – light is bent away from warm areas of locally low refractive index toward cool areas of locally high refractive index creating an image of varying intensity at the CCD camera (Fig. 11). The optics can be tuned such that the dark areas correspond to warm regions while the light areas correspond to cool areas of the silicone oil. The index of refraction coefficient $n_T = -(\partial n/\partial T)_p$ in liquids is typically of the order of 10^{-4}K^{-1} making shadowgraphy a very sensitive technique for detecting temperature variations, and hence, fluid flows.

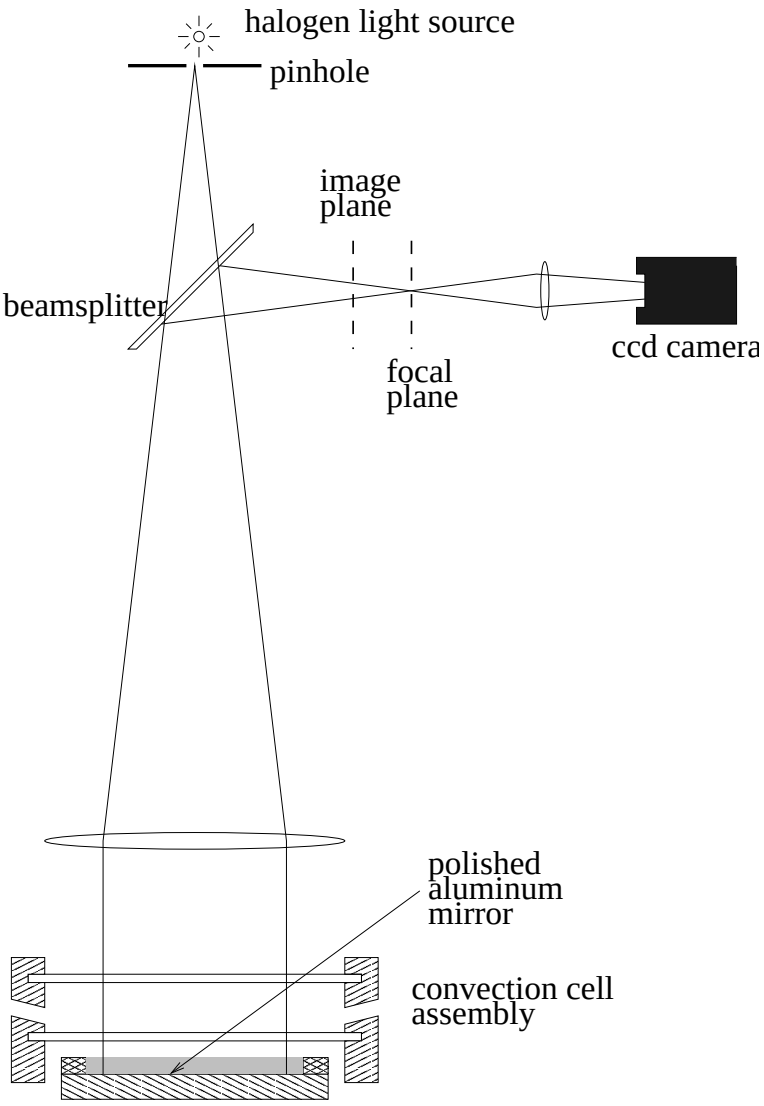

Figure 10: Schematic of shadowgraph setup.

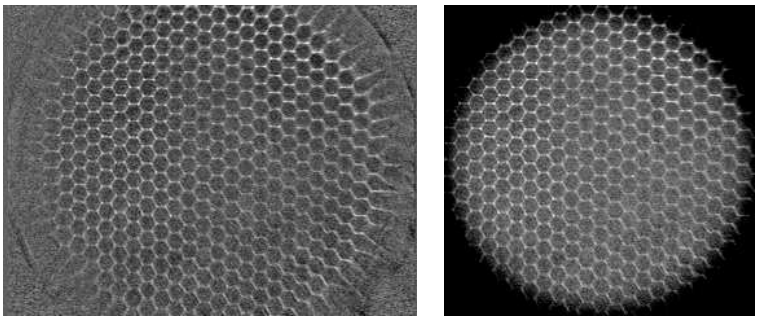

(a) (b)

Figure 11: (a) A typical 320×240 shadowgraph image captured from CCD camera. A background image taken with no pattern present has been subtracted to enhance the image. (b) The same image cropped to 240×240 and masked with a circular window that has a smooth transition to zero.

The optical path of the shadowgraph is illustrated in Fig. 10. When the camera's image plane is focused such that a real image of the plane of the liquid surface is formed, the sensitivity is zero and no convection pattern is observed. Thus the image plane should be above or below the plane of the liquid surface to improve sensitivity – the resulting shadowgraphs are negatives of each other. However, imaging too far above the surface introduces image distortion as the shadowgraph response becomes nonlinear near "caustics". Caustics are features that appear in a shadowgraph image that do not correspond to any characteristic of the pattern. They form at the focal length of the convective pattern when refracted light rays leaving the convection cell and intersect (Fig. 12).

A frame-capture card and accompanying software are used to extract and save digital images from the CCD camera – typically 320×240 pixels, but occasionally 640×480 pixels if greater resolution is desired. The 320×240 pixel images are cropped appropriately to 240×240 and multiplied with a circular window that has a smooth cutoff to remove the boundary region and the portion of the pattern distorted by it (Fig. 11). Images that are 640×480 pixels are cropped to 480×480 pixels. A background image taken when the control parameter is below onset is subtracted from the patterned images to improve the signal to noise ratio. The images are then analyzed using techniques described in section 3.2.1.1.

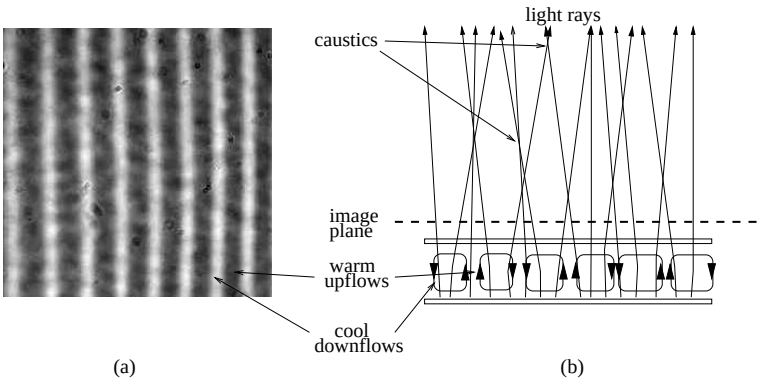

Figure 12: A shadowgraph image of straight convection rolls in RBC (a), and a side view illustration of the paths taken by light rays emerging from the convection cell. Caustics arise in regions near the focal point of the pattern where light rays intersect, and appear in a shadowgraph image as regions of increased intensity.

3.1.3 Flow Manipulation

Control of experimental initial conditions is achieved through selective localized heating of a grid of points (Fig. 13(a), (c)) at the liquid-gas interface with a 10.6 μm Synrad CO_2 infrared laser beam. At that frequency the laser light is tuned to be absorbed at the surface of the silicone-oil layer [32]. The technique directly alters the liquid flow by reducing the surface tension at the heated spots thereby drawing liquid away to the cooler unheated regions. After repeated lasing of the same points, the heated spots become regions of liquid up-flow and a pattern is established (Fig. 13(d)). The technique is distinct from that used by Busse *et al.* [8] to impose straight convection rolls with a prescribed wave number in Rayleigh-Bénard convection (RBC). With that method a pattern is imposed by passing light from a 500 watt light bulb through a mask of roll patterns. The buoyancy of the heated regions is increased, resulting in upward fluid flow. The technique is less effective in Bénard-Marangoni convection (BMC) because the air layer above the liquid becomes heated by the lamp, leading to perturbations of the surface temperature and distortion of the pattern [29].

The laser beam is rastered across the liquid surface employing a scanning technique commonly used in laser-light shows. For this experiment a General Scanning Inc. DE3000 assembly whose main features are outlined in Fig. 14 is used. A predetermined set of

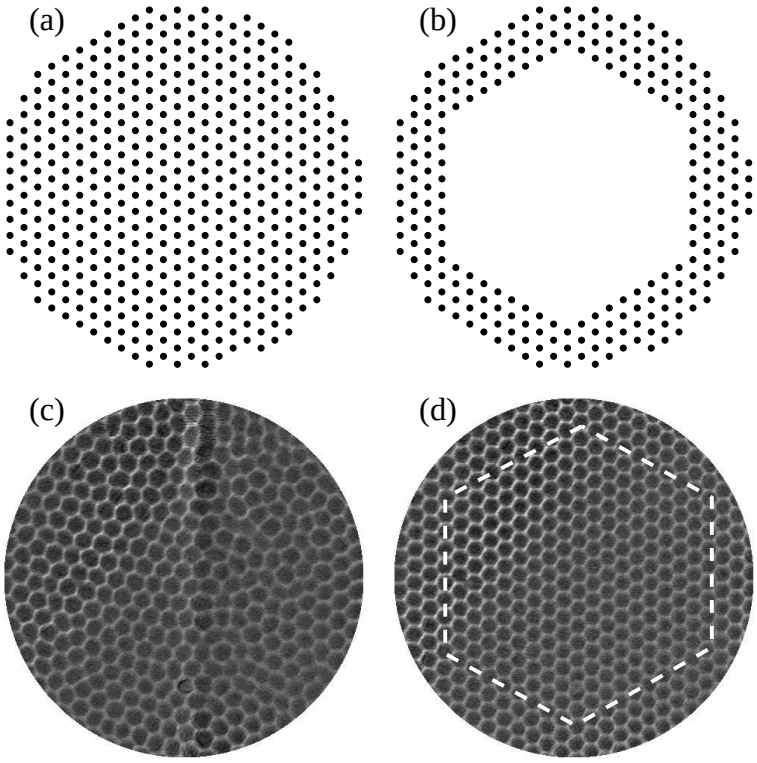

Figure 13: The process of imposing an ideal hexagonal pattern on the BMC cell. (a) Computer generated grid of points that correspond to the centers of individual hexagonal cells in the pattern. (b) The boundary points that are imposed to separate the interior dynamics from perturbations due to the cell apparatus wall. They are the same points as in (a) minus the interior 75%. (c) The infrared laser rapidly scans across the free surface layer from right to left. The dark vertical line indicates the current position of the laser. (d) A perfect pattern formed after several passes by the laser beam. The dashed line indicates the boundary of the lased points in (b).

coordinates and commands is input serially from a computer through the RS232 port or through an 8-bit parallel port to a beam-position controller (BPC). The BPC outputs a stream of X and Y coordinates to a pair of digital-to-analog converters connected to servo motors (galvanometers) that move two mirrors. The mirrors deflect an incoming laser beam to the corresponding X and Y coordinates. By outputting a signal to a laser controller the BPC synchronizes the laser with the mirrors allowing it to be turned off between points. It also enables synchronous modulation of the beam intensity, although that capability is not used in our experiments. The laser intensity is adjusted asynchronously by bypassing the scanner, and connecting the laser-controller box directly to the output of a LabPC card inside a computer. The laser-beam thickness can be adjusted by a telescope which first expands then refocuses the beam.

The scanning unit accepts a range of elementary input commands that that allow flexibility in the control of the laser beam. For example, the time spent lasing each point can be made as short as 270 μs. However, there is a balance between speed and accuracy – scanning more quickly gives the finite-moment-of-inertia mirrors less time to settle down, which degrades the accuracy of the targeting, while scanning too slowly allows the pattern enough time to evolve away from the target pattern. A frequently-used command is one that directs the scanner to continuously cycle through the same input set of points. That eliminates the slow process of reloading points to the scanner, a shortcoming that has been largely resolved with faster integrated circuits in the current generation of scanning systems.

During typical operation the scanner accepts a pattern of $\sim$500 points (pairs of coordinates) and rasters them in the order in which it received them. It first prepositions the mirrors and then turns the laser on briefly, typically $\sim$3 ms, for the first point. It then positions the mirrors for the next pair of coordinates and lases again. The average time between lased points is $\sim$20 ms. With that short a duty cycle the 7 W maximum power of the laser is effectively reduced to $\sim$ 1 W. Reflections and absorption from the optics and the carbon disulfide further reduce the power that reaches the liquid-gas interface to $\sim$0.3 W. With a beam diameter of $\approx$1.5 mm the heat flux of the laser at each point is $\sim 10^{-4}\mathrm{W/mm}^2$. However, that is sufficient to alter the surface tension because infrared radiation is strongly

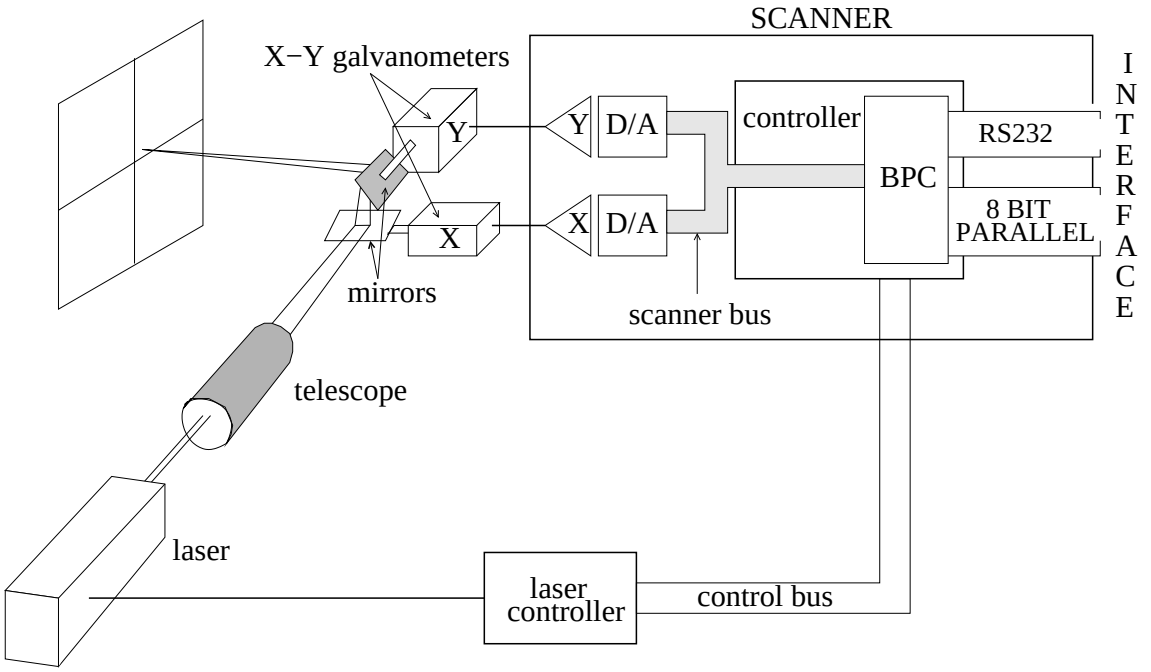

Figure 14: The main features of the laser scanning system. By controlling the laser and a pair of mirrors the scanner can direct a laser beam to selected coordinates on the target.

absorbed by silicone oil, ensuring most of the heating is at the interface where the driving occurs; and it is approximately equal to the heat flux provided by the resistive heater. The pattern is cycled through several times and usually establishes within $10\tau_v$ whereupon the lasing is turned off and within another $\sim\tau_v$ the strong thermal gradients caused by the laser dissipate thereby setting the initial conditions from which the evolution of the pattern can be studied. Lasing is continued on the outer 25% of the pattern in a hexagonal boundary to pin the cells (Fig. 13(b), (d)) otherwise new cells are created, or existing cells are destroyed, at the sidewall leading to pattern distortion.

Patterns can be imposed by two different means: either replacing an existing pattern, for $\epsilon > 0$, or by turning on the lasing when ϵ has been reduced below onset and then raising ϵ to the desired value. The latter is necessary when imposing large-wave-number patterns for operating values of $\epsilon \gtrsim 0.5$. In that case the larger wave number means a larger number of scanned points which, in turn, increases the scan cycle time to $\gtrsim \tau_v$. Thus a disturbance caused by the laser has enough time to relax away from the target state. That effect coupled with the stronger driving at large ϵ results in defects in the imposed pattern

that resist being altered. An alternative solution is to increase the laser power along with the scan rate, *i.e.*, an equipment upgrade.

The experimental apparatus has been described. Section 3.2 focuses on how the apparatus is used to investigate the three areas of interest: The region of stability for hexagons; the mechanisms that cause instability at the boundary of the stability region; and the motion of a common defect observed at the onset of secondary instability.

3.2 Methodology

3.2.1 Stable Band

Periodic patterns formed under nonequilibrium external conditions have a finite region in control parameter and wave number space for which they are stable. As described in section 2.1, the work of Busse *et al.* characterized the stable region for stationary straight rolls in Rayleigh-Bénard convection (RBC) through extensive theoretical and experimental work [8]. The three-dimensional stability region was determined for a range of the control parameter R, the Rayleigh number, and fluid Pr to form what is referred to as the "Busse balloon". Straight convection rolls were imposed for a range of wave numbers using a high-intensity lamp and then monitored for stability. For unstable wave numbers the pattern is not stationary and its wave number changes by a number of possible secondary instabilities (Fig. 2). The wave number for which secondary instability sets in marks the location of the boundary for the corresponding R and Pr.

Stationary hexagonal patterns formed under nonequilibrium external driving conditions are also expected to be stable over a finite range of wave number q and control parameter M, the Marangoni number. Bestehorn [26] calculated such a band for hexagons in Bénard-Marangoni convection (BMC) for an infinite Pr fluid (Fig. 5). Previous experimental measurements of the stability region for hexagons in BMC by Cerisier [29], using a mechanical method to set the initial conditions, reported that the patterns evolve to a unique mean wavelength. That is, no finite stability band was observed. However, the failure to find a range of stable wave numbers may have been due to boundary effects. In our experiments a stable band that is significantly smaller than that predicted by Bestehorn

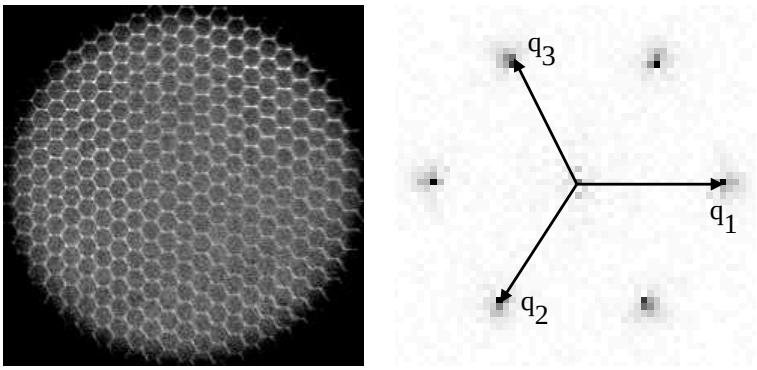

Figure 15: A hexagonal pattern (a) and the power spectrum of its Fourier transform (b).

is observed when no steps are taken to reduce the effect of fluid flows driven by the lateral boundary. The procedure discussed below details how the stability region for hexagons was measured in BMC for a control parameter range $0 \lesssim \epsilon \lesssim 1$, where $\epsilon = \frac{M-M_c}{M_c}$ is the reduced Marangoni number. The hexagons near the rigid lateral boundary where pinned by the laser to mitigate the boundary's influence on the hexagons in the interior region of the convection cell.

3.2.1.1 Creating Initial Conditions

A hexagonal pattern can be decomposed into three component roll patterns oriented 120° with respect to one another. Thus a gray-scale camera image of the pattern can be represented as

$$I(x,y) = \sum_{j=1}^{3} A_j(x,y) e^{i\mathbf{q}_j \cdot \mathbf{x}} + \text{c.c.}, \tag{13}$$

where, for an ideal hexagonal pattern, the $A_j(x,y) = A$ and $|\mathbf{q}_1| = |\mathbf{q}_2| = |\mathbf{q}_3| = q$. Computing the Fourier transform $F(q_x, q_y)$ of $I(x,y)$ using the FFT algorithm provided in the Matlab software package and displaying the power spectrum $|F|^2$ (Fig. 15) reveals six peaks whose vertices are at the centers of the vectors $\mathbf{q}_j$ and $-\mathbf{q}_j$. To extract the roll pattern associated with wave vector $\mathbf{q}_1$ the peaks at $\mathbf{q}_1$ and $-\mathbf{q}_1$ are multiplied by a circular window of suitable radius that has a smooth transition at the cutoff (such as a Butterworth filter). An inverse Fourier transform is then performed and yields the corresponding straight roll

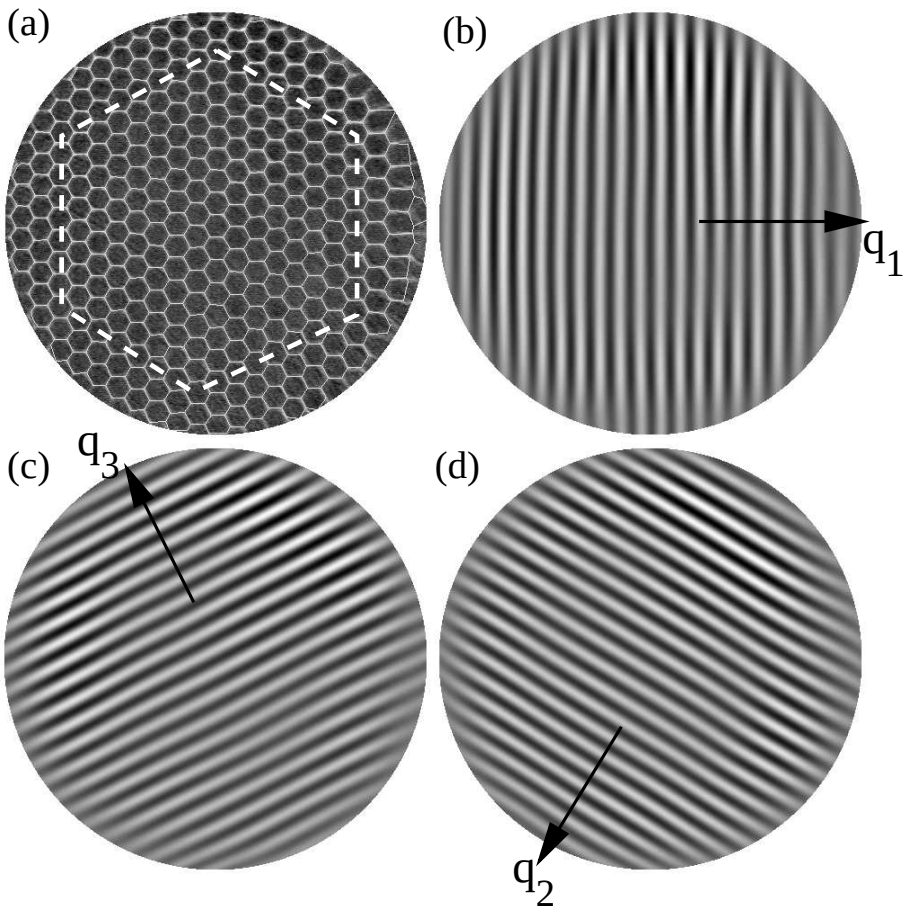

Figure 16: Decomposition of an imposed ideal hexagonal pattern into three plane waves oriented 120° with respect to one another. Each plane wave is perpendicular to two sides of the imposed boundary shown in (a) by the dashed lines. By moving opposite walls of the boundary the wave number of each plane wave can be varied by $\approx 5\%$ independently of the other two plane waves that make up the pattern.

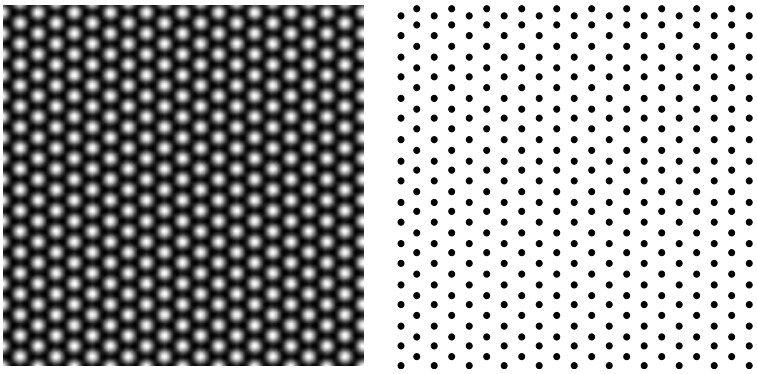

Figure 17: (a) Ideal hexagonal pattern formed by superposing three plane waves oriented 120° with respect to each other. (b) Hexagonal array of points corresponding to the centroids of the peaks of the pattern.

pattern (Fig. 16(b)). The same procedure is followed to obtain the roll patterns associated with the other two wave vectors.

To create an initial condition of regular hexagons on the BMC experiment a hexagonal array of points each corresponding to individual hexagons of the pattern must first be generated. The array is created by superposing three plane waves oriented 120° with respect to one another and then determining the coordinates of the centroids of the peaks of the resulting pattern (Fig. 17). By adjusting the coordinates, the wave number of each of the individual component rolls of the imposed patterns can be set. This involves stretching or squeezing the array of points uniformly in a given direction to adjust the wave number of the component rolls of the imposed patterns relative to each other, and then multiplying by the appropriate scale factor to obtain the target wave number values (Fig. 18). Fine adjustment of the wave number of a component roll *after* the pattern has been imposed is possible by slightly shifting the edges of the imposed boundary that are parallel to the target rolls (Fig. 16(a)). (Recall that lasing is continued at the boundaries after it has been turned off in the interior 75% of the cell.) The other boundary edges are also moved slightly in the process to ensure uniform stretching of the component roll throughout the interior non-lased section.

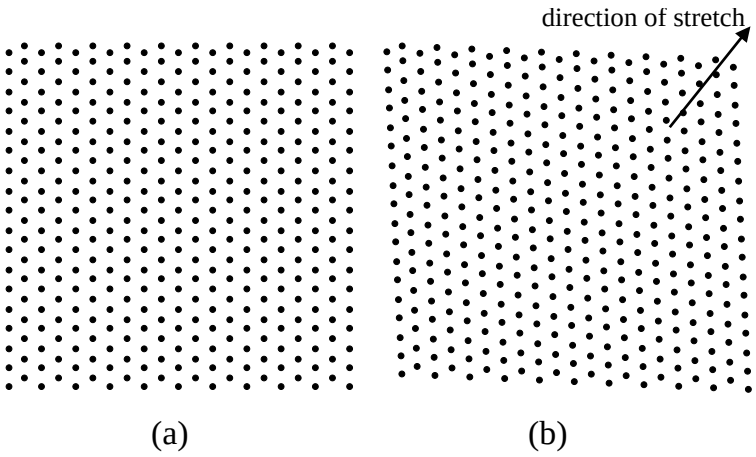

Figure 18: Hexagonal array of points (a) before and (b) after uniformly stretching by a factor of 0.9 in a fixed direction to adjust the wave number of the component rolls relative to one another.

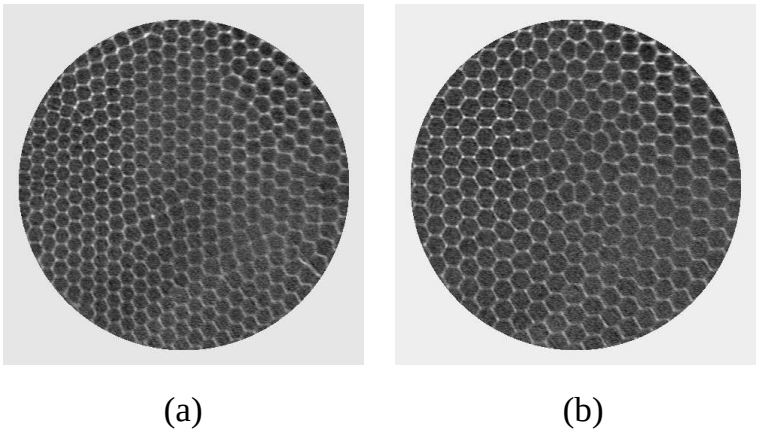

Figure 19: Hexagonal patterns that have become unstable as a result of being imposed with wave number outside the stable band. (a) Imposed q too high. b) Imposed q too low.

3.2.1.2 Measuring the Band

The width of the stable band at the Pr corresponding to the silicone oil used in the experiments is measured by imposing ideal hexagons at fixed ϵ and then tracking the evolution of the wave number $q_1 = q_2 = q_3 = q$. After the initial condition is set by the laser, images are taken at intervals of $\sim 7\tau_v$ for a duration of $\sim 400\tau_v$. A background image, taken at control parameter ϵ set below onset when no pattern has formed, is subtracted from each image to improve the signal-to-noise ratio. The images are then demodulated as described above to extract the three component rolls of the pattern and their wave number. The average of the measured q_j's is computed and is plotted against time. The procedure is repeated for a range of different initial q values at the same ϵ to produce a plot like that of Fig. 20. If the imposed q is within the stable band then the average of the three q_j does not change appreciably, and has been observed to persist for over $\sim 10^4\tau_v$. However for an imposed q that is too large or too small the pattern becomes unstable leading to the formation of defects at the boundary or within the bulk of the pattern (Fig. 19). The defects propagate through the pattern and significantly alter its average wave number, as is shown by the $\times$ symbols in Fig. 20. The largest and smallest q for which the wave number is stationary form the boundary of the band at that ϵ. The process is repeated for a range of ϵ values to form the stable band for the given Pr.

3.2.2 Secondary Instabilities

Busse *et al.* identified the mechanisms of secondary instability that restrict the region of stable straight convection rolls in RBC [8]. Unstable straight rolls were observed to transition to states with stable wave number through striking phase or amplitude instabilities, such as the zig-zag and cross-roll instabilities (Fig. 21).

The nature of secondary instability in more complex patterns such as triangles, squares and hexagons is not as well studied and understood. For hexagons there are some suggestions as to the nature of the instability mechanisms [13, 14] but no controlled experimental investigations have heretofore been conducted. Moreover, unlike in the case of straight rolls, the mechanisms are not easily distinguishable by eye, as Fig. 22 illustrates. Thus

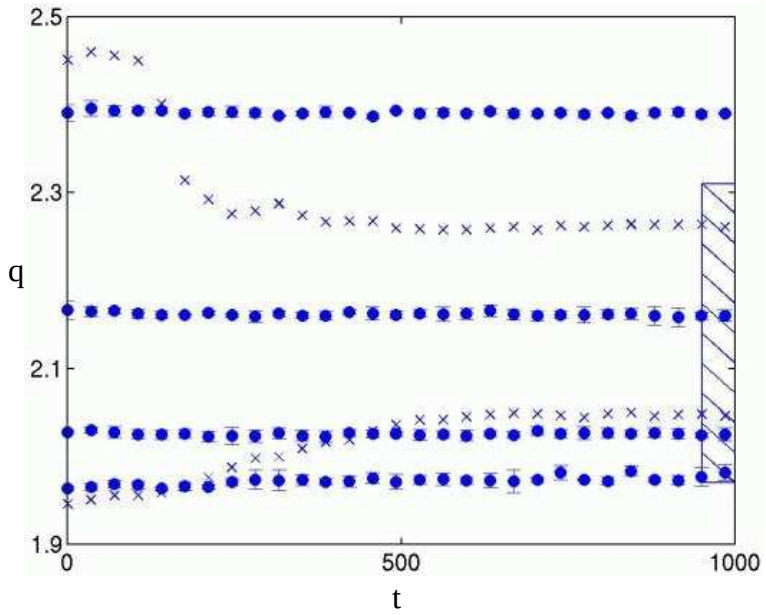

Figure 20: Time evolution of average wave number q of ideal hexagonal patterns illustrates stable vs unstable wave numbers for $\epsilon = 0.28$. Time is in units of τ_v. q represents the average of q_1, q_2, q_3; the variance of q is typically much smaller than the symbol size. Average wave numbers q that are time-independent correspond to stable ideal hexagonal planforms ($\bullet$). By contrast, time-dependent q correspond to patterns of initially ideal hexagons ($t = 0$) that lose stability ($\times$). The shaded area shows the extent of the stability region for ideal hexagons predicted by theory in [26] for the same ϵ.

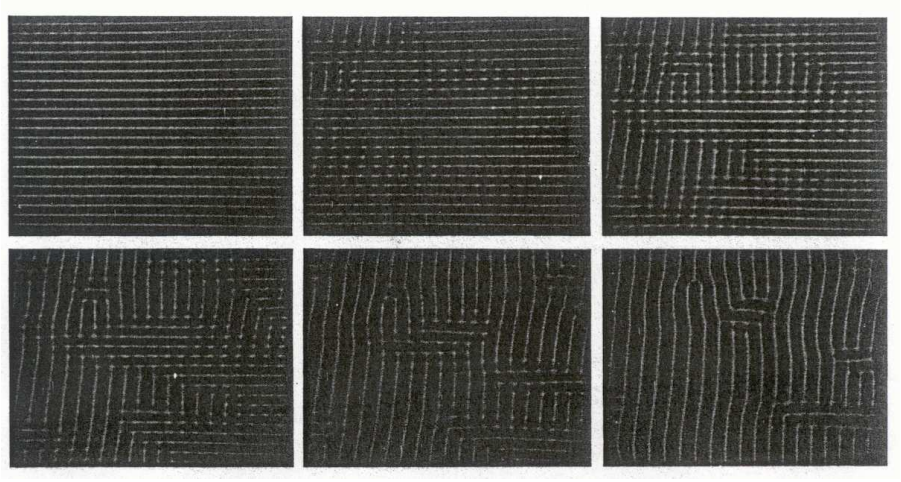

(a)

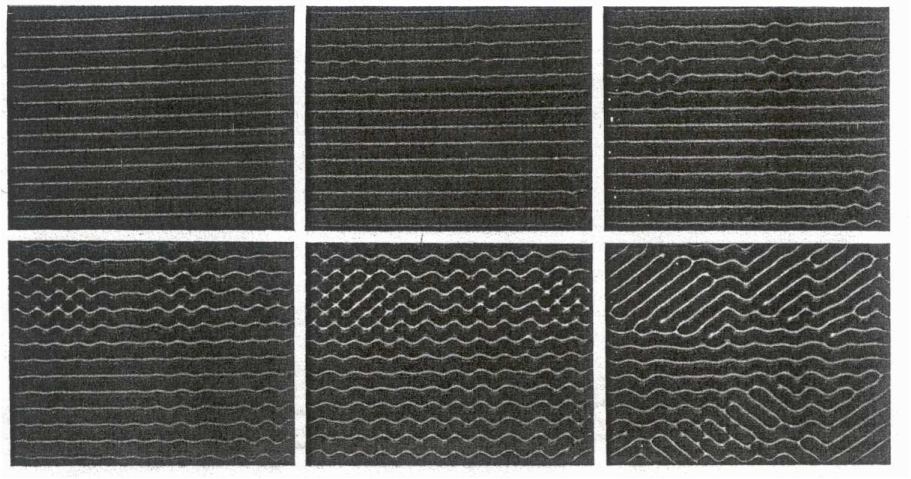

(b)

Figure 21: Secondary instability of straight roll patterns observed in RBC. (a) Cross roll instability – rolls with q that is too large decrease in amplitude and are replaced with rolls of smaller q oriented at 90° with respect to the original ones. (b) Zig-zag instability – Rolls with q too small form "zig-zags" which reduce the spacing between the rolls, effectively raising q. As the zig-zags increase in amplitude neighboring rolls join and form new rolls. (From Busse *et al.* [8].)

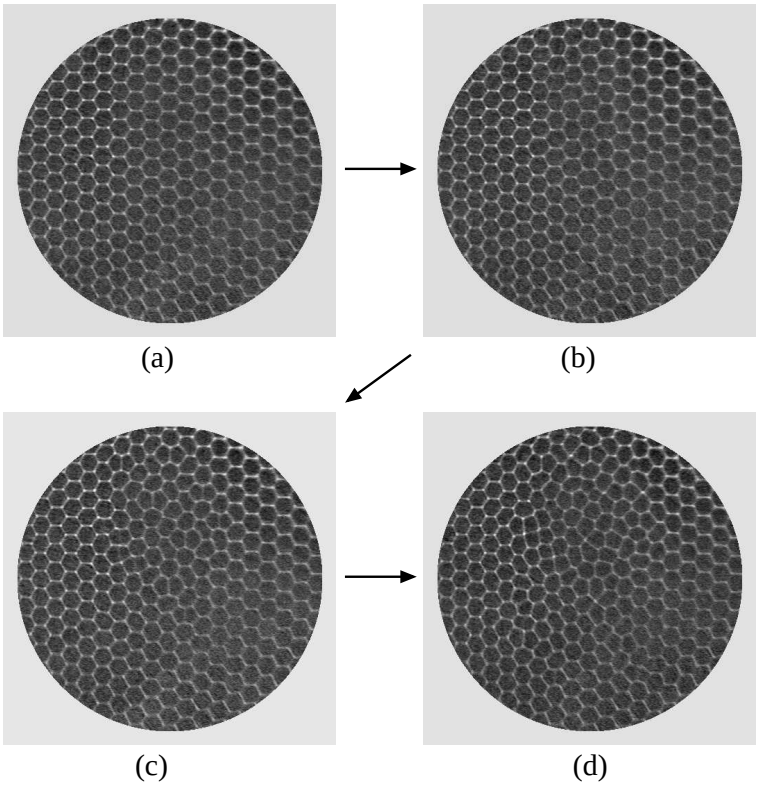

Figure 22: Evolution of a hexagonal pattern with q too small. The data is for $\epsilon = 2.01$ which corresponds to a measured low q boundary of $\epsilon = 2.04$. The images are taken $\sim 5\tau_v$ apart.

the approach of our investigations has been to impose predetermined perturbations as initial conditions and to then measure their stability. Bestehorn's analysis suggests that the instabilities in BM convection when surface tension is dominant are due solely to phase perturbations [26]. While their nature was not determined in that study, amplitude equation analyses suggest that the instabilities in hexagonal patterns correspond to two different types of long-wavelength modulations of the phase of the pattern [13, 14]. A review of the main ideas that lead to this conclusion are presented in Section 3.2.2.1 below. A more detailed derivation can be found in Refs. [13, 14, 15].

3.2.2.1 Phase Instabilities

The instabilities are determined by imposing amplitude and phase perturbations to the stable hexagon solutions $\sum_{j=1}^{3} A_j e^{iq_c \mathbf{n}_j \cdot \mathbf{r}} + \text{c.c.}$ of the amplitude equations (where q_c is the

critical wave number and $A_1 = A_2 = A_3 = H(\epsilon, \alpha, \gamma, q) \neq 0$)

$$\partial_t A_i = \epsilon A_i + (\hat{\mathbf{n}}_i \cdot \nabla)^2 A_i + \alpha A_j^* A_k^* - (|A_i|^2 + \gamma |A_j|^2 + \gamma |A_k|^2) A_i, \tag{14}$$

and then determining the unstable modes.

Perturbations of the form $A_j = He^{i\mathbf{Q}_j \cdot \mathbf{r}}(1 + a_j + i\phi_j)$ are substituted into the amplitude equations, where $\mathbf{Q}_j = \mathbf{q}_j - q_c \mathbf{n}_j$, and a_j and ϕ_j are the amplitude and the phase perturbations respectively. Linearizing the resulting equations yields six equations in the a_j and ϕ_j. For vanishing k, the wave number of the phase perturbations, the perturbations a_j in the amplitudes adiabatically follow the phase dynamics and are eliminated along with the total phase $\phi_1 + \phi_2 + \phi_3$. That leaves ϕ_2 and ϕ_3 which together can be used to express a phase vector $\mathbf{\Phi} = [-(\phi_2 + \phi_3), (\phi_2 - \phi_3)/\sqrt{3}]$. The equations can then be written as a linear diffusion equation of the phase of the hexagons:

$$\partial_t \mathbf{\Phi} = D_\perp \nabla^2 \mathbf{\Phi} + (D_\parallel - D_\perp) \nabla (\nabla \cdot \mathbf{\Phi}).$$

$D_\perp$ and $D_\parallel$ are functions of ϵ, α, γ and Q and are the transverse and longitudinal diffusion coefficients. They are analogous respectively to the velocity of transverse waves c_t and longitudinal waves c_l in the wave equation for an elastic solid. By that analogy the phase can be split into a transverse part $\mathbf{\Phi}_t$ that satisfies $\nabla \cdot \mathbf{\Phi}_t = 0$ and a longitudinal part that satisfies $\nabla \times \mathbf{\Phi}_l = \mathbf{0}$. It can be proved that

$$\partial_t \mathbf{\Phi}_t = D_\perp \nabla^2 \mathbf{\Phi}_t, \qquad \partial_t \mathbf{\Phi}_l = D_\parallel \nabla^2 \mathbf{\Phi}_l$$

Linear-stability analysis shows that the phase perturbations are stable if both $D_\perp > 0$ and $D_\parallel > 0$. Thus $D_\perp = 0$ determines the boundary of instability to transverse perturbations while $D_\parallel = 0$ determines the boundary of instability to longitudinal phase perturbations. Therefore long-wavelength transverse and longitudinal phase perturbations are the unstable phase modes for hexagonal patterns.

The phase perturbations are characterized by their wave vector $\mathbf{k}$ and its direction θ measured with respect to one of the wave vectors – in the experiments θ was measured with respect $\mathbf{q}_1$. For the longitudinal phase perturbation in the limit $k \to 0$, $\mathbf{\Phi}_l \parallel \mathbf{k}$, and for the transverse perturbation $\mathbf{\Phi}_t \perp \mathbf{k}$.

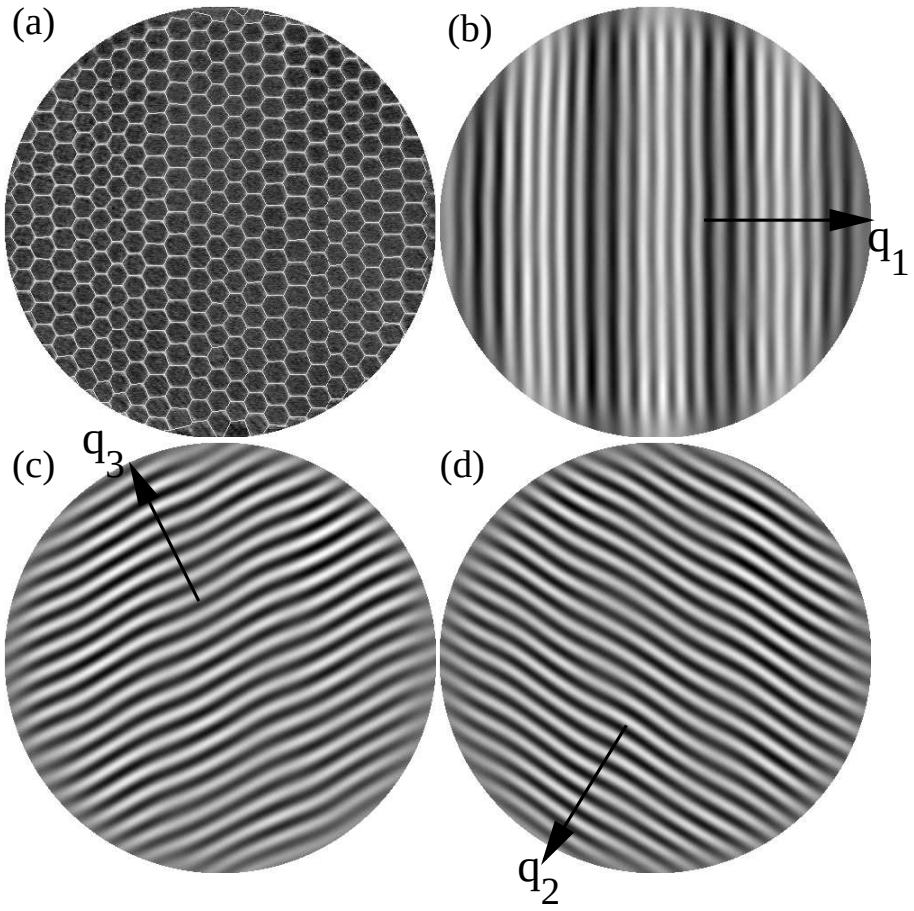

Figure 23: A shadowgraph image (a) of hexagons with a longitudinal phase perturbation is shown with the pattern's three roll components (b-d) extracted by complex demodulation. For the purposes of illustration, the perturbation, imposed as an initial condition, is shown with an amplitude that is larger than typical modulations by a factor of 8. In (a), the white edges and dark centers of the hexagons indicate, respectively, regions of down-flow and up-flow. (b) The main modulation is to the $\mathbf{q_1}$ rolls – note their compression and dilation. Shading has been added to emphasize the long-wave nature of the modulation – the overall lighter areas have higher wave number than the darker regions. (c) $\mathbf{q_2}$ rolls are sheared slightly by the modulation.(d) The $\mathbf{q_3}$ rolls are modulated with the same amplitude and phase as the $\mathbf{q_2}$ rolls.

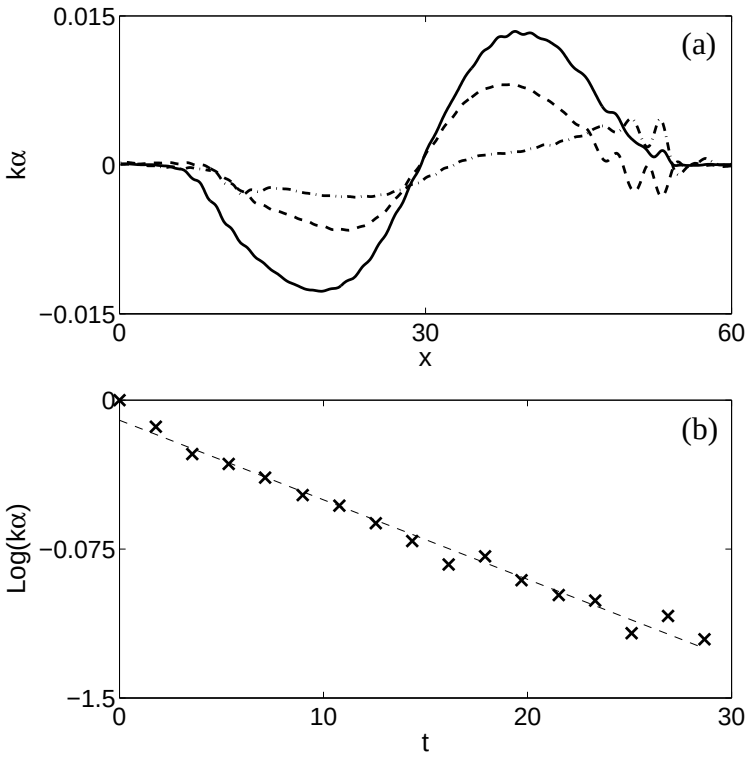

Figure 24: Spatial and temporal evolution of the longitudinal phase perturbation. (a) The profile of the local wave number of the $\mathbf{q}_1$ rolls (scaled by the mean value $q = 2.08$) is plotted at times $t = 0$ (symbol $-$), $t = 13$ ($--$) and $t = 27$ ($\cdot-$); thus the phase modulation adjusts the overall wave number by a maximum of less than 1.5%. The long-wave nature of the perturbation is apparent – the modulation wave number $k = 0.14$ is approximately $1/15^{\text{th}}$ of the mean q. (b) The amplitude ($k\alpha$) is plotted as a function of time on a semi-log scale; the slope of this curve yields the growth rate, which is negative for perturbations within the stable band.

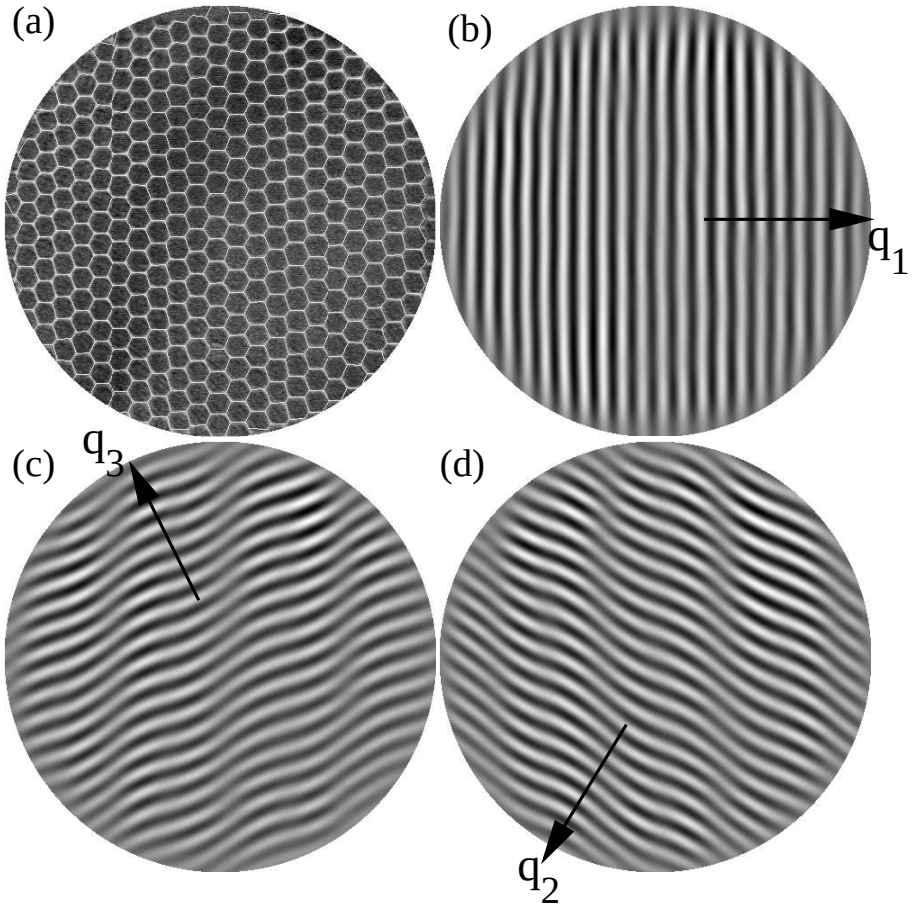

Figure 25: A shadowgraph image (a) of hexagons with a transverse phase perturbation is shown with the pattern's three roll components (b-d) extracted by complex demodulation. For the purposes of illustration, the perturbation is shown with an amplitude that is larger than typical modulations by a factor of 9. (b) The $\mathbf{q}_1$ component is unaffected by the transverse modulation. (c) The roll component labeled by wave vector $\mathbf{q}_2$ that shows the shearing of the rolls in a direction transverse to the $\mathbf{q}_1$ rolls. (d) The $\mathbf{q}_3$ component is modulated with the same amplitude but opposite phase as the $\mathbf{q}_2$ component.

To study the dynamics of longitudinal and transverse phase perturbations experimentally, perturbations suggested by Young and Riecke [40] were imposed. Taking $\theta = 0$, the phase perturbations applied to the $\mathbf{q}_1$, $\mathbf{q}_2$ and $\mathbf{q}_3$ component roll patterns are respectively $\phi_1 = i\alpha \cos kx$, $\phi_2 = -i\frac{1}{2}\alpha \cos kx$ and $\phi_3 = -i\frac{1}{2}\alpha \cos kx$ for the longitudinal perturbation, where x is parallel to $\mathbf{q}_1$ (Fig. 23). The perturbation appears as a sinusoidal modulation, with amplitude $k\alpha$, of the wave number of the $\mathbf{q}_1$ rolls parallel to $\mathbf{k}$ (Fig. 24(a)). The $\mathbf{q}_2$ and $\mathbf{q}_3$ rolls also have wave-number modulations parallel to $\mathbf{k}$ but with half the amplitude. For a transverse perturbation at $\theta = 0$, the ϕ_j are $\phi_1 = 0$, $\phi_2 = i\frac{\sqrt{3}}{2}\alpha \cos kx$ and $\phi_3 = -i\frac{\sqrt{3}}{2}\alpha \cos kx$. The result is a sinusoidal modulation of the $\mathbf{q}_2$ and $\mathbf{q}_3$ rolls parallel to $\mathbf{k}$ with amplitude $\frac{\sqrt{3}}{2}k\alpha$, but no perturbation of the $\mathbf{q}_1$ rolls (Fig. 25).

The longitudinal phase perturbations for arbitrary angle θ are given by

$$\begin{aligned}
\phi_1 &= i\alpha \cos\theta \cos[k(x\cos\theta + y\sin\theta)], \\
\phi_2 &= -i\frac{1}{2}\alpha(\cos\theta - \sqrt{3}\sin\theta)(\cos[k(x\cos\theta + y\sin\theta)], \\
\phi_3 &= -i\frac{1}{2}\alpha(\cos\theta + \sqrt{3}\sin\theta)\cos[k(x\cos\theta + y\sin\theta)];
\end{aligned}$$

and the transverse phase perturbations are:

$$\begin{aligned}
\phi_1 &= -i\alpha \sin\theta \cos[k(x\cos\theta + y\sin\theta)], \\
\phi_2 &= i\frac{1}{2}\alpha(\sin\theta + \sqrt{3}\cos\theta)(\cos[k(x\cos\theta + y\sin\theta)], \\
\phi_3 &= i\frac{1}{2}\alpha(\sin\theta - \sqrt{3}\cos\theta)\cos[k(x\cos\theta + y\sin\theta)].
\end{aligned}$$

To investigate the mechanisms of secondary instability, the longitudinal and transverse phase perturbations are applied at fixed ϵ to the hexagonal patterns and their growth rates are measured. The perturbations decay exponentially within the stable band at rates that depend on q. The perturbation growth rates are measured by tracking the amplitude of the sinusoidally modulated wave number of one of the component rolls − the other modulated rolls are found to decay at approximately the same rate. A plot of the logarithm-of-the-amplitude versus time fits reasonably well to a straight line (Fig. 24(b)) as expected for small disturbances. The slope of the line yields the growth rate. The procedure is repeated for q values that span the stable band.

The growth rate, *i.e.*, the slope of the logarithm-of-the-amplitude versus time graph is obtained using linear regression analysis, discussed in Appendix B and Ref. [24], and its error is estimated from the standard error of the slope.

3.2.3 Penta-Hepta Defects

Point defects in roll patterns appear as dislocations and play a role in pattern selection [7]. For an isolated dislocation in a pattern of straight rolls, such as in Fig. 26 for RBC, there is a wave number q_u above the dislocation that is different from q_l below the dislocation – in Fig. 26 $q_l > q_u$ as there is an "extra" roll below the dislocation. The defect "climbs" upward if q_l is the preferred wave number and downward if q_u is preferred. If the defect does not move then the preferred wave number is $q_l < q_d < q_u$ and is referred to as the "optimal" wave number. Asymptotically far from the defect $q_l = q_d = q_u$. Motion normal to the rolls is called "glide" and does not change the overall wave number of the pattern. The speed of the defect depends on $q - q_d$.

In hexagonal patterns the most common point defect is a PHD, which is a five-sided cell next to a seven-sided cell (Fig. 27(a)) embedded in a pattern of hexagons. It can be considered as a state of two bound dislocations of opposite phase-winding number in two of the three component rolls that make up the pattern [36]; *i.e.*, for any counterclockwise path encircling the defect core there is a phase jump of -2π for one of the rolls with a dislocation (Fig. 27(b)) and 2π for the other (Fig. 27(c)). Detailed theoretical and numerical studies amplitude equation studies by Tsimring [15] of the speed and direction of motion of a single PHD suggest that PHDs play the role of wave number selection mechanisms in hexagonal patterns. Corresponding detailed experimental study of PHD motion has not been performed. Work on PHDs done by Ciliberto *et al.* [23] involved inducing a pair of PHDs by focusing light from a powerful lamp onto a single location of a RBC cell and studying their characteristics. However, the technique does not enable control of the background wave number of the pattern which strongly influences PHD motion [15].

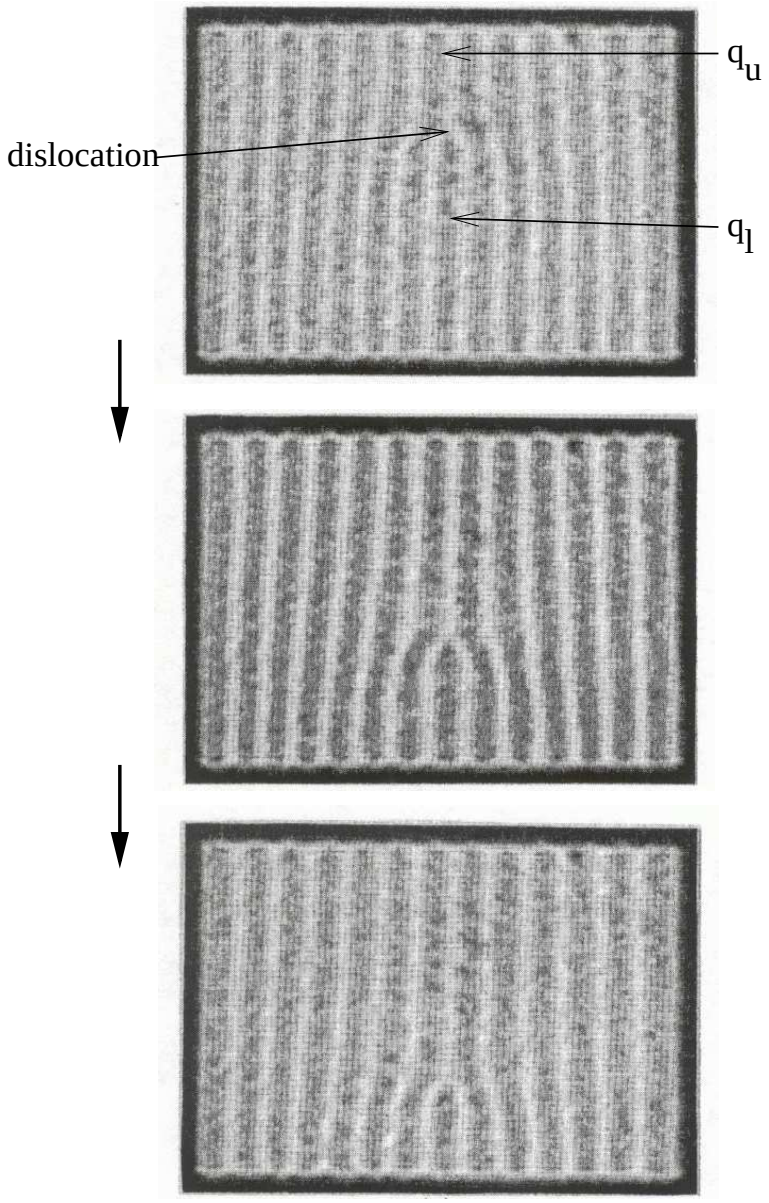

Figure 26: Climb motion of a single dislocation in a roll pattern in RBC. The wave number above the defect q_u is "preferred" over that below the defect q_l hence motion downward. (Adapted from Cross and Hohenberg [7].)

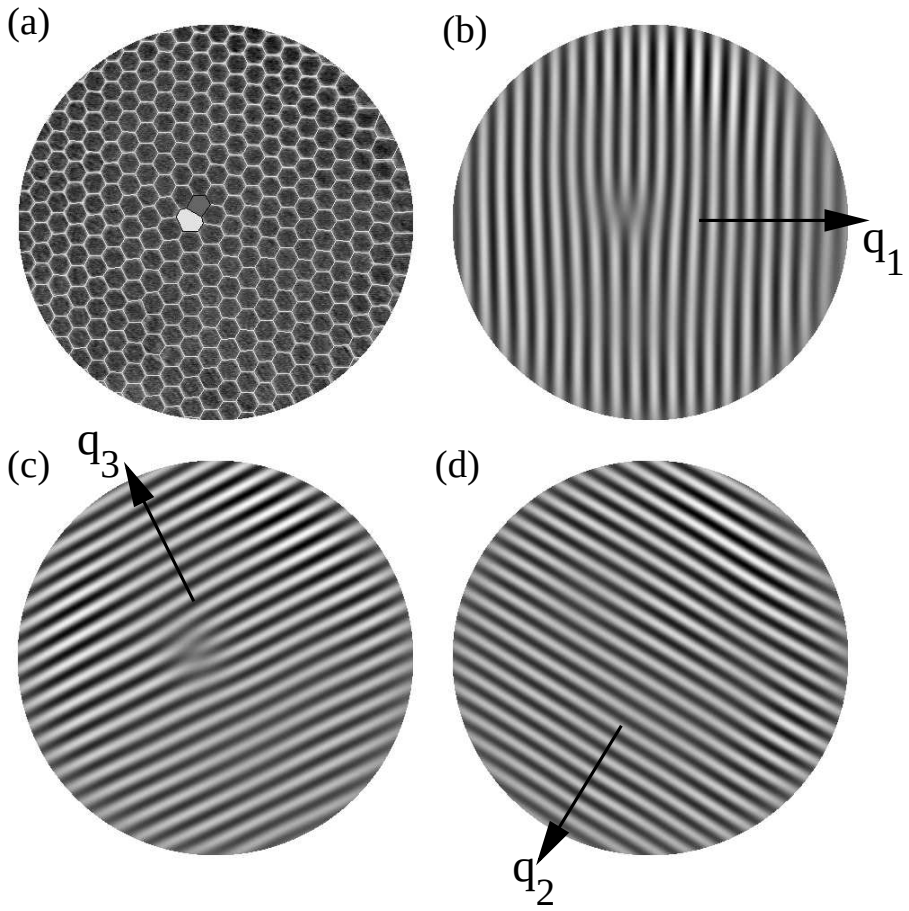

Figure 27: Decomposition of an imposed hexagonal pattern with a PHD embedded near its center. (a) The five-sided cell of the PHD has dark shading and the seven-sided cell has light shading. The $\mathbf{q_1}$ (a) and $\mathbf{q_3}$ (c) rolls have dislocations while the $\mathbf{q_2}$ rolls(d) are dislocation-free. The dislocations have opposite winding phase numbers. In this case any counter-clockwise close path encircling the defect has a jump of -2π for $\mathbf{q_1}$ and $+2\pi$ for $\mathbf{q_3}$.

3.2.3.1 Theoretical Analysis

This section is an overview of a detailed analysis of PHD motion presented in [15]. It begins by considering a stationary PHD and then proceeds to outline the method used to determine the speed and direction of motion of an isolated PHD.

A hexagonal pattern can be written as $\sum_{j=1}^{3} B_j e^{i(q_c \mathbf{n}_j + \mathbf{Q}_j)\cdot \mathbf{r}} + \text{c.c.}$, where q_c is the "optimal" wave number, which is at the center of the stable band; $\mathbf{Q}_j$ are "corrections" to the optimal wave vectors, and satisfy the resonance condition $\sum_{j=1}^{3} \mathbf{Q}_j = 0$; and $\mathbf{n}_1 = (1, 0)$, $\mathbf{n}_2 = (-\frac{1}{2}, \frac{\sqrt{3}}{2})$ and $\mathbf{n}_3 = (-\frac{1}{2}, -\frac{\sqrt{3}}{2})$. The B_j are functions of the rescaled variables $\mathbf{R} = \epsilon^{1/2}\mathbf{r}$, and satisfy the following three equations, which are derived directly from Eqs. (2)

$$\partial_T B_i = (\mu - Q_i^2)B_i + (\hat{\mathbf{n}}_i \cdot \nabla)^2 B_i + 2iQ_i(\hat{\mathbf{n}}_i \cdot \nabla)B_i + B_j^* B_k{}^* - (|B_i|^2 + \gamma|B_j|^2 + \gamma|B_k|^2)B_i, \quad (15)$$

with $\{i, j, k\} = \{1, 2, 3\}$, $\{2, 3, 1\}$, $\{3, 1, 2\}$. The spatial gradients are calculated with respect to $\mathbf{R}$.

For the special case when all $Q_j = Q$, the B_j can be expressed analytically as

$$B_j^0 = B_0 \equiv \frac{1 + \sqrt{1 + 4(\mu - Q^2)(1 + 2\gamma)}}{2(1 + 2\gamma)}.$$

A hexagonal pattern of infinite spatial extent with a single PHD is still largely hexagonal and can also be represented by $\sum_{j=1}^{3} B_j e^{i(q_c \mathbf{n}_j + \mathbf{Q}_j)\cdot \mathbf{r}} + \text{c.c.}$ In that case all the information about the defect is contained in the slowly varying amplitudes $B_j(x, y)$.

When $Q_j = 0$ the PHD is found to be stationary. Without loss of generality the PHD can be chosen such that the phase winding number around its core for the rolls corresponding to $\mathbf{q}_2$ is 2π, and is -2π for the $\mathbf{q}_3$ rolls, and 0 for the $\mathbf{q}_1$ rolls. Then a PHD solution to Eq. 15 can be written as

$$B_j = F_j(R, \phi)e^{i\theta_j(R,\phi)}, \quad (16)$$

where R and ϕ are polar coordinates. The condition of phase-winding number equal to 0 for the $\mathbf{q}_1$ rolls means $\oint_C \nabla\theta_1 d\mathbf{s} = 0$. Similarly for the $\mathbf{q}_2$ rolls, $\oint_C \nabla\theta_2 d\mathbf{s} = 2\pi$, and $\oint_C \nabla\theta_3 d\mathbf{s} = -2\pi$ for the $\mathbf{q}_3$ rolls. $F_2(0, \phi) = 0$ and $F_3(0, \phi) = 0$, while $F_j(\infty, \phi) = B_0$, for all j. This solution cannot be expressed in a closed analytical form. However, in the far field

where the B_j approach B_0, the following solutions for the phases θ_j have been proposed [35]

$$\theta_1 = (1-\cos 2\phi)\frac{\sqrt{3}}{6}, \tag{17}$$

$$\theta_2 = \phi - \left[\frac{1}{2} - \cos\left(2\phi - \frac{2\pi}{3}\right)\right]\frac{\sqrt{3}}{6}, \tag{18}$$

$$\theta_3 = -\phi - \left[\frac{1}{2} + \cos\left(2\phi - \frac{2\pi}{3}\right)\right]\frac{\sqrt{3}}{6}, \tag{19}$$

For the case when $Q_j \neq 0$, the PHD is not stationary. Tsimring's analysis then assumes as an ansatz that the PHD moves with a constant velocity $\mathbf{V}$. Then a coordinate transformation $\mathbf{R}' = \mathbf{R} - \mathbf{V}T$ into the moving frame yields the following from Eqs. (15)

$$-\mathbf{V}\cdot\nabla B_i = (\epsilon - Q_i^2)B_i + (\hat{\mathbf{n}}_i\cdot\nabla)^2 B_i + 2iQ_i(\hat{\mathbf{n}}_i\cdot\nabla)B_i + B_j^* B_k^* - (|B_i|^2 + \gamma|B_j|^2 + \gamma|B_k|^2)B_i, \tag{20}$$

A transformation of Eqs. (20) into the (ξ,η) coordinate frame is performed, where $\xi = X\cos\psi + Y\sin\psi$ and $\eta = Y\sin\psi - X\cos\psi$ are respectively the coordinates along the direction of PHD motion and orthogonal to it. Variable ψ is the angle between the direction of PHD motion and the X-axis. The resulting equations are then projected onto the translation modes $\{\partial_\xi B_j^*\}$ and $\{\partial_\eta B_j^*\}$, yielding

$$I_{\eta\eta}V_\eta + I_{\eta\xi}V_\xi = -i\left\langle \sum_{j=1}^{3} Q_j \partial_\eta B_j^* (\hat{\mathbf{n}}_j\cdot\nabla)B_j - \text{c.c.}\right\rangle,$$

$$I_{\eta\xi}V_\eta + I_{\xi\xi}V_\xi = -i\left\langle \sum_{j=1}^{3} Q_j \partial_\xi B_j^* (\hat{\mathbf{n}}_j\cdot\nabla)B_j - \text{c.c.}\right\rangle,$$

where

$$I_{\xi\xi} = \left\langle \sum_{j=1}^{3} |\partial_\xi B_j|^2 \right\rangle,$$

$$I_{\eta\eta} = \left\langle \sum_{j=1}^{3} |\partial_\eta B_j|^2 \right\rangle,$$

$$I_{\xi\eta} = I_{\eta\xi} = \frac{1}{2}\left\langle \sum_{j=1}^{3} \partial_\xi B_j \partial_\eta B_j^* + \text{c.c.}\right\rangle,$$

$\langle \ldots \rangle = \iint \ldots dXdY$ and $\langle \partial_X B_j \partial_Y B_j^* \rangle - c.c = i\delta_j |B_j^0|^2$. The phase-winding number is represented by δ_j, thus $\delta_1 = 0$, $\delta_2 = 2\pi$ and $\delta_3 = -2\pi$. All other terms on the right-hand

side of Eq. 20 vanish on integration. The remaining equations can be written as

$$\hat{\mathbf{I}} \cdot \mathbf{V} = \begin{pmatrix} I_{\xi\xi} & I_{\xi\eta} \\ I_{\eta\xi} & I_{\eta\eta} \end{pmatrix} \begin{pmatrix} V \\ 0 \end{pmatrix} = \begin{pmatrix} \overline{T}_1 \\ \overline{T}_2 \end{pmatrix}, \tag{21}$$

where

$$\begin{aligned} \overline{T}_1 &= 2\pi[|B_2^0|^2 Q_2 \sin(\psi - \frac{2}{3}\pi) - |B_3^0|^2 Q_3 \sin(\psi + \frac{2}{3}\pi)], \\ \overline{T}_2 &= 2\pi[|B_2^0|^2 Q_2 \cos(\psi - \frac{2}{3}\pi) - |B_3^0|^2 Q_3 \cos(\psi + \frac{2}{3}\pi)], \end{aligned}$$

and $\hat{\mathbf{I}}$ is called the mobility tensor of the PHD.

The angle and speed of the PHD motion are determined through lengthy calculations of the components of the mobility tensor. The region of integration of the components is split into two parts: an inner region that uses the stationary PHD solution, Eq. (16), and an outer region that uses the phase approximation, Eqs. (17)-(19). The results are the following nonlinear algebraic equations that relate V, ψ, Q_2, and Q_3

$$\frac{5}{2} V \ln(w_1 V) + V \ln(w_2 V) \cos 2\psi = 2Q_2 \sin(-\psi + 2\pi/3) + 2Q_3 \sin(\psi + 2\pi/3), \tag{22}$$

$$V \ln(w_3 V) \sin 2\psi = 2Q_2 \cos(-\psi + 2\pi/3) - 2Q_3 \cos(\psi + 2\pi/3), \tag{23}$$

3.2.3.2 Experiments

PHDs are studied experimentally in this investigation by imposing a single PHD in a pattern of hexagons with a range of different wave numbers for each of the component roll patterns. The speed and direction are then measured and plotted as a function of wave number.

A template of the coordinates of the pattern containing a single PHD is created from the following equations for the phases and amplitudes of the component rolls [36]:

$$\begin{aligned} A_1 &= A_1^0 \tanh\{0.2[(X_1 - X_1^0)^2 + (Y_1 - Y_1^0)^2]^{1/2}\} \\ \phi_1 &= \arctan[(Y_1 - Y_1^0)/(X_1 - X_1^0)] + \phi_0 \\ A_2 &= A_2^0, \qquad \phi_2 = 0 \\ A_3 &= A_3^0 \tanh\{0.2[(X_3 - X_3^0)^2 + (Y_3 - Y_3^0)^2]^{1/2}\} \\ \phi_3 &= -\arctan[(Y_3 - Y_3^0)/(X_3 - X_3^0)], \end{aligned}$$

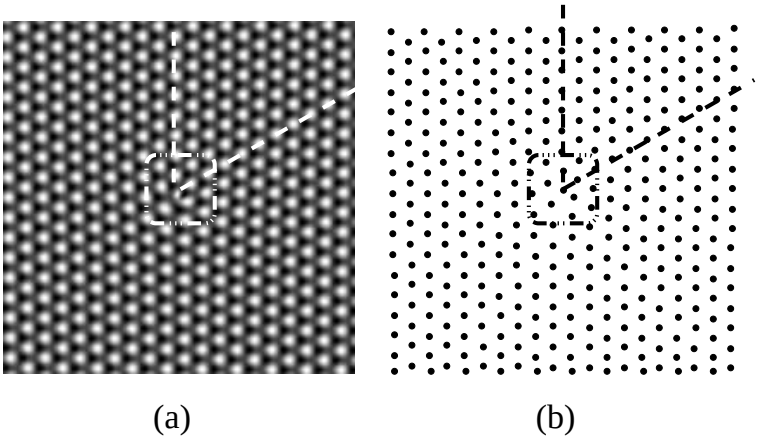

Figure 28: Illustration of grid of points obtained from a hexagonal pattern containing a single PHD is obtained. (a) Numerically obtained gray scale image with a PHD in the center. (b) Grid of points to be used for imposing the pattern onto the BM convection cell obtained by the finding the centroids of the peaks in (a). The dashed lines indicate rows of extra cells or points. The boxes are centered around the defect core.

where $({X_1}^0, {Y_1}^0)$ and $({X_3}^0, {Y_3}^0)$ are the coordinates of the cores of the dislocations, $A_j^0 = 0.01$ and $\phi_0 = \pi/4$. As in the case of an ideal hexagonal pattern the A_j are superposed and an array of points containing a PHD is obtained by finding the coordinates of the centroid of each peak in the gray-scale pattern as in Fig. 28.

The pattern with a PHD is imposed for different q_j and the direction of motion as well as the average speed is measured. For each roll pattern the q_j for which the PHD is stationary is noted – this is the so-called optimal wave number for the roll pattern and is in the center of the stable band.

3.2.3.3 Image Analysis

Measurement of q for the roll components of a pattern with a PHD differs from the method used above for an ideal pattern. In that case q for each component roll pattern is obtained by computing the distance from the origin of the peaks in the power spectrum of the Fourier transform. That method is inaccurate when applied to a pattern with a PHD because the wave number of the component roll patterns with dislocations is nonuniform near the PHD core (Fig. 29(c)). For an ideal PHD each q_j becomes uniform asymptotically far from the core of the PHD. A satisfactory approximation of that value is the average of the local

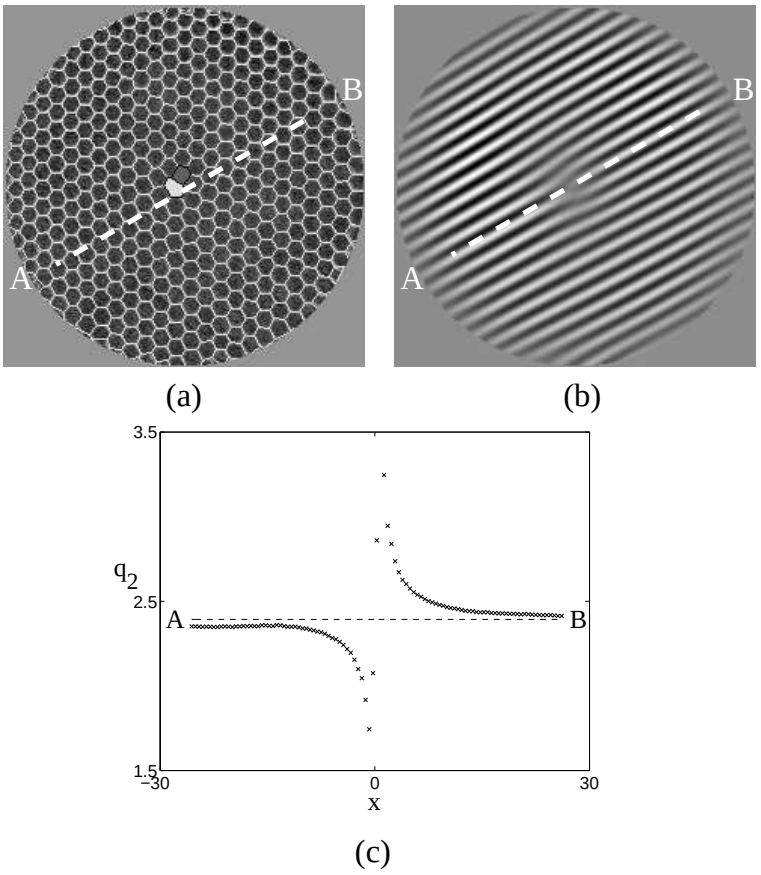

Figure 29: Local wave number of the $\mathbf{q}_3$ roll pattern along a line through a single penta-hepta defect. (a) Shadowgraph image of PHD taken with $\epsilon = 3.8$. The dark colored patch is the five sided cell and the light patch is the seven sided cell. (b) The corresponding $\mathbf{q}_3$ roll pattern. (c) Cross-section of the local wave number of the mode along the dashed line indicated in (a) and (b). The wave number from the core to "A" is lower than the wave number from the core to "B" because it has one less row. In the ideal case the lower (high) wave number increases (decreases) asymptotically to a value which defines the wave number of the rolls. The wave number is well approximated by taking the average of the two over a range of several wavelengths away from the defect core. In this case the average wave number is $q_3 = 2.39$.

q measured from either side of the PHD along a line that is perpendicular to the wave vector of the rolls and that passes through the core. The local wave number measurements are taken starting several wavelengths away from the core to avoid the region where q changes significantly over a few wavelengths. Matlab code that performs local wave number measurements of striped patterns was written by Chiam and Paul [33] and is based on an algorithm developed by Egolf *et al.* [34].

The position of the PHD is tracked by locating the singularity in the phase in either one of the roll patterns with a dislocation [23]. Finding the singularity involves first demodulating the image of the pattern to obtain the complex amplitude of one of the component rolls with a dislocation and then computing its phase. As mentioned above a pattern with a large number of hexagons containing only a single PHD is otherwise a regular hexagonal pattern. Thus the gray-scale camera image can still be represented as in Eq. (13), where the details of the PHD are contained in the $A_j(x, y)$. To extract $A_1(x, y)$ from the peak that corresponds to $A_1(x, y) \exp(i\mathbf{q}_1 \cdot \mathbf{x})$ in the power spectrum $|F|^2$, $F(q_x, q_y)$ is shifted by $-\mathbf{q}_1$ to locate peak 1 at the origin in Fourier space. The shifted $F(q_x, q_y)$ is then multiplied by a low pass filter with a cutoff in the range of the peak width and an inverse Fourier transform is performed to obtain the complex amplitude $A_1(x, y)$. The phase is then straightforwardly obtained from $\arctan(\mathrm{Im}[A_1(x, y)]/\mathrm{Re}[A_1(x, y)])$ and typically looks like Fig. 30. The singularity in the phase appears as a sharp peak in a spatial derivative of the phase – Fig. 29 shows the peak that results from the gradient of the phase, *i.e.* the wave number.

Analysis of the defect position shows that the two dislocations associated with the PHD are slightly offset from one another. Thus, to track the PHD the same dislocation must be used. Use of the other dislocation yields similar results.

The average direction and speed of the PHD for a typical experimental run are measured from the set of coordinates of the PHD's position generated from the time series of images taken during the experiment. Linear regression [24] is used to compute the straight line $y = a + bx$ that points in the average direction of motion. An error estimate of the direction measurement is computed from the standard error in the estimate of the slope b. The average speed is computed from the slope of the distance versus time graph, and its error

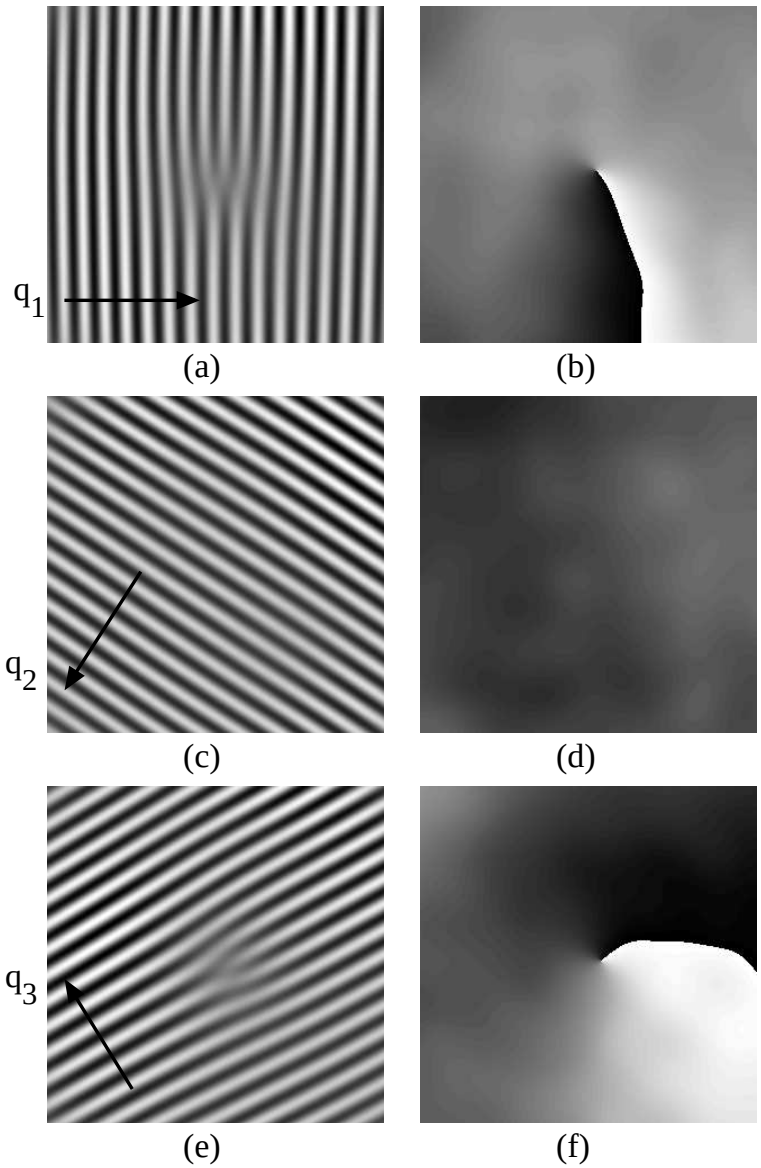

Figure 30: Illustration of the phases (b), (d), (f) of the slowly varying amplitudes of the components roll patterns (a), (c), (e) of a single PHD.

is also estimated from the standard error of the slope. Appendix B gives an outline of the linear regression analysis used.

CHAPTER IV

RESULTS AND CONCLUSIONS

4.1 Stable Band

The experimentally measured stable band for hexagons in Bénard-Marangoni convection (BMC) is plotted in Fig. 31 along with the theoretical prediction by Bestehorn [26] for comparison. There is quantitative agreement with theory for $\epsilon < 0.5$ at the low-q boundary. At the high-q boundary the agreement is qualitative – there is a clear shift both experimentally and theoretically of the boundary toward higher q as ϵ is increased. For larger ϵ however, the agreement is worse – the size of the band is well estimated but the predicted shift of the band to higher q with ϵ is not observed. There are several factors that may account for the differences between theory and experiment. Buoyancy effects are significantly larger in the theoretical analysis where $\Gamma = M/R \approx 2.7$, compared with $\Gamma \approx 8.5$ in the experiment. The Prandtl number Pr in the theoretical model is assumed to be infinite while the silicone oil used here has $Pr \approx 100$. Of smaller impact may be the differences in Biot number. At the aluminum-silicone oil boundary $Bi \approx 10^3$ compared with the theoretically assumed $Bi \to \infty$; and $Bi \approx 0.2$ in the experiment at the silicone-oil-air interface compared with $Bi = 0.1$ for the theoretical model. (Busse *et al.* attributed shifts in their measured boundary from the theoretical predictions in Rayleigh-Bénard convection (RBC) to finite conductivity effects [8].) The finite time over which the pattern was monitored for stability may have resulted in an overestimation of the width of the stable band. Near the outside edge of the boundary the growth rate of perturbations is small, thus the time scale over which the pattern breaks down is large. Typical observation times were $\sim 10^3 \tau_v$ but only $\sim 10^2$ horizontal diffusion times, which may be insufficient time for perturbations of long wavelength to grow.

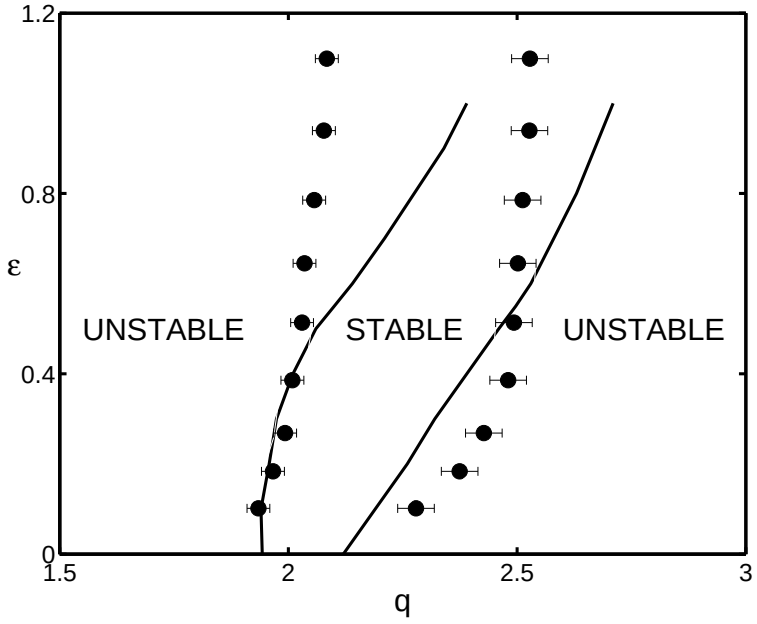

Figure 31: The band of stable wave numbers q for ideal hexagonal patterns ($q_1 = q_2 = q_3 = q$) is shown for a range of reduced temperatures ϵ. The experimentally determined stable wave numbers lie between the low- and high-q boundaries (•) and are compared with the theoretical predictions (solid lines) of Bestehorn [26].

4.1.1 Remarks

Amplitude equation analyses by Echabarria and Pérez-Garciá [13], and Young and Riecke [14] are carried out with the assumption of a pattern of infinite lateral extent. Their results predict a larger region of stability at small values of the control parameter ϵ. This is expected, as the range of stable solutions is reduced by the presence of boundaries – an effect shown theoretically [7] for straight rolls in Rayleigh-Bénard convection, where the stability band reduces in width from $\sim\epsilon^{1/2}$ to $\sim\epsilon$.

The failure of an earlier study by Cerisier *et al.* to observe stationary behavior for patterns of *any* q underscores the importance of mitigating the effects of the lateral boundary. In our early investigations it was noted that with an aluminum sidewall the pattern does not settle down even after waiting $\sim 10^4 \tau_v$. The pattern becomes stationary when the sidewall is replaced with one made of Teflon which is more closely matched in conductivity to the silicone oil. However, this is preceded by a period of $\sim 10^2 \tau_v$ during which additional hexagons form at the boundary for patterns with small q or disappear at the boundary for

patterns with large q. Thus the resulting measured stable band is smaller than predictions. A satisfactory solution is to continue to lase a "boundary" of several cells thick in the outer 75% of the convection cell after imposing the initial condition. The effect is to pin those cells thereby virtually eliminating the problem of large scale cell creation and destruction at the boundary. However, when the pattern does go unstable the breakdown occurs mostly at or near the pinned boundary. Nevertheless the resulting measured stability region shown in Fig. 31 is close in size to the theoretical prediction of Bestehorn.

The measured stable region in Fig. 31 represents a slice of the full region of stability for hexagons, which is expected to also depend on Pr as in the case of RBC (Fig. 32). As in RBC there is an upper limit in ϵ of the stability region for hexagons, *i.e.*, the slice of Fig. 31 has an upper bound. In experiments described in Ref. [37], hexagons lose stability to squares at $\epsilon \sim 2.4$.

4.2 Secondary Instability

Secondary instabilities are identified by observing the behavior of their growth rates at the boundaries of the stable band. The growth rate of the transverse perturbation is found to remain relatively constant and negative for $2.2 \lesssim q \lesssim 2.55$, but starts to gradually decrease in magnitude for $q \lesssim 2.2$, and appears to tend to zero at the low-wave-number boundary (Fig. 33). This suggests that the divergence-free transverse perturbation becomes unstable at the low wave number side of the stable band and is thus responsible for the instability at that boundary. At the high wave number boundary the magnitude of the growth rate is not reduced, *i.e.*, the transverse modulation does not appear to restrict the band at high wave number. For the longitudinal-phase perturbation, the measured growth rate is finite at the low-wave-number boundary and remains constant for $2.05 \lesssim q \lesssim 2.4$. As q approaches the high-wave-number boundary, the change in growth rate is not slow as in the transverse case, but becomes increasingly sharp the closer q gets to the boundary, and appears to tend to zero growth rate at the boundary (Fig. 34), *i.e.*, the longitudinal perturbation may be the secondary instability that restricts the stable band at high wave number.

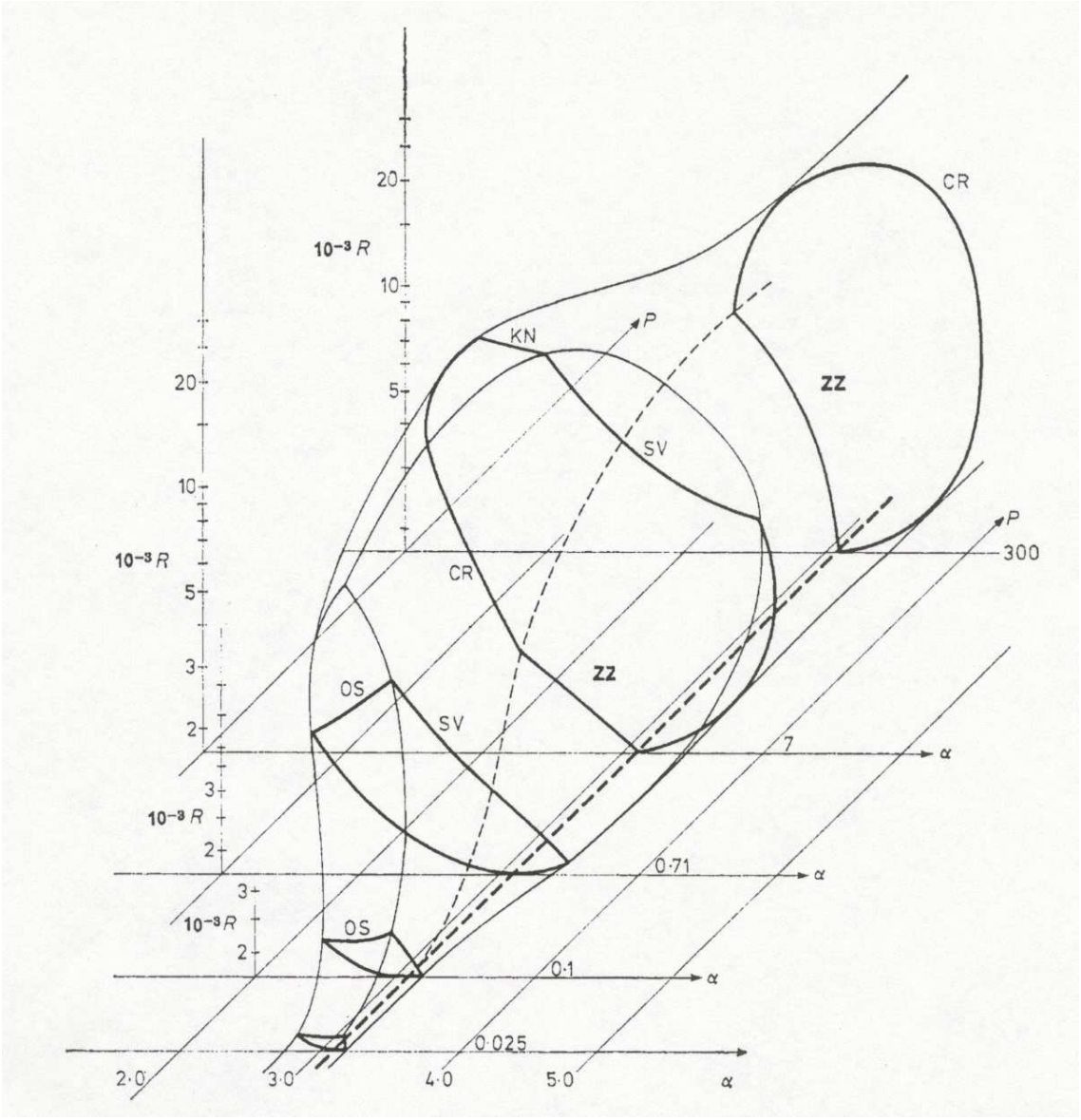

Figure 32: The Busse balloon – a three-dimensional region of stable straight convection rolls in R-P-α (Rayleigh number-Prandtl number-wave number) space. (From Busse [22].)

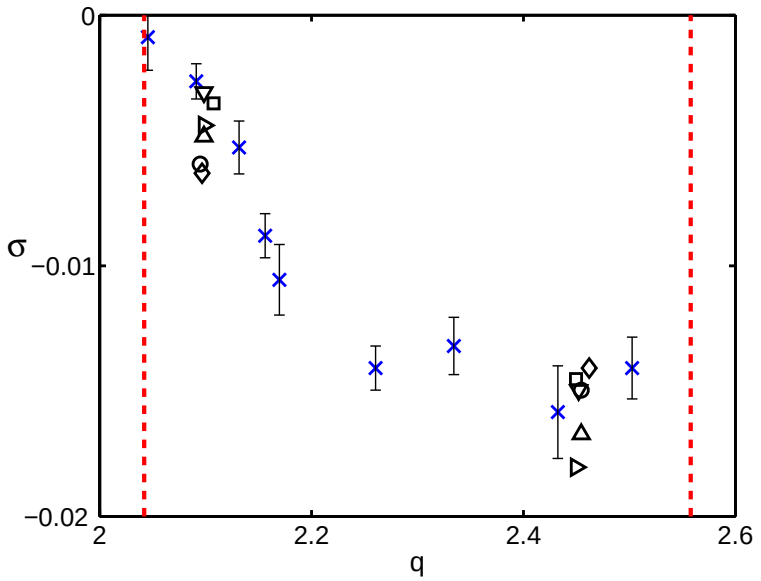

Figure 33: Plot of growth rate vs. wave number for the transverse perturbation. The dashed lines represent experimentally measured boundaries of the stable band measured previously for $\epsilon = 0.46$. The data are shown for $\theta = 0$ ($\times$,$\circ$), $\theta = \pi/18$ ($\square$), $\theta = \pi/12$ ($\Diamond$), $\theta = \pi/6$ ($\triangleright$), $\theta = \pi/3$ ($\triangle$), and $\theta = 2\pi/3$ ($\triangledown$).

4.2.1 Angular Dependence of Perturbations

Amplitude equation analyses [14, 15] suggest that phase perturbations with a finite phase-modulation wave number k are neither purely transverse nor purely longitudinal, *i.e.*, for longitudinal perturbations $\mathbf{\Phi}_l$ is not parallel to $\mathbf{k}$ and for transverse perturbations $\mathbf{\Phi}_t$ is not perpendicular to $\mathbf{k}$. (Recall that the derivation of the phase equation assumed $k \to 0$.) In that case there is a "mixing" of the phase perturbations which is a function of θ, the angle between $\mathbf{k}$ and the $\mathbf{q}_1$ wave vector. The mixing is in general non-zero except for discrete $\theta = n\pi/6$, where n is an integer. A consequence is that the growth rates of phase perturbations are also expected to be functions of θ. Thus to investigate the mixing in the experiment, the two types of phase perturbation were applied at different angles, with $k = 0.14$ and at two different values of q inside the stable band, and their growth rates were measured. As predicted by the theory the results were not significantly different for $\theta = n\pi/6$, for $n = 1$, 2 and 4 (Figs. 33 and 34), indicating little or no angular dependence. For $\theta = \pi/12$ and $\pi/18$, where the mixing is expected to be strong, the growth rates were

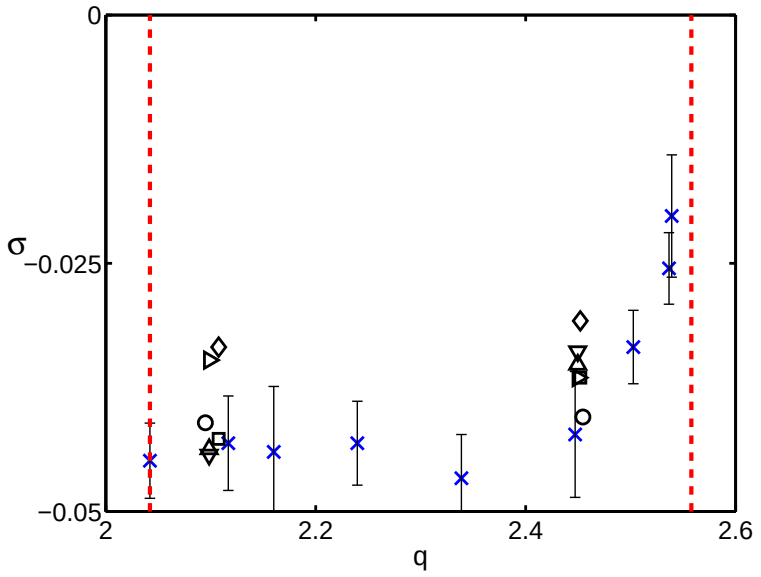

Figure 34: Plot of growth rate vs. wave number for the longitudinal perturbation. The dashed lines represent experimentally measured boundaries of the stable band for $\epsilon = 0.46$. The growth rate of the longitudinal perturbation appears to sharply decrease and trend to zero at the high-wave-number boundary. The data are shown for $\theta = 0$ ($\times$,$\circ$), $\theta = \pi/18$ ($\square$), $\theta = \pi/12$ ($\Diamond$), $\theta = \pi/6$ ($\triangleright$), $\theta = \pi/3$ ($\triangle$), and $\theta = 2\pi/3$ ($\triangledown$).

not significantly different, suggesting that k is small enough that phase mixing is weak.

4.2.2 Remarks

The angular independence of the growth rate for $k \to 0$ adds to the difficulty of identifying the instability mechanism as the pattern breaks down. A transverse-phase perturbation with $\mathbf{k}$ at $\theta = 30°$ destabilizes the pattern at the low-q boundary but *looks* qualitatively different to the eye from the transverse perturbation with $\mathbf{k}$ at $\theta = 0°$. To identify the instability mechanism by working backward from a pattern at the edge of the stable band it is necessary to first know the direction of $\mathbf{k}$ and then to demodulate appropriately. Thus we were not able to confirm the nature of the instabilities at either boundary by imposing an ideal pattern and observing it as it breaks down.

Mechanisms other than phase instabilities might also play a role in limiting the stable-wave-number band. The growth rate data conclusively show that the transverse perturbation becomes unstable at the low-q boundary (Fig. 33). The data are less convincing at the high-q boundary where the growth rates of the longitudinal perturbation are tending toward

zero so rapidly that the resolution of our experimental setup is insufficient to resolve very small growth rates near the boundary (Fig. 34). In principle, amplitude instabilities could limit the stable band at high q; however, theoretical work on Bénard-Marangoni convection [26] suggests that when buoyancy effects are weak, amplitude instabilities play no role in secondary instability of hexagons.

Some insight into the ϵ dependence of secondary instability mechanisms can be gained by comparing these results with the measurements of the stable wave-number band. The measured low-q boundary does not change significantly for $0 < \epsilon < 1$ suggesting that the transverse phase instability is the mechanism that limits the stable band for that range. Similarly, the high-q boundary remains unchanged for $0.4 \lesssim \epsilon < 1$, suggesting the longitudinal-phase instability governs the high-q limit. However, for $\epsilon \lesssim 0.4$ the high-q limit depends strongly on ϵ. Thus, by analogy with the Busse balloon for straight rolls, where a change in the nature of the ϵ dependence of the stability boundaries *can* indicate transitions between different mechanisms, it is possible that the dominant instability mechanism may change (say from a longitudinal- to a transverse-phase instability) as ϵ is decreased below 0.4. Future experimental work could explore this aspect. Complementary theoretical and numerical studies could investigate the importance of amplitude instabilities at those boundaries too.

4.3 Penta-hepta Defects

As motivated in Chapter III, secondary phase instabilities occur for pattern wave numbers outside the stable band and lead to the formation of penta-hepta defects (Fig. 35). The motion of the PHDs then adjusts the wave number of the pattern back into the stability region. The following sections present experimental results of investigations of the motion of a single PHD embedded in a hexagonal pattern and compare them with theoretical predictions.

4.3.1 Trajectory and Speed of PHD

The PHD is a state of bound dislocations in two of the three roll patterns that make up the hexagonal pattern. Its motion adds or removes rolls from the components that make up the pattern as their respective dislocations move, thereby altering the overall wave number.

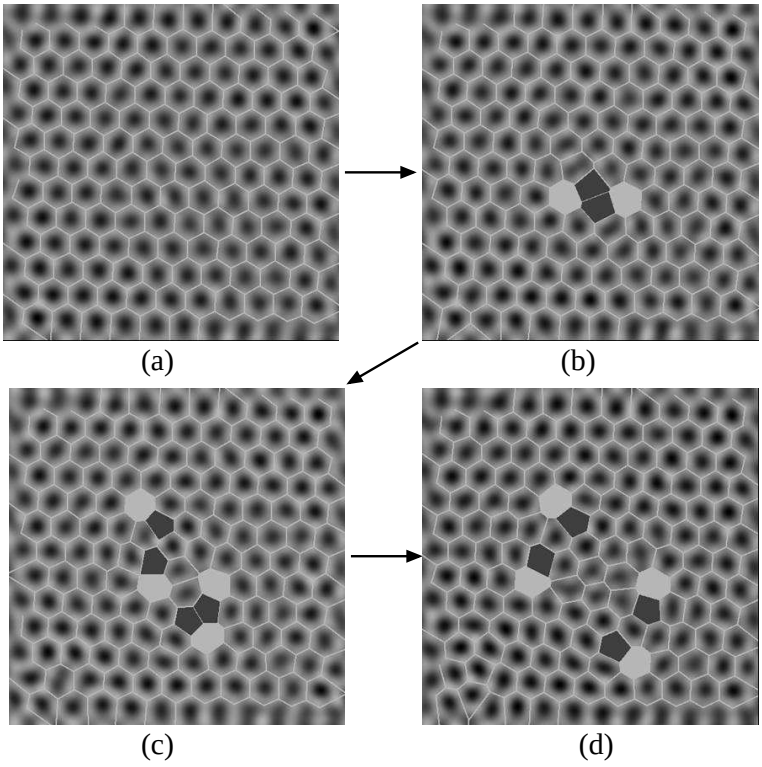

Figure 35: Pairs of PHDs forming spontaneously from an initially ideal hexagonal pattern with q too small. The dark cells are five-sided and the light cells are seven-sided. The defects propagate outward and increase q in the process.

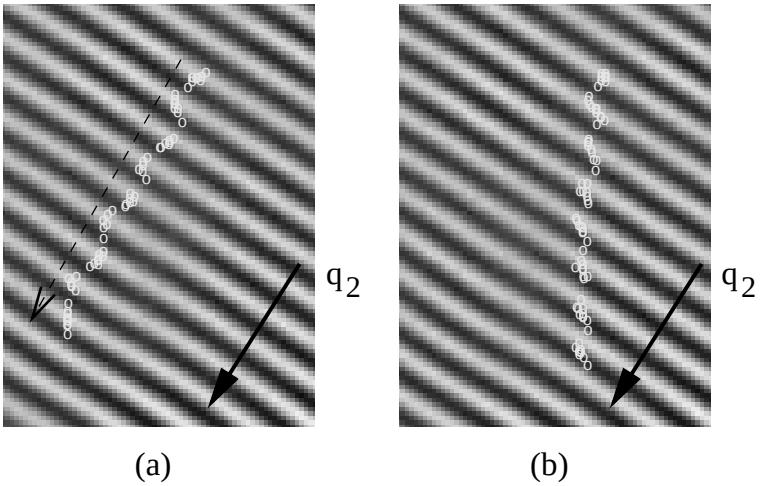

Figure 36: The trajectory of an isolated PHD for (a) equal and (b) unequal wave numbers at $\epsilon = 0.28$. Each circle represents the position of the PHD in intervals $\sim\tau_v$. The dashed arrows indicate direction of PHD motion. The trajectories are plotted on the defect-free mode $\mathbf{q}_2$. (a) For $Q_1 = Q_2 = Q_3 = 0.16$ the path is roughly parallel to $\mathbf{q}_2$. (b) Trajectory after Q_3 is decreased by 0.6.

As in the case of roll patterns the motion depends on the $Q_j = q_j - q_d$, the wave number "corrections" to the optimal wave number of the pattern. If $Q_j = 0$ for both component roll patterns with dislocations then the PHD does not move.

Without loss of generality the labeling of the roll patterns from Tsimring's paper are changed in the following discussion for convenience to allow easy comparison with our experimental results. Thus, as in the experiments, Q_1 refers to the roll patterns of Tsimring's analysis that have a dislocation of phase-winding number $+2\pi$. Q_3 refers to the roll pattern with a -2π phase-winding number dislocation, and Q_2 refers to the dislocation-free rolls.

The following three distinct initial conditions were considered in the theory and experiments:

4.3.1.1 $Q_1 = Q_3$

A main result of Tsimring's theoretical and numerical studies [15] is the prediction that when the wave number corrections of the roll patterns with dislocations are equal and non-zero, the PHD motion is parallel to the wave vector of the dislocation-free rolls. The direction of motion is not affected by small changes in the wave number of the dislocation-free rolls.

However, a change in the wave number of either roll pattern with a dislocation strongly affects the direction. Fig. 36(a) shows the path of a PHD imposed in the experiment for $Q_1 = Q_2 = Q_3 = 0.16$. The overall direction of motion is clearly parallel to $\mathbf{q}_2$ the wave vector of the dislocation-free roll pattern. The background wave number of the pattern is larger than the optimal wave number and the PHD motion is, as expected, in a direction that reduces q_1 and q_3. From the symmetry of the pattern the motion parallel to $\mathbf{q}_2$ is the only unbiased direction reducing q_1 and q_3 at an equal rate. Adjustments made to Q_2 did not change the direction of motion significantly enough to yield a measurable effect. However, making $Q_3 = 0.1$ while keeping $Q_1 = 0.16$ causes a substantial change in the direction (Fig. 36(b)). In that case Q_1 is farther from the optimal value than Q_3 and the PHD moves in a direction that reduces Q_1 at a quicker rate than it reduces Q_3.

4.3.1.2 Varying Q_3 while $Q_1 = Q_2 = 0$

Quantitative predictions of the path and speed of the PHD motion as a function of Q_3 are computed by Tsimring [15]. Fig. 37 plots the direction of motion, ψ, vs. Q_3 and the speed, v, vs. Q_3 when $Q_1 = Q_2 = 0$. The direction of motion is approximately parallel to $\mathbf{q}_2$, the wave vector of the other roll pattern with a dislocation, and the speed is predicted to increase approximately linearly with $|Q_3|$.

In the experiment the direction of motion and speed of the PHD were measured as a function of Q_1 rather than Q_3 as in the theory. Fig. 38 plots the results for the case of $Q_2 = Q_3 = 0$. The PHD is observed to travel approximately parallel to $\mathbf{q}_3$, the second roll pattern with a dislocation, consistent with what would be expected from from an analysis of the theoretical results. Motion parallel to $\mathbf{q}_3$ is pure climb along the $\mathbf{q}_3$ rolls which keeps $Q_3 = 0$. Thus the direction is parallel or antiparallel to $\mathbf{q}_3$ depending on whether the $Q_1 < 0$ or $Q_1 > 0$ (Fig. 39). The data appears to confirm the subtle deviation of ψ from the direction parallel to $\mathbf{q}_3$ for values of Q_1 close to zero predicted by Tsimring.

In the experiment the PHD speed also increases approximately linearly with Q_1. However, the speed for $Q_1 > 0$ is less than that for similar magnitudes of Q_1 when $Q_1 < 0$. It is unclear why that is the case.

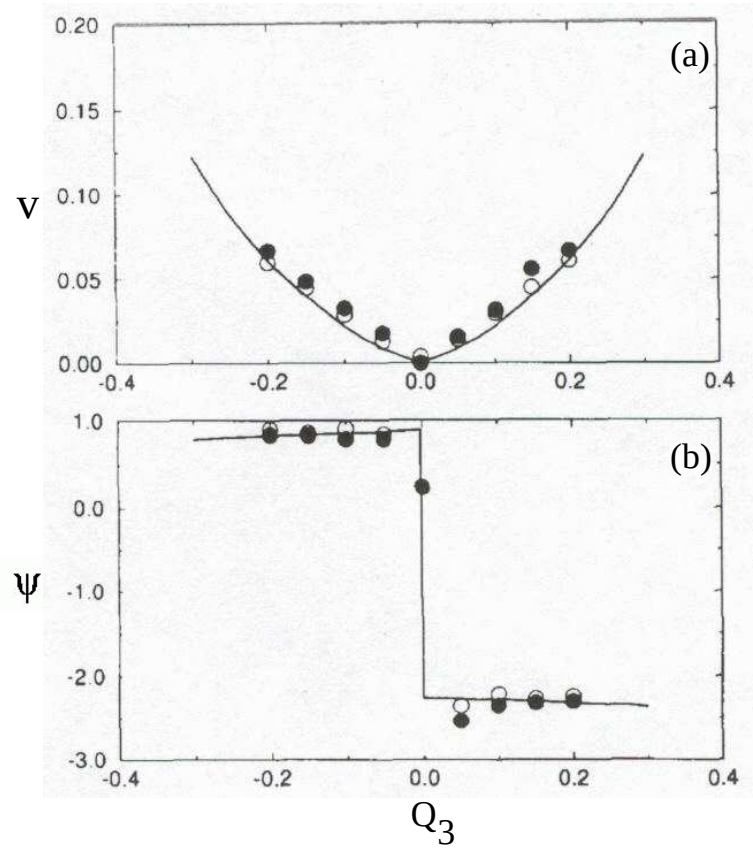

Figure 37: Theoretical and numerical predictions of (a) speed and (b) angle of the PHD motion as a function of the wave number correction Q_3 of the component rolls with dislocation of negative phase-winding number. For the other component roll patterns corrections are $Q_1 = Q_2 = 0$. The angles are measured with respect to the wave vector of the dislocation-free roll pattern. The solid lines are theoretical predictions, and the open and closed circles are from numerical simulations. (Adapted from Tsimring [15].)

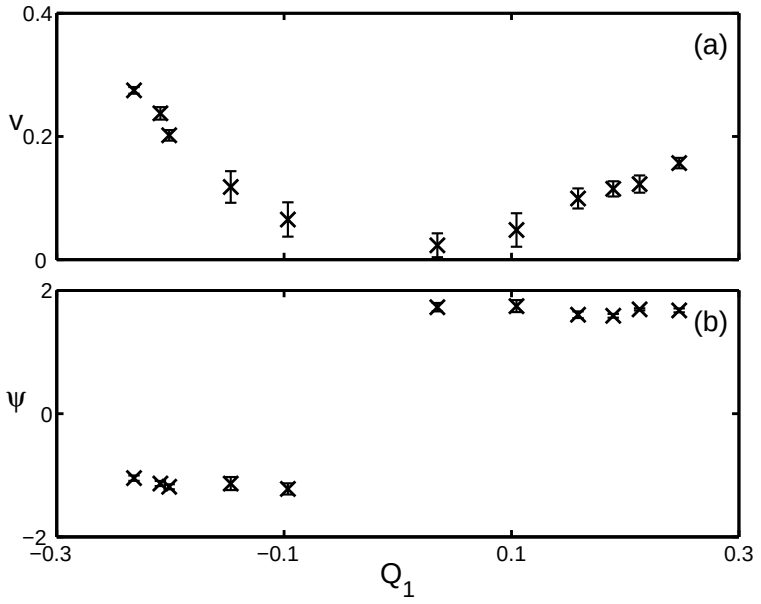

Figure 38: Measured (a) speed and (b) angle of PHD motion as a function of the wave number correction Q_1 for $\epsilon = 0.46$. $Q_2 = Q_3 = 0$. The angles are measured with respect to the $\mathbf{q}_2$ wave vector. The gaps in the data plots correspond to values of Q_1 for which the PHD-path length was too short to estimate an accurate direction of motion.

4.3.1.3 Varying Q_1 while $Q_3 \neq 0$ and $Q_2 = 0$

Quantitative predictions of the PHD motion as a function of Q_1, when $Q_3 = 0.1$ and $Q_2 = 0$, are plotted in Fig. 40. In that case the direction of motion depends strongly on the combination of wave number corrections, and the PHD speed increases with $|Q_1|$ in a weakly nonlinear way.

In the experiment the measured dependence of ψ on Q_1, when $Q_3 = 0.14$ and $Q_2 = 0$, is also strong. The direction of motion ψ, changes smoothly (within the error of the experiment) through the range shown in the shaded region of Fig. 42 in qualitatively the manner predicted by the theory. In that case there is PHD motion even when $Q_1 = 0$ by virtue of $Q_3 \neq 0$; there is always some climb along q_3 as a result. The speed of the PHD is almost linear for $Q_1 > 0$ but not linear for $Q_1 < 0$. As the speed of the motion for $Q_1 < 0$ near zero is not constant it is difficult to estimate the average speed.

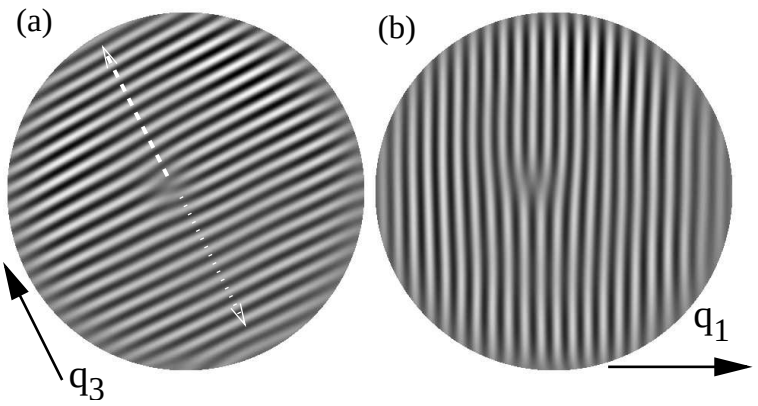

Figure 39: Path of PHD when Q_1 is adjusted and $Q_2 = Q_3 = 0$. Motion is such that the PHD does not climb along the $\mathbf{q}_3$ rolls. The dashed arrow is the direction when $Q_1 > 0$ and the dotted arrow is the direction when $Q_1 < 0$.

4.3.1.4 Remarks

The experimental data of Figs. 38 and 41 qualitatively agrees well with the theoretical predictions of Figs. 37 and 40. Differences such as those observed with the speed measurements may be attributable to boundary effects – it was observed that when the PHD is near the boundary its speed changes. Increasing the aspect ratio of the experiment may reduce the discrepancies. This is most easily achieved by reducing the liquid depth.

A direct quantitative comparison of the measured and computed speeds is misleading since the "microscopic" details of the BMC experiment differ from the parameters used in Tsimring's amplitude equation formulation of the problem. Thus the magnitude of the measured speeds is not expected to be the same. Nevertheless, our results show that the predicted and measured directions of motion can be compared meaningfully; the range of motion is captured very well by the theoretical analysis.

The direction of motion of a PHD was also investigated experimentally by Tam *et al.* [38]. In that experiment an isolated PHD is formed in a raft of soap bubbles that is placed on a glass plate. Unlike in our experiments, it was found that PHD motion is *perpendicular* to the wave vector of the dislocation-free roll pattern. However, their system is an *equilibrium* system, which is qualitatively different from our "out of equilibrium" experiment. In addition, the pattern of soap bubbles is formed out of rigid components

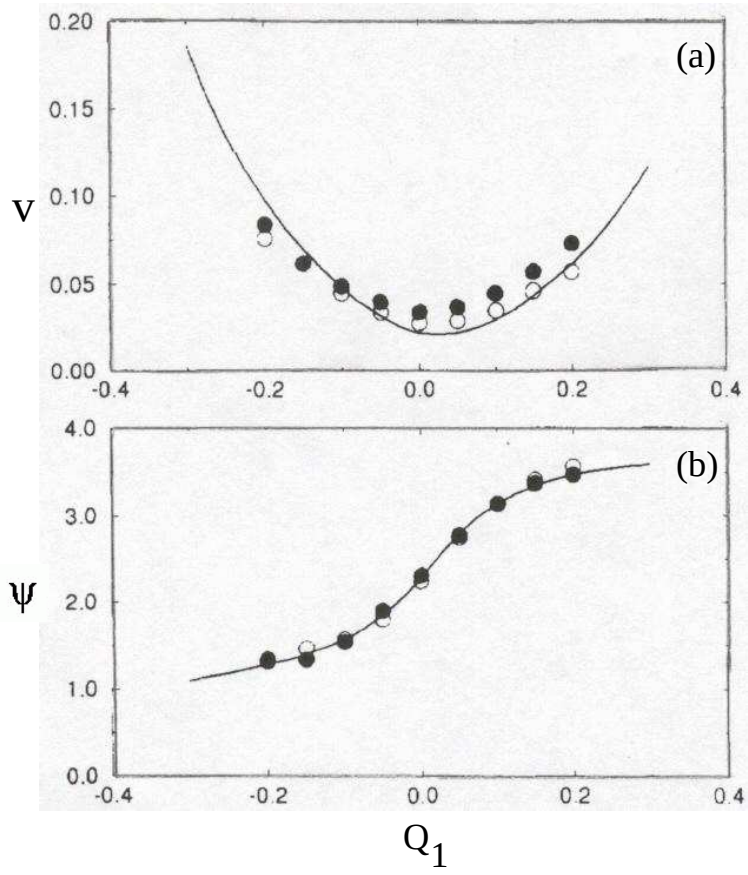

Figure 40: Theoretical and numerical predictions of (a) speed and (b) angle of PHD motion as a function of the wave number correction Q_1 of the component rolls with dislocation of positive phase-winding number. The other component roll pattern with a dislocation has $Q_3 = 0.1$, while the dislocation-free roll pattern has $Q_2 = 0$. The angles are measured with respect to the wave vector of the dislocation-free roll pattern. The solid lines are theoretical predictions, and the open and closed circles are obtained by numerical simulations. (Adapted from Tsimring [15].)

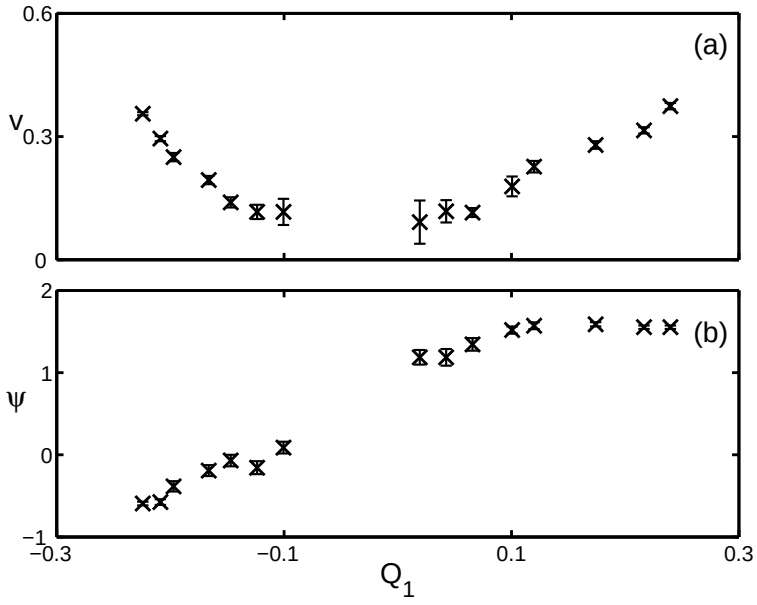

Figure 41: Measured (a) speed and (b) angle of PHD as a function of the wave number correction Q_1 for $\epsilon = 0.46$ for $Q_2 = 0$ and $Q_3 = 0.14$. The angles are measured with respect to the $\mathbf{q}_2$ wave vector. The gaps in the data plots correspond to values of Q_1 for which the PHD-path length was too short to estimate an accurate direction of motion.

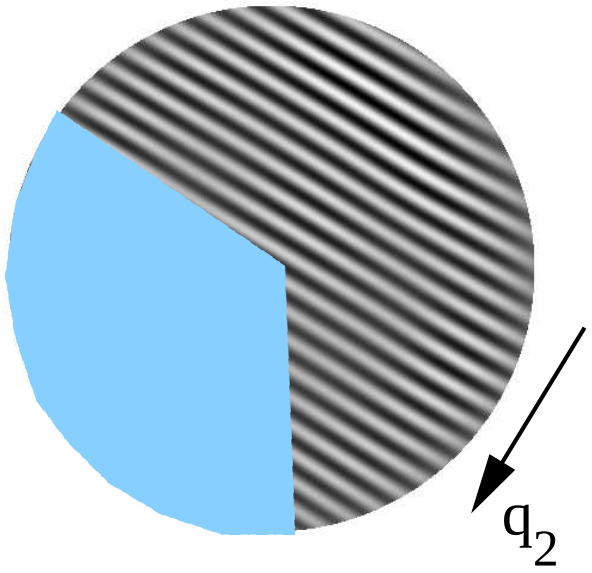

Figure 42: The shaded region marks the range of angles that the PHD moves along when Q_1 is adjusted, for fixed $Q_2 = 0$ and $Q_3 = 0.14$.

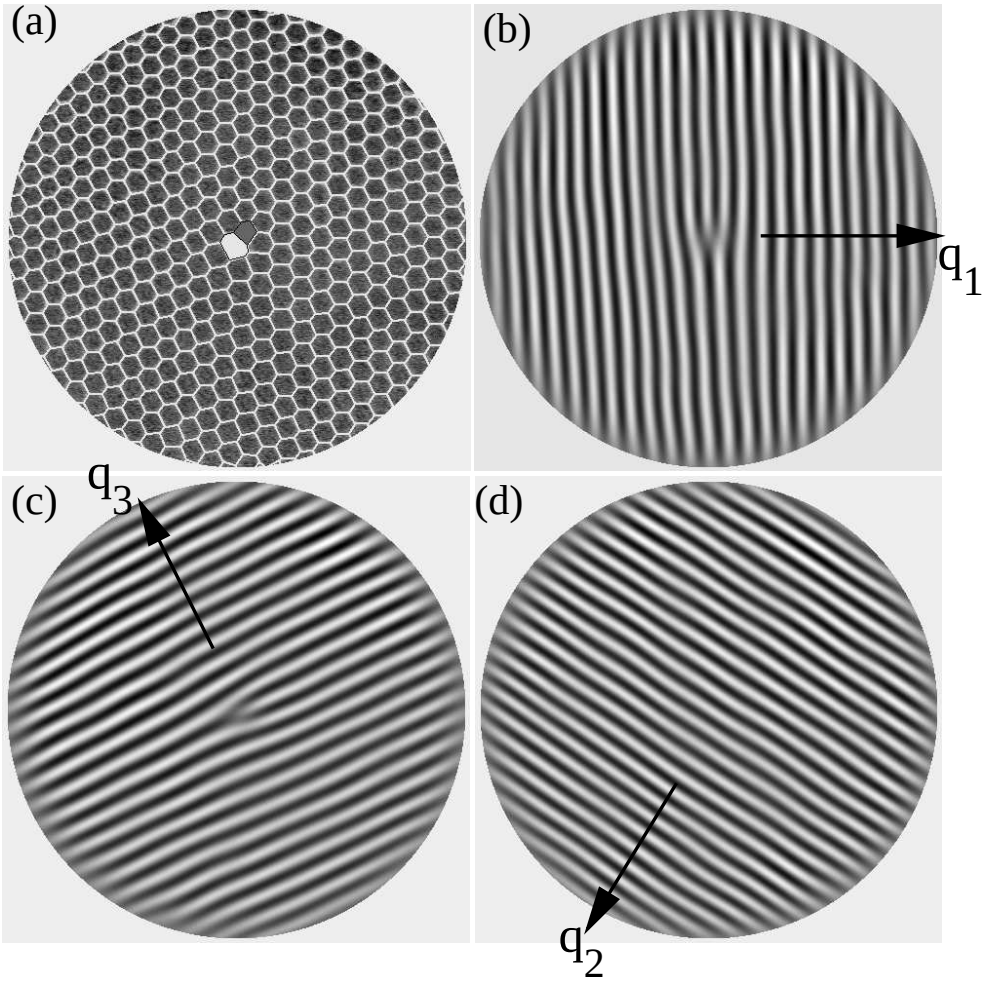

Figure 43: wave-number selection through formation of a PHD: $t = 0$. (a) A single PHD with (a) $q_1 = 2.37$, (c) $q_3 = 2.5$ and (d) $q_2 = 2.68$. q_2 is beyond the high-wave-number boundary ($q = 2.52$) of the stable band.

that do not alter their wave number.

The dislocation-free roll pattern plays a role in wave-number selection when q_2 falls outside the stable band. In that case a roll splits at the core of the PHD, forming two new dislocations of opposite phase-winding number in the $\mathbf{q}_2$ roll pattern. Each new dislocation pairs up with the dislocations in $\mathbf{q}_1$ and $\mathbf{q}_3$ of opposite phase-winding number, thereby creating two PHDs out of four dislocations (Figs. 43- 45). One PHD has a dislocation in the $\mathbf{q}_1$ and $\mathbf{q}_2$ rolls, while the other has a dislocation in the $\mathbf{q}_2$ and $\mathbf{q}_3$ rolls. The two PHDs then move in directions that remove a roll from the $\mathbf{q}_2$ rolls if q_2 is too large, or add a roll if q_2 is too small, thereby adjusting q_2 back into the stable band.

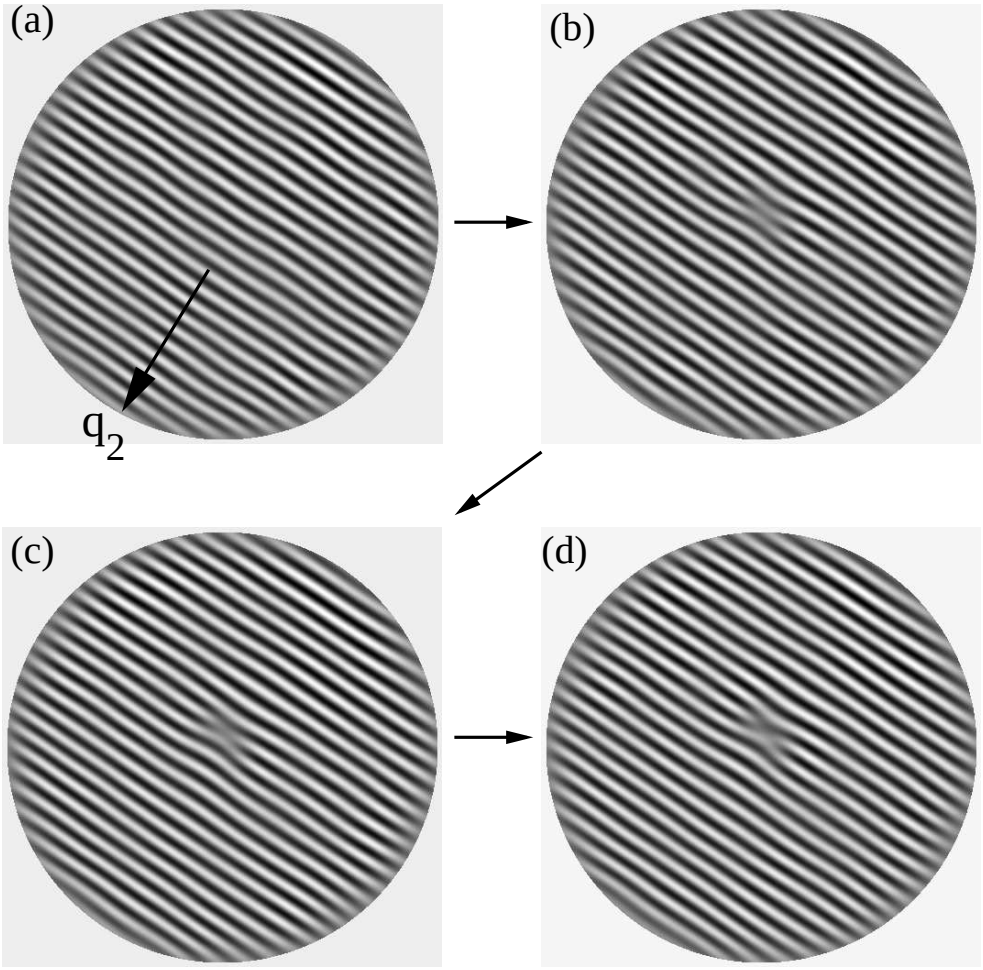

Figure 44: wave-number selection through formation of a PHD: Evolution of $\mathbf{q}_2$ roll pattern. (a) At $t = 0$ the roll pattern is defect-free. A pinching off of the rolls starts to occur at the core of the PHD at (b) $t \sim 16\tau_v$ which (c) grows steadily and (d) by $t \sim 24\tau_v$ a roll has split and formed to two dislocations of opposite phase-winding number.

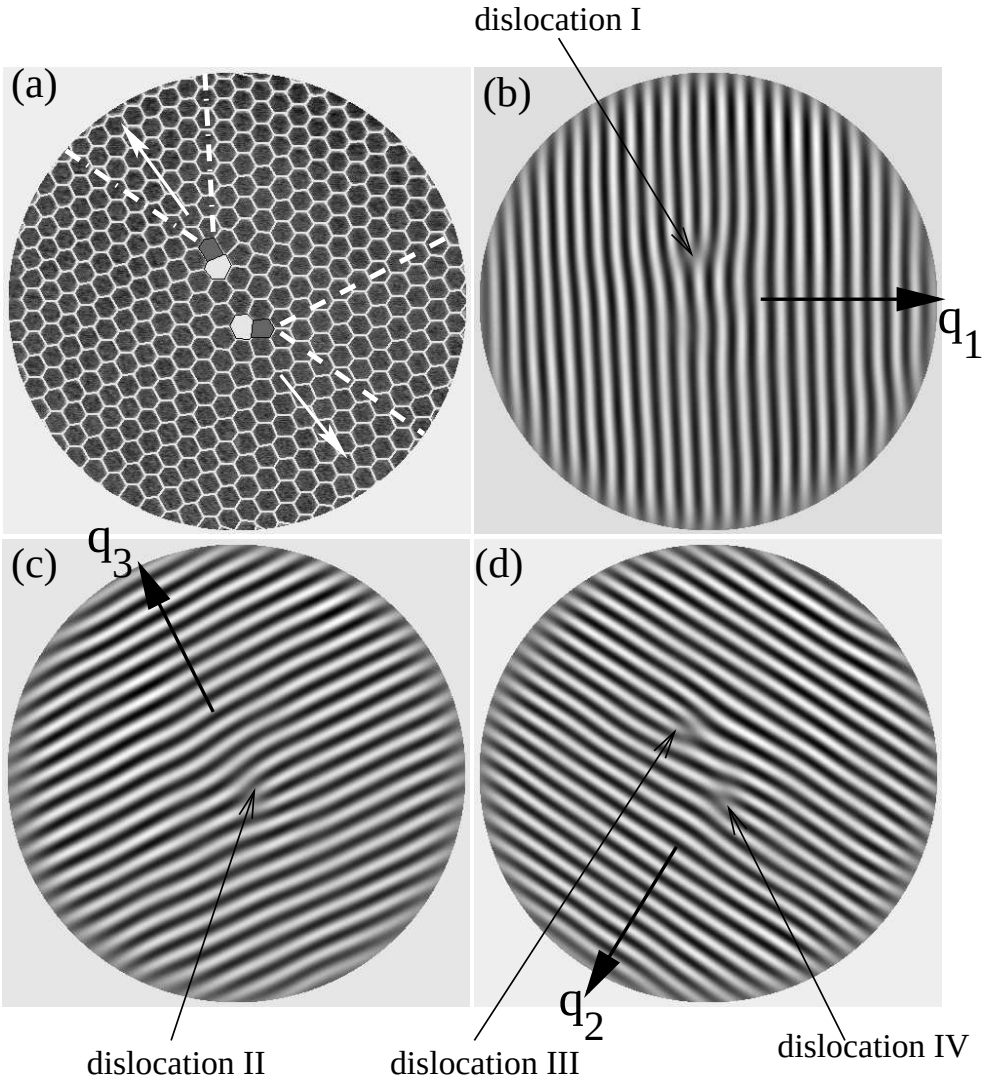

Figure 45: Wave-number selection through formation of a PHD: $t \sim 50\tau_v$; a new pair of PHDs formed out of the old PHD and the two new dislocations, shown in (d), formed from a roll of the $\mathbf{q}_2$ pattern. The PHDs are moving in a direction (white arrows) that eliminates a roll from the $\mathbf{q}_2$ pattern. The original PHD was a combination of dislocations I and II, shown in (b) and (c) respectively. The top PHD is a combination of dislocations I and III, and the bottom PHD is a combination of dislocations II and IV. The dashed and dot-dashed lines in (a) are the extra rows of cells that correspond to rolls with dislocations.

4.3.2 Time Dependence of Speed

The theoretical analysis of Tsimring [15] assumes a constant PHD velocity. However, the experiments demonstrate that this is not always the case. The velocity is observed to change in magnitude and direction under some initial conditions. We distinguish three topologically different types of motion.

4.3.2.1 Cell Collapse

For the case when $Q_1 = Q_2 = Q_3 > 0$ the motion is parallel to $\mathbf{q}_2$ and the PHD removes two rows of hexagonal cells by alternately eliminating a cell from rows perpendicular to the $\mathbf{q}_1$ and $\mathbf{q}_3$ directions. The result is a *zig-zag* trajectory whose overall direction is parallel to $\mathbf{q}_2$ (Fig. 36). The time dependence is due to the collapse of the pentagonal cell (Fig. 46) followed by a rearrangement of the pattern, and occurs through a series of T1 and T2 elementary processes described by Weaire and Rivier [39]. In a T1 process a cell edge shrinks to zero and then grows along a different axis in such a way that cells switch neighbors (Fig. 47(a)). Weaire and Rivier consider a T2 process in which a *three*-sided cell vanishes. Thus the collapsing of a five-sided cell is seen as a continuous series of T1 processes that first make it three-sided, followed by a T2 process which makes it disappear. However, in our experiment the five-sided cell remains five-sided until it vanishes into a vertex plus an edge. A cell collapse, like the one shown in Fig. 46, is relatively quick and causes a brief jump in speed, as the speed-evolution plot of Fig. 49 shows. The subsequent T1 processes that lead to the rearrangement of the cells into the familiar five-sided cell next to a seven-sided cell result in a much slower PHD speed. The speed jump corresponds to a displacement of the PHD by approximately π/q parallel to $\mathbf{q}_2$.

4.3.2.2 Cell Mitosis

The motion anti-parallel to $\mathbf{q}_2$ has a smoother trajectory and the speed has less of a time dependence. It is a result of cell *creation* through division (mitosis), also an elementary process [39], of the heptagonal cell (Fig. 48). This is a topologically different process than that observed in the motion parallel to $\mathbf{q}_2$, and is regarded as a combination of T1 and

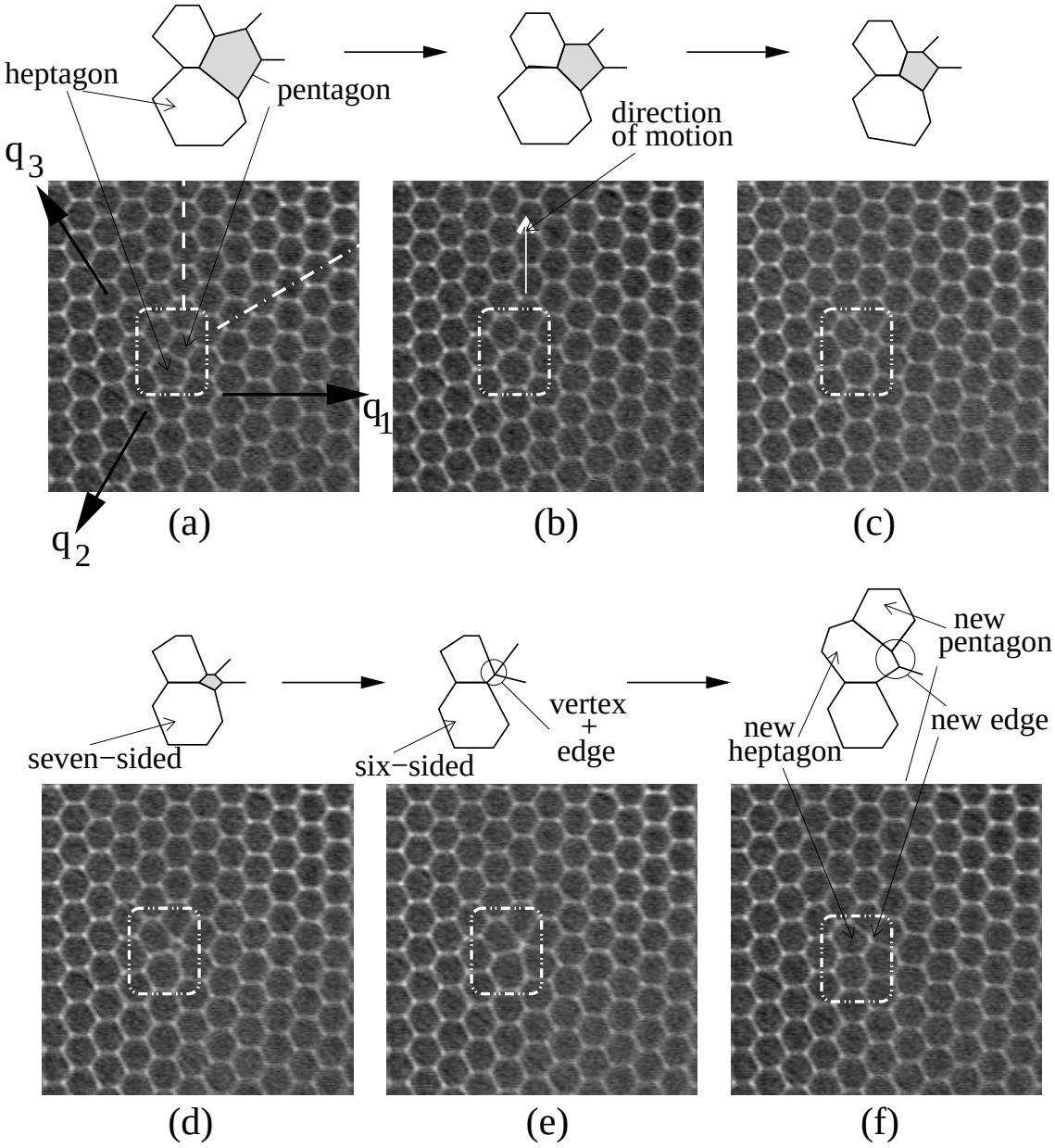

Figure 46: PHD motion via cell collapse. (a) PHD at the center of the pattern. The dashed line marks an extra row of cells of the $\mathbf{q}_1$ component rolls. The dot-dashed line marks an extra row of cells associated with the $\mathbf{q}_3$ rolls. The extra rolls terminate at the PHD core. (b)-(d) The pentagonal cell in the process of collapsing. (e) The pentagon has collapsed into a vertex and an edge and in the process converted the heptagon into a hexagon, and changed a hexagon into a pentagon. (f) A partial T1 process creates an edge which converts a hexagon into a heptagon. Thus the penta-hepta pair has been recreated at new location. The process has reduced the length of the extra roll of $\mathbf{q}_1$, thereby moving the PHD core upward by one cell length.

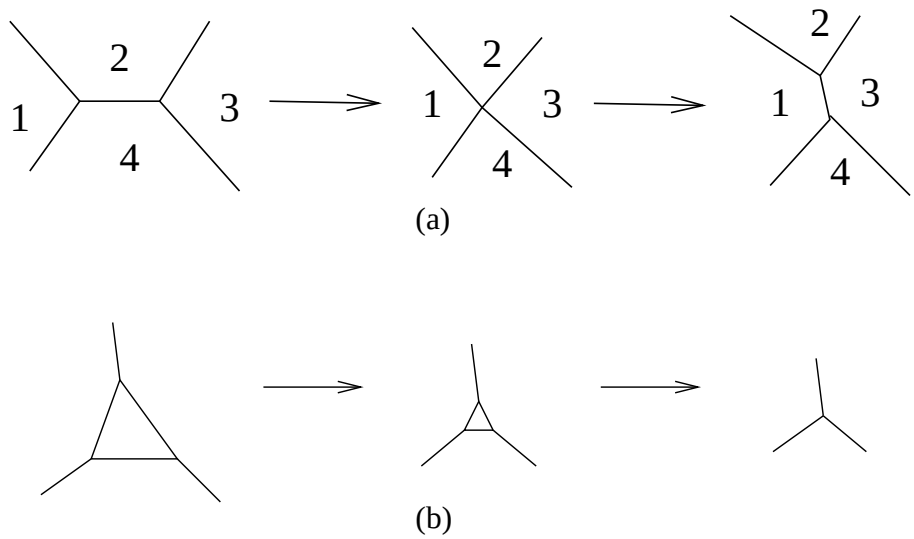

Figure 47: Two elementary processes by which hexagonal patterns rearrange themselves. (a) T1 process – edge between cells 2 and 4 shrinks to zero and is replaced by another resulting in cells 1 and 3 becoming neighbors and 2 and 4 separating. (b) T2 process – a three-sided cell vanishes. (Adapted from Weaire [39].)

inverse T2 processes [39]. Heptagon mitosis results in the displacement of the PHD by approximately π/q antiparallel to $\mathbf{q}_2$.

4.3.2.3 Neighbor-Switching

A third type of motion is observed when the PHD moves primarily by gliding along one roll pattern with a dislocation. For the narrow range of motion for which $Q_1 > 0$ and $Q_3 \approx 0$ (results are similar for $Q_3 > 0$ and $Q_1 \approx 0$) the PHD moves purely through "neighbor switching", *i.e.*, using T1 processes (Fig. 50). The trajectory is smooth and appears to be the least time dependent. However, for $Q_1 < 0$ and $Q_3 \approx 0$ the motion is different. The PHD moves in the opposite direction through a combination of a series of "neighbor switches" similar to the $Q_1 > 0$ case, followed by instances of cell mitosis.

4.3.2.4 Remarks

The three elementary processes proposed by theorists as means by which a hexagonal pattern might arrange itself are not restricted to any particular system. Thus in principle PHDs in other stationary periodic nonequilibrium patterns with hexagonal symmetry, such as the chemical patterns observed in Ref. [2] are likely to propagate in the same manner.

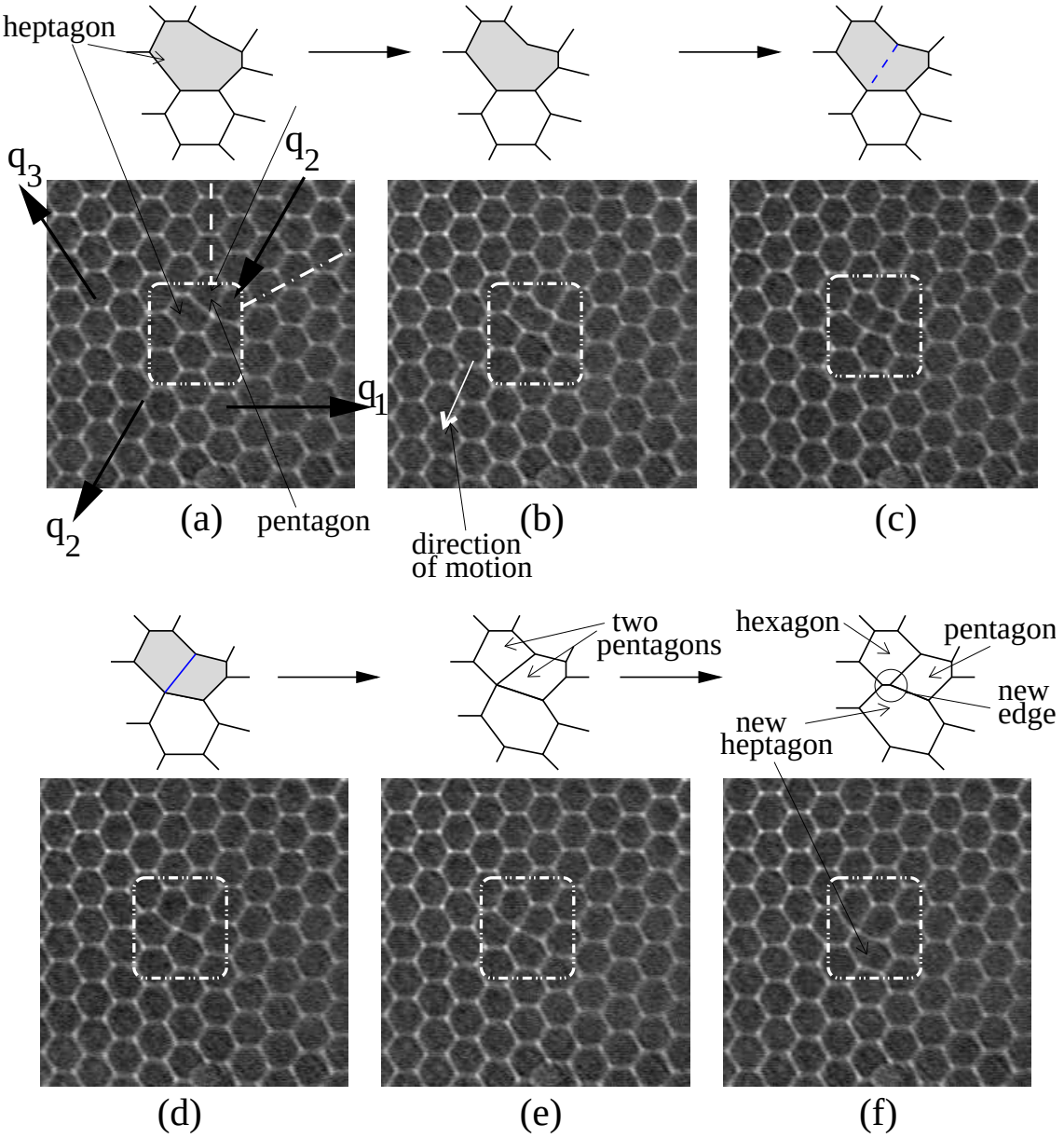

Figure 48: PHD motion via cell mitosis. (a) PHD at the center of the pattern. The dashed line marks an extra row of cells of the $\mathbf{q}_1$ component rolls. The dot-dashed line marks an extra row of cells associated with the $\mathbf{q}_3$ rolls. The extra rolls terminate at the PHD core. (b) The boundary separating the heptagonal and pentagonal cells deforms slightly. (c)-(e) The heptagonal cell splits into two pentagons through mitosis as the downward flowing liquid through its center becomes stronger. (f) After the split a partial T1 process creates an edge which converts one of the pentagons into a hexagon, while at the same time changing a hexagon into a heptagon. Thus the pentagon-heptagon pair has been recreated. The row corresponding to the dislocation in the $\mathbf{q}_1$ rolls has shifted to the left and lengthened slightly in the rearrangement process while the row with a dislocation in $\mathbf{q}_3$ has increased in length by one cell. Thus the core of the PHD has moved by one cell length.

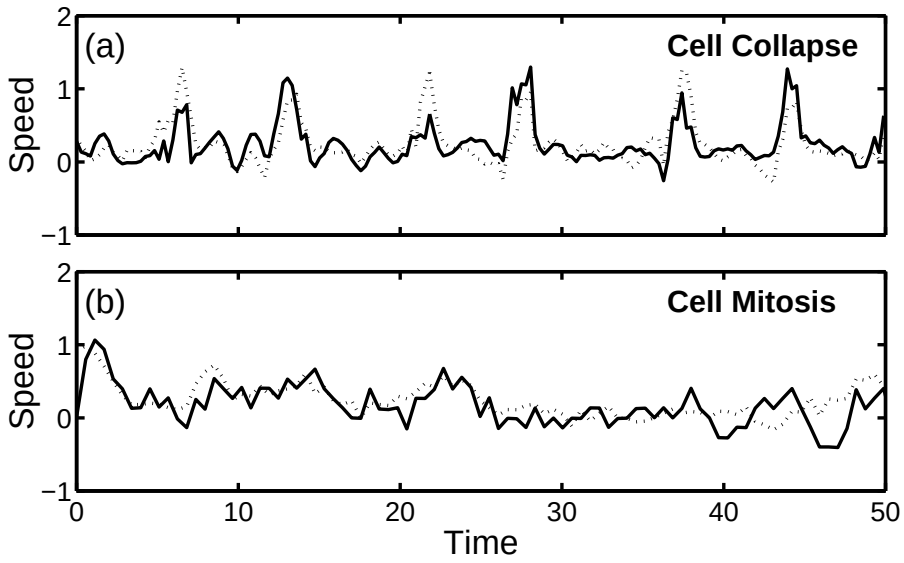

Figure 49: Measured time series of PHD speeds for $q_1 = q_2 = q_3$ at $\epsilon = 0.28$, corresponding to (a) pentagonal cell collapse with $q = 2.23$ and (b) heptagon mitosis with $q = 1.95$. The solid line indicates the magnitude of velocity perpendicular to $\mathbf{q}_2$ while the dashed line shows the magnitude of velocity perpendicular to $\mathbf{q}_3$. Pentagonal cell collapse is characterized by jumps in PHD motion that occur alternately between directions perpendicular to $\mathbf{q}_2$ and perpendicular to $\mathbf{q}_3$; this alternating character is shown in (a). By contrast, PHD motion during heptagon mitosis is smoother, as shown in (b).

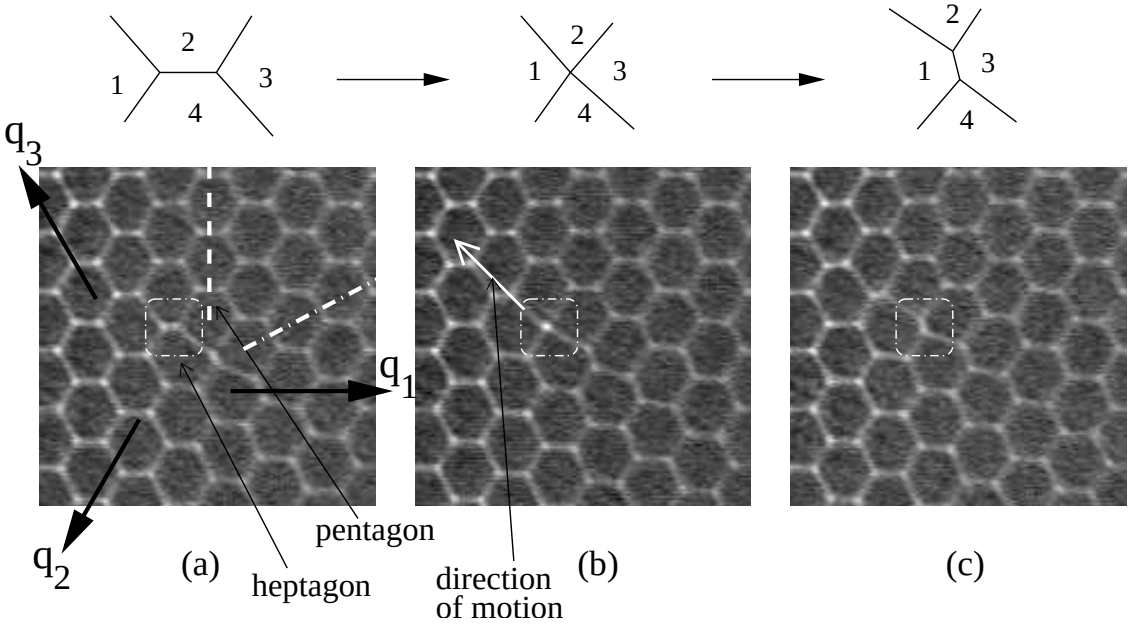

Figure 50: PHD motion via "neighbor switching". The dashed line marks an extra row of cells of the $\mathbf{q}_1$ component rolls. The dot-dashed line marks an extra row of cells associated with the $\mathbf{q}_3$ rolls.The edge indicated by the box (a) shrinks to a point (b) and is replaced by another edge along a different axis (c). In the process of rearrangement the PHD moves by π/q.

4.3.3 Discussion

A pattern typically breaks down through the formation of multiple PHDs. Thus future work on PHDs could explore how two or more affect each other. There are six distinct PHDs corresponding to different combinations of dislocations of opposite phase-winding number in any two roll systems. Thus the studies could examine how the different distinct PHDs interact with one another. Tsimring finds through numerical investigations that two PHDs in a pattern with all $Q_j = 0$ move and either attract or repel each other depending on the configuration of their phase-winding numbers. The movement is caused by distortion of the phase field of one PHD by the other, leading to nonzero Q_j at the location of the PHD. His studies predict that PHDs of the same type will repel. Two PHDs with opposite phase-winding number in the same roll system will attract each other and collide leading to the annihilation of one PHD and the formation of a single PHD of different configuration than the original two. The process is similar to the reverse of the example shown in Figs. (43)-(45)

Tsimring's studies assumed a PHD in a a pattern of infinite lateral extent. While his predictions of the direction of motion are qualitatively confirmed by our measurements, our investigations found that the speed and direction of motion differ significantly from theory. Our results show a strange asymmetry in the speed of the PHD when its direction is reversed. It is unclear whether this is due in some part to boundary effects, as we have observed that as the PHD approaches the boundary, its speed reduces dramatically. Asymmetry also occurs in the case where in one direction the motion is due purely to neighbor-switching, while in the opposite direction the motion is observed to be a mix of neighbor-switching and mitosis. Further investigation is needed to determine whether these are limitations of our experimental setup, or whether they are intrinsic to hexagonal patterns but are missed by the theory.

A possible area of future study could be the control of PHD motion. In the experiments described above, the protocol is to imprint the patterns at time $t = 0$, and to then turn off the forcing for the duration of the experiment to allow the pattern to evolve undisturbed. The result is PHD motion in a straight line. However, if the conditions can be changed *while* the defect is in motion then the path of the PHD can be altered. It is possible to

make small alterations to the wave number of each roll by shifting the pinned boundaries in or out. However, the time frame over which the pattern changes wave number is slow ($\sim 10\tau_v$) thus steering of the PHD is gradual.

CHAPTER V

DISCUSSION

In this thesis we have investigated fundamental aspects of the behavior of hexagonal patterns formed under nonequilibrium external conditions. They fall under the general category of patterns that are spatially periodic and stationary in time. Our focus has been on the symmetry of the pattern itself rather than on the details of the particular system (in this case a Bénard-Marangoni convection experiment) that produces the pattern. To that end, we have compared our experimental results with predictions from amplitude equation studies, which are analyses that reduce the problem to its essential symmetries. Thus, it is expected that our results would apply qualitatively to other driven stationary periodic hexagonal patterns.

The studies are analogous to earlier investigations by Busse *et al.* on patterns of straight rolls. Hexagons are more complex structures that can be represented as a superposition of three roll systems oriented 120° with respect to one another. Our work is the first quantitative experimental investigation of complex patterns in several areas of interest: the extent of the region of stability of the pattern; the nature of the secondary instabilities, which are the mechanisms by which patterns with wave number outside the allowed region of stability become unstable; and the behavior of defects, which typically form through secondary instability.

We showed, contrary to an earlier experimental study, that indeed there is a substantial stable band for hexagons. The band was approximately the same size as that of Bestehorn's theoretical estimate that reduced the "microscopic" equations of a Bénard-Marangoni convection experiment to a set of amplitude equations. Predictions using generic amplitude equations show a larger region of stability for small ϵ than is observed in our experiment. However, that is expected since the theoretical studies assume a hexagonal pattern of infinite lateral spatial extent.

The work on secondary instability was heretofore not studied experimentally. We were able to apply perturbations suggested by amplitude equation analyses and show that they are possible mechanisms of instability at the boundaries of the stable region. This particular set of experiments would benefit from further theoretical collaboration to sort out some ambiguity about the mechanism of instability at the high-wave-number side of the stable band. Current theoretical studies suggest that the stable band is limited only by phase instabilities. However, no experimental investigations have been performed to rule out the possibility of amplitude instabilities being responsible.

The theoretical study of penta-hepta defects (PHDs) by Tsimring extended an earlier study on the motion of single dislocations in roll patterns. PHDs are the hexagonal pattern analog to dislocations in roll patterns, and are not as well understood. Currently our investigations provide the only test of Tsimring's studies. The direction of motion predictions agree well with experimental measurements, while for speed measurements the theory and experiment are not in as good agreement.

By and large, our experimental results show that theoretical studies that focus on pattern symmetries can produce qualitatively good predictions. It is likely that some of the differences observed in experiment are due to boundary effects or inherent system biases in the experimental setup. Typically the effects of such problems can be investigated systematically and reduced. For example, increasing the aspect ratio effectively makes the system larger, *i.e.*, moves the lateral boundary farther away. The experiments can then be repeated and compared for measurable differences.

There are a range of possible areas of future work. In addition to investigating the role of amplitude instabilities in limiting the stable band, it would be useful to probe the ϵ-dependence of the instability mechanisms. Also, an investigation could be carried out to determine whether there is modulation-wavelength dependence of the transverse and longitudinal instability mechanisms. In our investigations it was assumed that there is no wavelength dependence for the phase instabilities when their wavelengths are very large. When PHDs form spontaneously in the bulk of the pattern they do so in pairs. Some numerical studies by Tsimring have yielded predictions about their interactions that can

readily be tested using our current experimental setup. Another area of interest would be an investigation of the effect of lateral boundaries on the motion of PHDs. Our experiments clearly show that the boundary affects their speed and trajectory.

APPENDIX A

PID CONTROL

Proportional-integral-derivative (PID) control is a technique that is used to maintain a process variable ($PV(t)$), such as temperature, at a desired value, referred to as the setpoint ($SP(t)$) [41]. It tracks the error $\epsilon(t)$ between $PV(t)$ and $SP(t)$ and minimizes it based on the the value of the error, its integral over a recent time interval and its current derivative. The three quantities are weighted according to their relative importance, and a controller output $CO(t)$ to be fed to the driving unit, *e.g.* an air conditioner, is generated from

$$CO(t) = P \cdot \epsilon(t) + I \cdot \int_0^t \epsilon(\tau) d\tau + D \cdot \frac{d}{dt}\epsilon(t) \tag{24}$$

where

$$\epsilon(t) = SP(t) - PV(t). \tag{25}$$

Thus if the current error is large, or has been large for a long time or is changing rapidly, the controller output will be large. And if it has remained at the setpoint for a long time the controller output will be very small.

The challenge is in tuning the controller, *i.e.*, choosing the weights appropriately. If The weights are made very large, the controller will aggressively attempt to correct all errors, including small discrepancies. The result would be to drive $PV(t)$ past $SP(t)$ as the controller attempts to correct recent errors, making the control ineffective. Conversely, setting the weights too small would leave the controller unable to correct one error before another error appears. Thus a well tuned controller is set somewhere between the two extreme cases.

In 1942 Ziegler and Nichols [42] empirically created tuning rules that yield "acceptable"

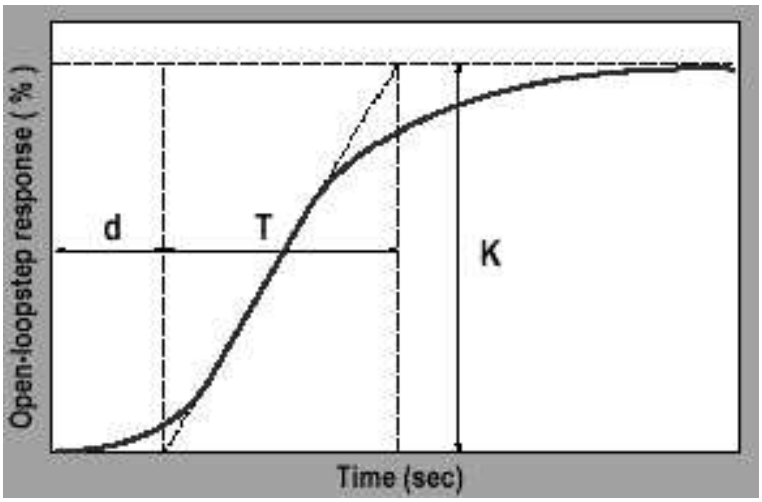

Figure 51: Ziegler-Nichols reaction curve.

controller performance. They proposed the following weights for Eq. (24):

$$P = \frac{1.2 \cdot T}{K \cdot d}, \tag{26}$$

$$I = \frac{0.6 \cdot T}{K \cdot d^2}, \tag{27}$$

$$D = \frac{0.6 \cdot T}{K}, \tag{28}$$

where K, T and d are determined experimentally. If the controller outputs a unit step and the response, $PV(t)$, is plotted against time, then K is the net change in $PV(t)$; T is the process time constant defined as the inverse of the slope of the response curve at its steepest point; and d is the dead time, *i.e.*, the delay between the input time and the response time defined in Fig 51.

APPENDIX B

LINEAR REGRESSION ANALYSIS

Linear regresssion analysis determines the "best fit" straight line for two variables that have a linear relationship. Thus, if data labeled as variable y depends linearly on variable x data, linear regression finds constants a and b such that line $y = a + bx$ minimizes the the least squares error between the data and the straight line. Constant a is the intercept of the line with the y-axis and b is the slope.

The following summary is covered in more detail in Ref. [24]. It is also discussed in most introductory statistics texts.

B.1 Determination of the Slope and the Intercept

It can be shown that for n data points (x_i, y_i) the slope b of the best fit line is given by

$$b = \frac{SS_{xy}}{SS_{xx}}, \tag{29}$$

where

$$SS_{xy} = \sum_{i=1}^{n}(x_i - \overline{x})(y_i - \overline{y}) \tag{30}$$

and

$$SS_{xx} = \sum_{i=1}^{n}(x_i - \overline{x})^2. \tag{31}$$

The constants $\overline{x}$ and $\overline{y}$ are the average values of the variables and are given by

$$\overline{x} = \frac{1}{n}\sum_{i=1}^{n} x_i$$

and

$$\overline{y} = \frac{1}{n}\sum_{i=1}^{n} y_i.$$

The intercept a of the least squares line is given by

$$a = \overline{y} - b\overline{x}. \tag{32}$$

B.2 Determination of the Error in the Slope

The standard error of the slope is given by

$$se_b = \frac{se_r}{\sqrt{SS_{xx}}}, \tag{33}$$

where sum SS_{xx} is defined in Eq. (31), and se_r is the the standard error of the regression, given by

$$se_r = \sqrt{\frac{SS_{yy} - bSS_{xy}}{n-2}}. \tag{34}$$

The sum SS_{xy} is defined in Eq. (30) and

$$SS_{yy} = \sum_{i=1}^{n} (y_i - \overline{y})^2. \tag{35}$$

Assuming the error distribution is approximately normal, the 95% confidence interval for slope b is given by

$$b \pm se_b \times t_{n-2,0.05} \tag{36}$$

where $t_{n-2,0.05}$ is the 95^{th} percentile on a t-distribution with $n-2$ degrees of freedom.

APPENDIX C

EVOLUTION OF HEXAGONAL PATTERNS FROM CONTROLLED INITIAL CONDITIONS IN A BÉNARD-MARANGONI CONVECTION EXPERIMENT

The material for this appendix is found in the published Letter of Ref. [52]. It reports the first experimental measurement of the stable band for nonequilibrium hexagonal patterns, and the observed time dependence in the motion of a penta-hepta defect.

APPENDIX D

PREPRINT: SUBMITTED TO PHYSICAL REVIEW LETTERS SEPTEMBER 2003

This appendix is a preprint submitted to Physical Review Letters in September 2003. It reports the first experimental studies of secondary phase instabilities in hexagonal patterns.

D.1 Secondary Instabilities of Hexagonal Patterns in a Bénard-Marangoni Convection Experiment

Denis Semwogerere and Michael F. Schatz

Center for Nonlinear Science and School of Physics, Georgia Institute of Technology, Atlanta, Georgia 30332-0430

We have identified experimentally secondary instability mechanisms that restrict the stable band of wave numbers for ideal hexagons in Bénard-Marangoni convection. We use "thermal laser writing" to impose long wave perturbations of ideal hexagonal patterns as initial conditions and measure the growth rates of the perturbations. For $\epsilon = 0.46$ our results suggest a longitudinal phase instability limits stable hexagons at high wave number while a transverse phase instability limits low wave number hexagons.

PACS numbers: 47.54.+r, 47.20.-k, 61.72.Ji

For stable, spatially-periodic patterns observed in many nonequilibrium systems [4, 46, 47, 48], the pattern typically exhibits a wave number q that is drawn from range of possible values, even when a given system's external parameters are fixed. The maximum and minimum values of q are typically limited by secondary instability that leads to more complex states. For stationary striped patterns (rolls), the study of secondary instability

in Rayleigh-Bénard convection led to the identification of several instability mechanisms, as cataloged by the "Busse balloon" [8]. These mechanisms have a universal character and have been associated with roll instability in several other physical systems [49, 9, 11]. Periodic patterns of hexagons also arise in diverse physical settings, including fluid flow [16, 26] chemical reactions [2], nonlinear optics [50], crystal growth [51] and granular flow [3]. However, the instability mechanisms that constrain stable wave numbers for hexagons have not, heretofore, been observed in experiments.

In this Letter we describe phase instabilities that limit the stable wave number of hexagonal patterns in Bénard-Marangoni convection experiments. These instabilities initially appear as modulations with small wave number k of the hexagons. Theoretical studies of amplitude equations show that as $k \to 0$ two different instabilities can restrict the stable band [14, 13] – a *longitudinal* modulation with a curl-free phase vector $\mathbf{\Phi}$ and a *transverse* modulation with a divergence-free $\mathbf{\Phi}$. Our experiments demonstrate that these instabilities are observable even with finite k where significant mixing of the longitudinal and transverse modes might occur [14].

In Bénard-Marangoni convection hexagonal convection patterns arise when a fluid with a free upper surface is heated uniformly from below and cooled from above with a sufficiently large temperature gradient. The convective flow is driven primarily by temperature-induced surface tension gradients (*thermocapillarity*) at the liquid-gas interface and is characterized by the Marangoni number $M = \frac{\sigma_T \Delta T d}{\rho \nu \kappa}$, where σ is the liquid's surface tension, ΔT the temperature difference across the liquid layer, $\sigma_T \equiv \frac{d\sigma}{dT}$, and d, ρ, ν, κ are respectively, the liquid's thickness, density, kinematic viscosity, and thermal conductivity. With $\sigma_T < 0$, surface tension gradients draw fluid from warm areas at the liquid-gas interface to cool areas. This creates upflows at the locally warm spots and downflows at the cool areas (Fig. 52(a)).

The experiments are performed on a flat layer of silicone oil of depth $d = 0.094 \pm 0.003$ cm confined by a Teflon sidewall ring of inner diameter 7.62 ± 0.003 cm yielding an aspect ratio of 40.5 for the convecting region. Uniform heating is applied from below and an air gap of thickness 0.074 ± 003 cm is cooled from above to set the control parameter

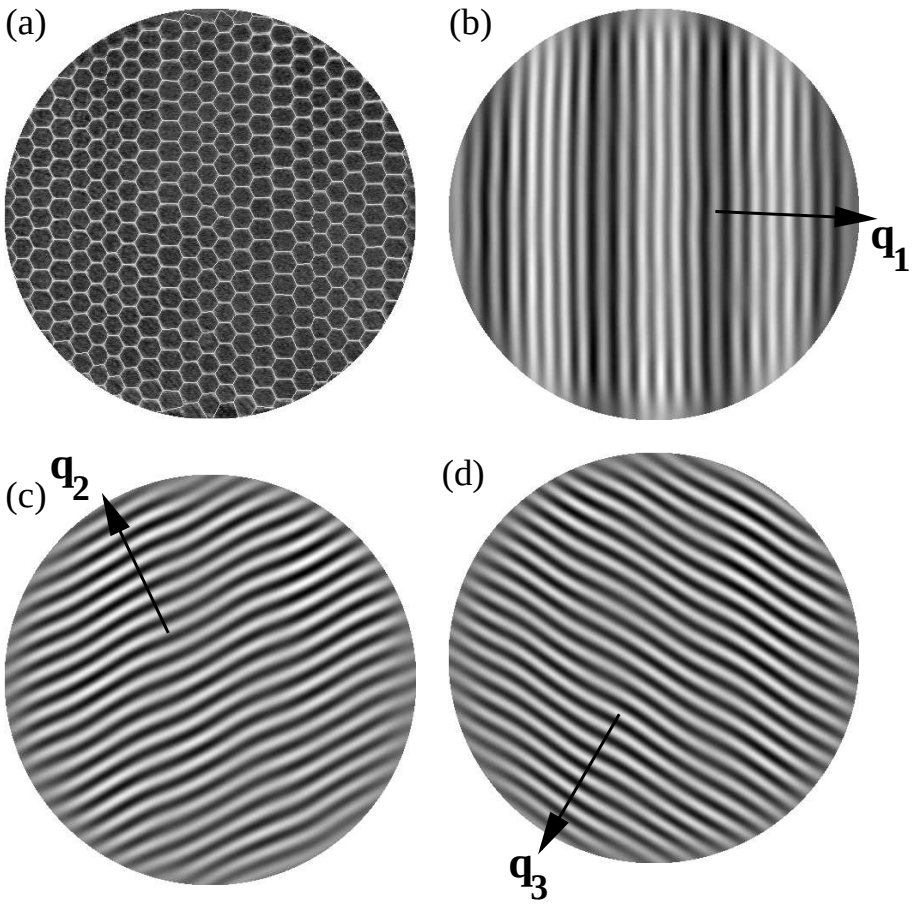

Figure 52: A shadowgraph image (a) of hexagons with a longitudinal phase perturbation is shown with the pattern's three roll components (b-d) extracted by complex demodulation. For the purposes of illustration, the perturbation, imposed as an initial condition, is shown with an amplitude that is larger than typical modulations by a factor of 8. In (a), the white edges and dark centers of the hexagons indicate, respectively, regions of downflow and upflow. (b) The main modulation is to the $\mathbf{q_1}$ rolls – note their compression and dilation. Shading has been added to emphasize the long wave nature of the modulation – the overall lighter areas have higher wave number than the darker regions. (c) $\mathbf{q_2}$ rolls are sheared slightly by the modulation.(d) The $\mathbf{q_3}$ rolls are modulated with the same amplitude and phase as the $\mathbf{q_2}$ rolls.

at $\epsilon = \frac{M-M_c}{M_c} = 0.46$, where M_c is the value of the Marangoni number at the onset of convection. The liquid kinematic viscosity ν is 8.25 ± 0.03 cS and the Prandtl number Pr is 87.2 ± 0.3. All measurements are nondimensionalized by the length scale d and the vertical diffusion time $\tau_v = d^2/\kappa = 8.8$ s. Visualization is achieved using the shadowgraph technique [10]. Images of the patterns are digitized and then analyzed using a variety of Fourier and complex demodulation techniques to extract the spatial dependence of the pattern wave number, amplitude and phase [38, 23, 34]. A hexagonal pattern can decomposed into three component roll patterns oriented 120° with respect to one another. The components are labeled as in Fig. 52 by wave vectors $\mathbf{q_1}$, $\mathbf{q_2}$ and $\mathbf{q_3}$.

The initial conditions of the experiment are imposed by thermo-optically altering the thermocapillary driving [52]. Beginning at fixed ϵ above onset the natural pattern selected by the system is replaced with the desired pattern by heating multiple spatial points along the liquid-gas interface with a scanned infrared CO_2 laser beam. The imposed hot spots become the new regions of liquid upflow thereby establishing the pattern (Fig. 52(a)). The process typically takes less than 10 τ_v, whereupon lasing is turned off. The strong thermal gradients due to the lasing dissipate within $\sim \tau_v$ and thereafter the resulting pattern sets the initial condition from which the subsequent pattern evolution is studied. Lasing is maintained along the outer 25% of the pattern to pin cells in a hexagonal boundary so as to prevent pattern distortion due to creation or destruction of cells at the sidewall.

Imposing ideal hexagons (*i.e.* patterns with $q = |\mathbf{q_1}| = |\mathbf{q_2}| = |\mathbf{q_3}|$) permits measurement of the stable band but is insufficient to determine the mechanisms of the secondary instabilities. The band is determined by imposing ideal patterns at fixed ϵ, and tracking q over time to check for stability [52]. The imposed pattern remains stationary for q in a stable range; however, if q is too large or too small, the imposed pattern becomes unstable. The boundaries of the stable band are taken to be the largest and smallest q that do not change. For unstable values of q the pattern forms penta-hepta defects at the boundaries or within the interior. The defects propagate in such a way as to either add or eliminate cells so that the average q is driven into the stable band [52]. Observation of these instability driven dynamics does not reveal the nature of the mechanisms that cause them, unlike

the case of periodic rolls where phase instabilities such as the zig-zag instability are easily distinguished by eye [8].

The mechanisms of secondary phase instability can be probed by applying phase perturbations to hexagonal patterns. The perturbations are characterized by a wave vector $\mathbf{k}$ and angle θ measured with respect to one of the roll wave vectors (here chosen to be $\mathbf{q_1}$ for convenience). In the long wavelength limit ($k \to 0$) the phase vector of the perturbation can be written as $\mathbf{\Phi} \equiv -(\phi_2 + \phi_3)\hat{\boldsymbol{\imath}} + (\phi_2 - \phi_3)/\sqrt{3}\hat{\boldsymbol{\jmath}}$ [14, 13], where ϕ_1, ϕ_2 and ϕ_3 are terms added to the phases of the $\mathbf{q_1}$, $\mathbf{q_2}$ and $\mathbf{q_3}$ rolls respectively. In that case there are two classes of phase perturbation: a longitudinal perturbation for which $\mathbf{\Phi} \parallel \mathbf{k}$ and a transverse perturbation for which $\mathbf{\Phi} \perp \mathbf{k}$. For $\theta = 0$ the longitudinal perturbation is taken as $\phi_1 = i\alpha coskx$, $\phi_2 = -i\frac{1}{2}\alpha coskx$ and $\phi_3 = -i\frac{1}{2}\alpha coskx$ (Fig. 52), where α is proportional to the perturbation amplitude and the x axis is parallel to $\mathbf{q_1}$. The result is a sinusoidal modulation of the wave number of the $\mathbf{q_1}$ rolls in a direction parallel to $\mathbf{k}$ with amplitude $k\alpha$ (Fig. 54(a)). The perturbations to the $\mathbf{q_2}$ and $\mathbf{q_3}$ rolls have similar modulations parallel to $\mathbf{k}$ but with amplitude $\frac{1}{2}k\alpha$. For the transverse perturbation (Fig. 53) $\phi_1 = 0$, $\phi_2 = i\frac{\sqrt{3}}{2}\alpha coskx$ and $\phi_3 = -i\alpha\frac{\sqrt{3}}{2}coskx$. In that case the $\mathbf{q_1}$ rolls are unperturbed while the $\mathbf{q_2}$ and $\mathbf{q_3}$ rolls are perturbed sinusoidally along the x axis with amplitude $\frac{\sqrt{3}}{2}k\alpha$.

Perturbations applied at fixed ϵ decay exponentially when q is within the stable band and do so with a growth rate that depends on q. The growth rate is measured by first applying the perturbation as an initial condition and then tracking the evolution of its amplitude. The logarithm of the amplitude plotted against time fits reasonably well to a straight line (Fig. 54(b)) indicating that the perturbations decay exponentially as expected for disturbances that are sufficiently small. The slope obtained from a linear least squares fit yields the perturbation's growth rate.

Secondary instabilities are identified by observing the behavior of their growth rates at the boundaries of the stable band. The growth rate of the transverse perturbation is found to remain relatively constant for $2.2 \lesssim q \lesssim 2.55$ but starts to gradually decrease in magnitude for $q \lesssim 2.2$ until it crosses zero at the low wave number boundary (Fig. 55(a)). This suggests that the divergence-free transverse perturbation becomes unstable at the low

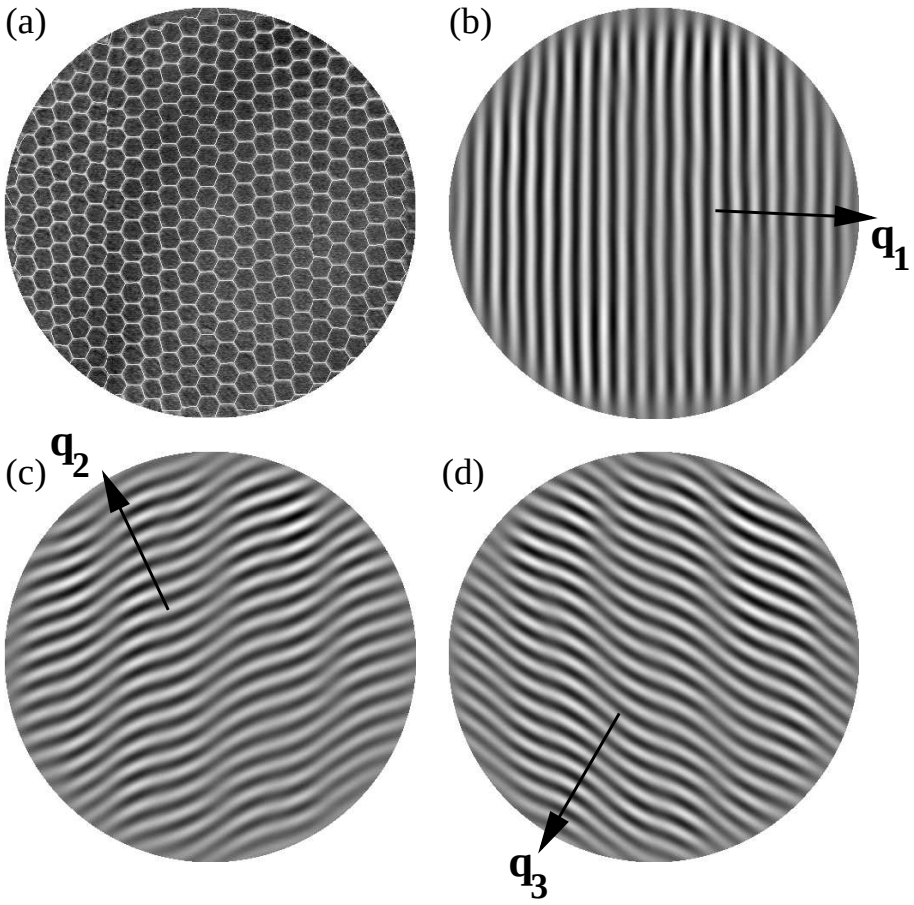

Figure 53: A shadowgraph image (a) of hexagons with a transverse phase perturbation is shown with the pattern's three roll components (b-d) extracted by complex demodulation. For the purposes of illustration, the perturbation is shown with an amplitude that is larger than typical modulations by a factor of 9. (b) The $\mathbf{q_1}$ component is unaffected by the transverse modulation. (c) The roll component labeled by wave vector $\mathbf{q_2}$ that shows the shearing of the rolls in a direction transverse to the $\mathbf{q_1}$ rolls. (d) The $\mathbf{q_3}$ component is modulated with the same amplitude but opposite phase as the $\mathbf{q_2}$ component.

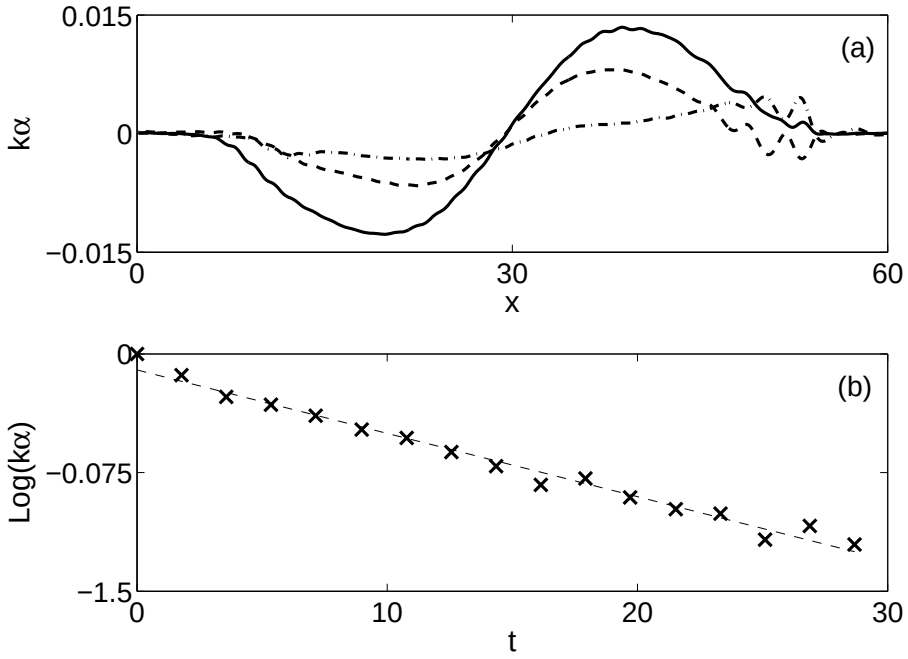

Figure 54: Spatial and temporal evolution of the longitudinal phase perturbation. (a) The profile of the local wave number of the $\mathbf{q_1}$ rolls (scaled by the mean value $q = 2.08$) is plotted at times $t = 0$ (symbol $-$), $t = 13$ ($--$) and $t = 27$ ($\cdot-$); thus the phase modulation adjusts the overall wave number by a maximum of less than 1.5%. The long wave nature of the perturbation is apparent – the modulation wave number $k = 0.14$ is approximately $1/15^{\text{th}}$ of the mean q. (b) The amplitude ($k\alpha$) is plotted as a function of time on a semi-log scale; the slope of this curve yields the growth rate, which is negative for perturbations within the stable band.

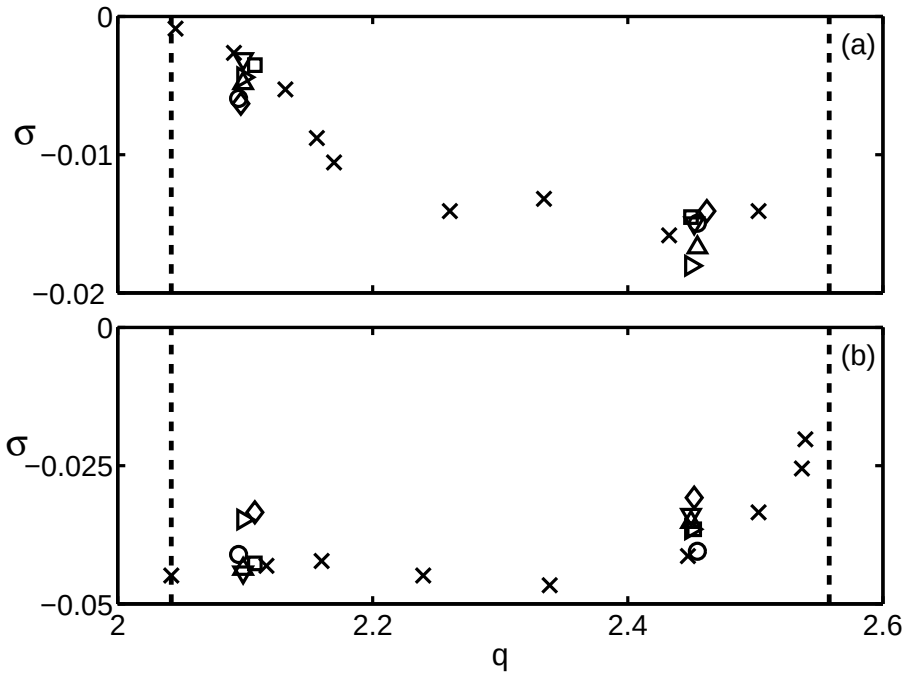

Figure 55: Plots of growth rate vs. wave number for the transverse perturbation (a) and the longitudinal perturbation (b). The dashed lines represent experimentally measured boundaries of the stable band measured previously for $\epsilon = 0.46$. (a) The growth rate for the transverse perturbation appears to go to zero at the low wave number boundary. (b) The growth rate of the longitudinal perturbation appears to sharply decrease and trend to zero at the high wave number boundary. The data are shown for $\theta = 0$ ($\times$,$\circ$), $\theta = \pi/18$ ($\square$), $\theta = \pi/12$ ($\Diamond$), $\theta = \pi/6$ ($\triangleright$), $\theta = \pi/3$ ($\triangle$), and $\theta = 2\pi/3$ ($\triangledown$).

wave number side of the stable band and is thus responsible for the instability at that boundary. At the high wave number boundary the magnitude of the growth rate does not reduce, *i.e.*, the transverse modulation does not appear to restrict the band at high wave number. For the longitudinal phase perturbation the measured growth rate is finite at the low wave number boundary and remains constant for $2.05 \lesssim q \lesssim 2.4$. As q approaches the high wave number boundary the change in growth rate is not slow as in the transverse case, but becomes increasingly sharp the closer q gets to the boundary, and appears to trend to zero growth rate at the boundary (Fig. 55(b)), *i.e.*, the longitudinal perturbation may be the secondary instability that restricts the stable band at high wave number.

Amplitude equation analyses [14, 15] suggest that phase perturbations with finite k are neither purely transverse nor purely longitudinal, *i.e.*, for longitudinal perturbations

$\mathbf{\Phi}$ is not parallel to $\mathbf{k}$ and for transverse perturbations $\mathbf{\Phi}$ is not perpendicular to $\mathbf{k}$. This "mixing" of phase perturbations is a function of θ and is in general non-zero except for $\theta = n\pi/6$, where n is an integer. A consequence of this is that the growth rates of phase perturbations are also functions of θ. In the experiments, with $k = 0.14$ and at two different values of q in the stable band, growth rates were measured for $\theta = n\pi/6$, for $n = 1$, 2 and 4. The results were not significantly different (Fig. 55) indicating no mixing, consistent with theory [14]. For $\theta = \pi/12$ and $\pi/18$ where mixing is expected to be strong, the growth rates were also not significantly different, suggesting that k is small enough that phase mixing is weak.

Mechanisms other than phase instabilities might also play a role in limiting the stable wave number band. The growth rate data conclusively show that the transverse perturbation becomes unstable at the low q boundary. The data are less convincing at the high q boundary where the growth rates of the longitudinal perturbation are trending toward zero so rapidly the resolution of our current experiments is insufficient to resolve very small growth rates near the boundary. In principle, amplitude instabilities could limit the stable band at high q; however, theoretical work on Bénard-Marangoni convection [26] suggest that when buoyancy effects are weak, amplitude instabilities play no role in secondary instability of hexagons.

Some insight into the ϵ dependence of secondary instability mechanisms can be gained by comparing these results with previous measurements of the stable wave number band [52]. The measured low q boundary does not change significantly for $0 < \epsilon < 1$ suggesting that the transverse phase instability is the mechanism that limits the stable band for that range. Similarly, the high q boundary remains unchanged for $0.4 \lesssim \epsilon < 1$, suggesting the longitudinal phase instability governs the high q limit. However, for $\epsilon \lesssim 0.4$ the high q limit depends strongly on ϵ. Thus, by analogy with the Busse balloon for straight rolls, where a change in the nature of the ϵ dependence of the stability boundaries *can* indicate transitions between different mechanisms, it is possible that the dominant instability mechanism may change (say from a longitudinal to a transverse phase instability) as ϵ is decreased below 0.4. Future experimental work complemented by theoretical and numerical studies at the

same parameter values would be useful to map the dependence of secondary instability mechanisms on ϵ and elucidate the relative importance of phase and amplitude instabilities.

We thank Yuan-Nan Young and Hermann Riecke for reading an early version of the paper and for many helpful discussions. We also thank Keng-Hwee Chiam and Mark Paul for the use of their local wave number analysis code. Support for this work by the National Science Foundation and the Research Corporation is gratefully acknowledged.

REFERENCES

[1] L. Zhang, H.S. Cho, F. Li, R.M. Metzger, W.D. Doyle, "Cellular growth of highly ordered porous anodic films on aluminium", J. Mat. Sci. Let. **17**, 291 (1998).

[2] Q. Ouyang, H. Swinney, "Transition from a uniform state to hexagonal and striped Turing patterns", Nature **352**, 610 (1991).

[3] P. B. Umbanhowar, F. Melo, H. L. Swinney, "Periodic, aperiodic and transient pattens in vibrated granular layers", Physica A **249**, 1 (1998).

[4] L. Rayleigh, "On convection currents in a horizontal layer of fluid, when the higher temperature is on the under side", Phil. Mag. **32**, 529 (1916).

[5] J. L. Rogers, M. F. Schatz, "Supperlattice patterns in vertically oscillated Rayleigh-Bénard convection", Phys. Rev. Lett., **85**, 4281 (2000).

[6] W. S. Edwards, S. Fauve, "Patterns and quasi-patterns in the Faraday experiment", J. Fluid Mech. **278** 123 (1994).

[7] M. C. Cross, P. C. Hohenberg, "Pattern Formation Outside of Equilibrium", Rev. Mod. Phys. **65**, 851 (1993).

[8] M.M. Chen and J. A. Whitehead, "Evolution of two-dimensional periodic Rayleigh convection cells of arbitrary wave-numbers", J. Fluid Mech. **31**, 1 (1968); F. H. Busse and J. A. Whitehead, "Instabilities of convection rolls in a high Prandtl number fluid", J. Fluid Mech. **47**, 305 (1971).

[9] S. Nasuno, S. Kai, "Instabilities and transition to defect turbulence in elctrohydrodynamic convection of nematics", Euro. Phys. Lett. **14**, 779 (1991).

[10] J. R. de Bruyn, E. Bodenschatz, S. W. Morris, S.P. Trainoff, Y. Hu, D. S. Cannell, G. Ahlers, "Apparatus for the study of Rayleigh-Bénard convection gases under pressure", Rev. Sci Instrum. **67**, 2043 (1996).

[11] J. Plumecoq, C. Szwaj, D. Derozier, M. Lefranc, S. Bielawski, "Eckhaus instability induced by nonuniformities in a laser", Phys. Rev. A **64** 061801 (2001).

[12] R. B. Hoyle, "Cross-Newell equations for hexagons and Triangles", Phys. Rev. E **61**, 2506 (2000).

[13] B. Echabarria and C. Pérez-Garciá, "Phase instabilities in hexagonal patterns", Euro. Phys. Lett. **43**, 35 (1998).

[14] Y.-N. Young, H. Riecke, "Mean flow in hexagonal convection: stability and nonlinear dynamics", Physica D **163**, 166 (2002).

[15] L.S. Tsimring, "Penta-hepta defect motion in hexagonal patterns", Phys. Rev. Lett. **74**, 4201 (1995); L. S. Tsimring, "Dynamics of penta-hepta defects in hexagonal patterns", Physica D **89**, 368 (1996).

[16] H. Bénard, "Les torbillons cellulaires dans une nappe liquide", Rev. Gen. Sci. Pure Appl. **11**, 1261 (1900).

[17] J. R. A. Pearson, "On convection cells induced by surface tension", J. Fluid Mech., **4** 489 (1958).

[18] J. Thomson, "On certain curious motions observable at the surfaces of wine and other alcoholic liquors", Phil. Mag. **10** 330 (1855).

[19] C. Marangoni, "Über die ausbreitung der tropfen einer flüssigkeit auf der oberfläche einer anderen", Ann. Phys. **143** 337 (1871).

[20] D. A. Nield, "Surface tension and buoyancy effects in cellular convection", J. Fluid Mech. **19**, 341 (1964).

[21] P. A. Manneville, "Dissipative Structures and Weak Turbulence", edited by H. Araki, A. Libchaber and G. Parisi, Academic Press, London (1990).

[22] F. H. Busse, "Non-linear properties of thermal convection", Rep. Prog. Phys. **41**, 1929 (1978)

[23] S. Ciliberto, P. Coullet, J. Lega, E. Pampaloni, and C. Pérez-García, "Defects in roll-hexagon competition." Phys. Rev. Lett. **65**, 2370 (1990).

[24] B. Gerstman, "StatPrimer", Retrieved Nov. 3, 2003 from San Jose State University, Dept. of Health Science. Web site: http://www.sjsu.edu/faculty/gerstman/StatPrimer.

[25] M. M. Sushchik, L. S. Tsimring, "The Eckhaus instability in hexagonal patterns", Physica D **74**, 90 (1994).

[26] M. Bestehorn, "Phase and amplitude instabilities for Bénard-Marangoni convection in fluid layers with large aspect ratio", Phys. Rev. E **48**, 3622 (1993).

[27] S. J. VanHook, M. F. Schatz, J. B. Swift, W. D. McCormick and H. L. Swinney, "Long-wavelength surface-tension-driven Bénard convection: experiment and theory", J. Fluid Mech. **345**, 45, (1997).

[28] M. F. Schatz, G. P. Neitzel, "Experiments on Thermocapillary Instabilities", Ann. Rev. Fluid Mech. **33**, 93 (2001).

[29] P. Cerisier, C. Pérez-García, R. Occelli, "Evolution of induced patterns in surface-tension driven Bénard convection", Phys. Rev. E **47**, 3316 (1993).

[30] E. L. Koschmieder, D. W. Switzer, "The wavenumbers of supercritical surface-tension-driven Bénard convection", J. Fluid Mech. **240**, 533 (1992).

[31] M. F. Schatz, S. J. VanHook, W. D. McCormick, J. B. Swift, and H. L. Swinney, "Onset of surface-tension-driven Bénard Convection", Phys. Rev. Lett. **75**, 1939 (1995).

[32] S. Benz, P. Hintz, R. J. Riley and G. P. Neitzel, "Instability of thermocapillary-buoyancy convection in shallow layers. Part 2. Suppression of hydrothermal waves", J. Fluid Mech. **359**, 165 (1998).

[33] K-H. Chiam, M. Paul, California Institute of Technology, Dept. of Physics.

[34] David A. Egolf, Ilarion V. Melnikov, Eberhard Bodenschatz, "Importance of local pattern properties in spiral defect chaos", Phys. Rev. Lett. **80**, 3228 (1997).

[35] L. M. Pismen, A. A. Nepomnyashchy, "Structure of dislocations in the hexagonal pattern", Europhys. Lett. **24**, 461 (1993).

[36] M. I. Rabinovich, L. S. Tsimring, "Dynamics of dislocations in hexagonal patterns.", Phys. Rev. E **49**, 35 (1993).

[37] K. Nitschke, A. Thess, "Secondary instability in surface-tension-driven Bénard convection." Phys. Rev. E **52** 5772 (1995).

[38] T. Tam, D. Ohata and M. Wu, "Dynamics of a penta-hepta defect in a hexagonal pattern.", Phys. Rev. E **61**, R9 (2000).

[39] D. Weaire, N. Rivier, "Soap, cells and statistics–random patterns in two Dimensions.", Contemp. Phys **25**, 59 (1984).

[40] H. Riecke, Northwestern University, Dept. of Engineering Sciences and Applied Mathematics.

[41] V. VanDoren,"PID – The basic technique for feedback control", Control Engineering **44**, 132 (1997).

[42] J. G. Ziegler, N. B. Nichols, "Optimum settings for automatic controllers", Trans. ASME **64**, 759 (1942)

[43] W.J. Firth, Proc. SPIE Int. Soc. Opt. Eng. (U.S.A.) **2039**, 290 (1993).

[44] F. H. Busse, J. Math. and Phys., "On the stability of two-dimensional convection in a layer heated from below." **46**, 140 (1967).

[45] Q. Ouyang, G. H. Gunaratne and H. L. Swinney, "Rhombic patterns: Broken hexagonal symmetry.", Chaos **3**, 707 (1993).

[46] A. M. Turing, "The chemical basis of morphogenesis.", Phil. Trans. R. Soc. London B **237**, 37 (1952).

[47] E. Dubois-Violette, G. Durand, E. Guyon, P. Manneville and P. Pieranski, "Instabilities in nematic liquid crystals." in *Solid State Phys.*, edited by L. Liebert, Suppl. **14**, 147 (1978).

[48] R. C. DiPrima and H. L. Swinney, "Instabilities and transition in flow between concentric rotating cylinders.", in *Hydrodynamic Instabilities and the Transition to Turbulence*, edited by H. L. Swinney and J.P. Gollub (Springer-Verlag, New York, 1981), p.139.

[49] J. R. de Bruyn, C. Bizon, M. D. Shattuck, D. Goldman, J. B. Swift and H. L. Swinney, "Continuum-type stability balloon in oscillated granular layers.", Phys. Rev. Lett. **81**, 1421 (1998).

[50] R. Neubecker and E. Benkler, "Empirical bifurcation analysis of optical pattern formation.", Phys. Rev. E **65**, 66206 (2002).

[51] B. Caroli, C. Caroli, B. Roulet, "On the stability of hexagonal patterns in solidification of binary mixtures.", Journal Crystal Growth **68**, 677 (1984).

[52] D. Semwogerere, M. F. Schatz, "Evolution of hexagonal patterns from controlled initial conditions in a Bénard-Marangoni convecton experiment." Phys. Rev. Lett. **88**, 054501 (2002).